# Supplementary Materials for

## Algorithm-driven DNA nanostructure design for advanced functionality

Nicolas Levy & Julie Finkel,
Allan Mills, Gerrit David Wilkens, Anjelica Kucinic, Aurélie Ancelin,
Pierre Marcus, Octave Hazard, Joris Picot, Daria Pchelina,
Gaëtan Bellot* and Nicolas Schabanel*

*Corresponding authors: nicolas.schabanel@ens-lyon.fr and gaetan.bellot@cbs.cnrs.fr

# Supplementary Information

## Table of Contents

# S1 ENSnano geometric model to design curved DNA helix bundles, Table ST1, algorithm SA1, and figs. S1 to S12

## S1.1 Default DNA parameters used in ENSnano

The 3D positions of Nucleotides are computed in ENSnano using six parameters as shown in fig. S1: the helix radius $R$, the rise $\Delta$, the inclination $I$, the helicity $\chi$, the minor groove angle $\alpha$ and the inter-helices axis distance $H$. The default value of these parameters in table ST1 are based on three papers: the crystallographic data from[22] for $R$, $\Delta$, $I$, and $\alpha$; data from[21] for $\alpha$ and $\chi$; and data from[32] for $H$. Phosphate positions parameters from[22] are used to compute the nucleotides positions parameters by placing the nucleotides in the middle of two consecutive phosphates: as a consequence, the nucleotide inclination is set to $I_N = I_P - 2 \times (\Delta/2) = 0.375 - 0.332 = 0.043\,\text{nm}$ and the minor groove angle is set to $\beta_N = \beta_P - 2 \times (\alpha/2) = 170.4° - 34.48° = 135.92°$. The inter-helix axis distance is set to $H = 8\Delta = 2.65\,\text{nm}$ based on the double-layer origami data from[32] as the inter-helix distance from one layer corresponds to the distance spanned by 8 bases pair in the other layer. This value is moreover consistent with the average inter-helix distance reported in[39].

Note that the most important parameters for DNA origami design are $\Delta$, $\alpha$, $\chi$ and $H$ as any error on them will accumulated over the span of the design (as opposed to $R$, $\beta$, and $I$). As a fortunate consequence, they are thus the easiest to adjust if needed, as any error on them would be easily detected in experimental data. Finally, recall that it is always possible to impose your own DNA parameters in the ENSnano `.ens` file, as these may change with your own experimental setting (buffer,...).

| | Phosphate positions[22] | Nucleotide positions |
|---|---|---|
| *Radius* | $R = 0.93\,\text{nm}$ | |
| *Rise* | $\Delta = 0.332\,\text{nm}$ | |
| *Inclination* | $I = 0.375\,\text{nm}$ | $I = 0.043\,\text{nm}$ |
| *Twist ($\alpha$) and Helicity ($\chi$)* | $\alpha = \frac{360°}{\chi} = 34.48°$ with $\chi = 10.44\,\text{bp/turn}$ | |
| *Minor groove angle* | $\beta = 170.4°$ | $\beta = 135.92°$ |
| *Inter-helices axis distance* | $H = 2.65\,\text{nm}$ | |

Table ST1: DNA double-helix parameters used in ENSnano: the nucleotides positions are deduced from the phosphate positions as measured in[22] and the DNA parameters used in[21,32].

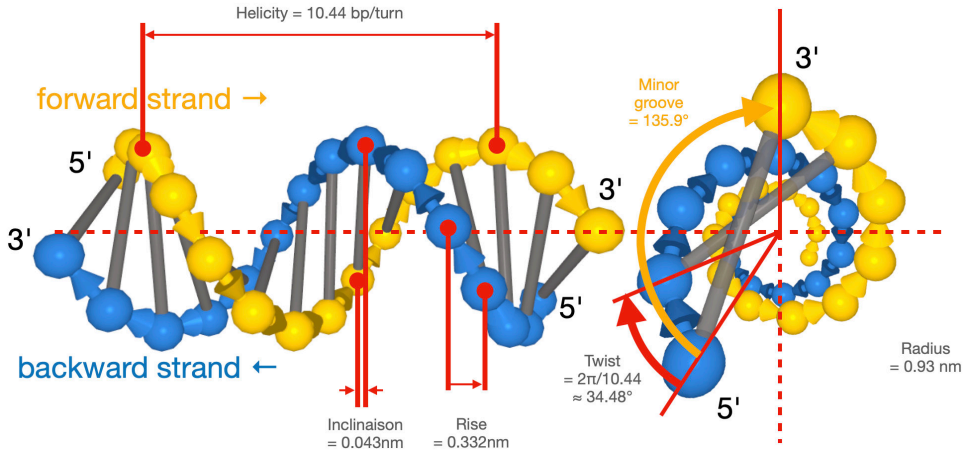


Figure S1: Illustration of DNA double helix parameters.

## S1.2 Curvature and torsion of a 3D curve

Given a 3D curve $t \mapsto M(t)$, we denote by $\dot{M}(t)$, $\ddot{M}(t)$ and $\dddot{M}(t)$ the 1st, 2nd and 3rd derivatives of $M(t)$ with respect to $t$. The *curvature* at $M(t)$ is defined as:

$$\gamma(t) = \frac{||\dot{M}(t) \wedge \ddot{M}(t)||}{||\dot{M}(t)||^3}$$

Its inverse $R(t) = 1/\gamma(t)$ is the *curvature radius* at $M(t)$, that is the radius of its *osculating circle*, which is the circle best approximating the curve at $M(t)$. The *torsion* $\tau(t)$ at $M(t)$ measures how fast the curve takes off from the plane of its osculating circle. It is given by the formula:

$$\tau(t) = \frac{\det\left[\dot{M}(t), \ddot{M}(t), \dddot{M}(t)\right]}{||\dot{M}(t) \wedge \ddot{M}(t)||^2}$$

It is measured in $\text{nm}^{-1}$.

Curvature and torsion at $M(t)$ characterizes the *osculating helix*, that is the helix best matching the curve locally at $M(t)$. Torsion is thus a natural parameter to measure when dealing with DNA helices. Refer to[24] for full details.

As DNA helices are not continuous mathematical curves but discrete, made of nucleotides organised in helicoidal configuration, we use the following discrete version of the torsion. If $M(i)$ be the positions of consecutive nucleotides in a DNA strand, we define the 1st, 2nd, and 3rd *discrete derivatives* at $M(i)$ as:

$$\begin{aligned}
\Delta M(i) &= M(i+1) - M(i), \\
\Delta^2 M(i) &= \Delta M(i+1) - \Delta M(i) = M(i+2) - 2M(i+1) + M(i), \\
\text{and } \Delta^3 M(i) &= \Delta^2 M(i+1) - \Delta^2 M(i) = M(i+3) - 3M(i+2) + 3M(i+1) - M(i).
\end{aligned}$$

The *discrete torsion* is then defined as:

$$\overset{\Delta}{\tau}(i) = \frac{\det\left[\Delta M(i), \Delta^2 M(i), \Delta^3 M(i)\right]}{||\Delta M(i) \wedge \Delta^2 M(i)||^2}$$

The discrete torsion of a straight DNA helix is constant to:

$$\overset{\Delta}{\tau}_{\text{straight DNA helix}} \doteq 0.4851\,\text{nm}^{-1}$$

Next, we will use discrete torsion to evaluate the quality of our algorithms mapping DNA onto arbitrary 3D curves.

## S1.3 Curved DNA model in ENSnano

**Our geometric curved DNA helix model** relies on the definition of a moving frame $\mathbf{F}(t) = (\mathbf{X}(t), \mathbf{Y}(t), \mathbf{Z}(t))$ that adaptively follows the intended curve $t \mapsto M(t)$ (Fig. 1A). The $i$-th nucleotides from the forward and backward strands are placed around the curve using the frame $\mathbf{F}(t)$. Their positions $N_i^f$ and $N_i^b$ are computed from the helix axis points $M(t_i^f)$ and $M(t_i^b)$ located at curvilinear distances $i\,\Delta$ and $(I + i\,\Delta)$ from the origin of the curve, where $\Delta$ and $I$ are the rise and inclination of the DNA B-form helix[22] using the following formula:

$$N_i^f = M(t_i^f) + R\cos(\rho + i\,\alpha)\,\mathbf{X}(t_i^f) + R\sin(\rho + i\,\alpha)\,\mathbf{Y}(t_i^f)$$

$$N_i^b = M(t_i^b) + R\cos(\rho + i\,\alpha + \beta)\,\mathbf{X}(t_i^b) + R\sin(\rho + i\,\alpha + \beta)\,\mathbf{Y}(t_i^b)$$

$$\text{where } s(t) = \int_0^t ||\dot{M}(t)||\,dt \text{ is the curvilinear abscissa (with } \dot{M}(t) = \tfrac{dM(t)}{dt}),$$

$$\text{and } t_i^f = s^{-1}(i\,\Delta) \text{ and } t_i^b = s^{-1}(I + i\,\Delta) \text{ are the parameters } t \text{ for the}$$

$$\text{projections of the } i\text{-th nucleotides (forward and backward) on the curve,}$$

and $R$, $\alpha$, $\beta$, and $\rho$ are respectively the radius, the helical twist, the narrow groove angle, and the roll of the DNA helix (table ST1 and fig. S1).

Several approaches exist for defining a frame $F(t)$ along a curve. The classically used is the Frenet frame, which captures important geometrical properties of the curve such as the tangent, the normal, the osculating plane, etc. However, the Frenet frame tends to undergo sudden rotations in order to adapt to the osculating plane[24]. Using this frame leads to unrealistically twisted DNA helices, ignoring the prevalence of the base-pair stacking interactions which tends to enforce a constant twist around the DNA helix axis (fig. S3).

We thus introduce a *lazily adaptive frame* $\mathbf{F}(t) = (\mathbf{X}(t), \mathbf{Y}(t), \mathbf{Z}(t))$ that rotates as little as possible along the curve. $Z(t)$ is the normalized tangent to the curve at $M(t)$ for all $t$. $X(t)$ and $Y(t)$ are built incrementally along the curve at each of the required locations $t_i^f, t_i^b$ according to algorithm SA1.

## S1.4 Adaptive moving frame algorithm

We denote by $\mathrm{Normalized}(U) = U/||U||$ the normalized vector of a non-zero vector $U$. For two non-colinear vectors $u$ and $v$, we denote by $\mathrm{rot}_{u\to v}$ the rotation mapping $u$ to $v$ around the axis perpendicular to both $u$ and $v$ (i.e., around the cross product $u \wedge v$ of $u$ and $v$).

Algorithm SA1 constructs the adaptive frames used to embed DNA helices in 3D along a given curve in ENSnano.

**Algorithm SA1:** Lazily adaptive frame along a parameterized curve $M(t)$

**Input:** A parameterized curve $t \mapsto M(t)$ and a set $T = \{t_i^f\} \cup \{t_i^b\}$ of the parameters where we need a frame

**Output:** An adaptive right-handed frame $\mathbf{F}(t) = (\mathbf{X}(t), \mathbf{Y}(t), \mathbf{Z}(t))$ for $t \in T$.

`/* Initialization */`
**sort** $T = \{t_1 < \cdots < t_{2n}\}$
**forall** $k = 1..2n$ **do**
  **set** $\mathbf{Z}(t_k) := \mathrm{Normalized}(\dot{M}(t_k))$  `/* Z(t_k) is the normalized tangent */`
$\mathbf{X}(t_1)$ and $\mathbf{Y}(t_1)$ are set arbitrarily so that $(\mathbf{X}(t_1), \mathbf{Y}(t_1), \mathbf{Z}(t_1))$ is a right-handed frame, e.g.: **choose** $\mathbf{U} \in \{(1,0,0), (0,1,0), (0,0,1)\}$ such that $\mathbf{U}$ is not colinear to $\mathbf{Z}(t_1)$, and **set** $\mathbf{Y}(t_1) := \mathrm{Normalized}(\mathbf{Z}(t_1) \wedge \mathbf{U})$ and $\mathbf{X}(t_1) := \mathbf{Y}(t_1) \wedge \mathbf{Z}(t_1)$
`/* Adaptive frame computation */`
**for** $k = 2, 3, \ldots, 2n$ **do**
  **set** $\rho_k = \mathrm{rot}_{\mathbf{Z}(t_{k-1})\to\mathbf{Z}(t_k)}$  `/* the rotation mapping Z(t_{k-1}) to Z(t_k) */`
  **set** $\mathbf{X}(t_k) := \rho_k(\mathbf{X}(t_{k-1})$ and $\mathbf{Y}(t_k) := \rho_k(\mathbf{Y}(t_{k-1})$  `/* rotate the frame according to Z(t_k) */`

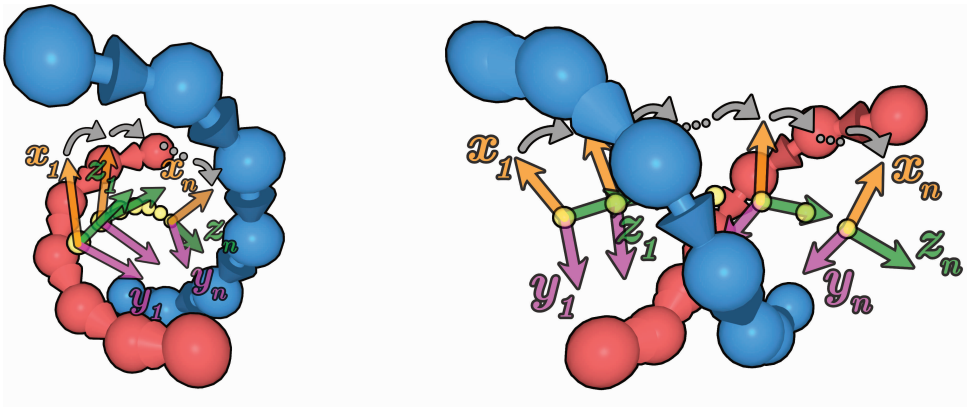


Figure S2: The moving frames $\mathbf{F}_k = (\mathbf{X}_k, \mathbf{Y}_k, \mathbf{Z}_k)$ is computed iteratively along the curve (yellow dots) such that $\mathbf{Z}_k$ is tangent to the curve. The nucleotides of the DNA helix following this curve are then positioned according to this moving frames.

## S1.5 Adaptive moving frame along a curve

As shown in fig. S3, our algorithm SA1 produces a smoother embedding of the DNA double helix embedding than the classic Frenet frame. Indeed the Frenet frame is very sensitive to any local change in curvature and tends to rotate erratically as can be observed in fig. S3(left), inducing unwanted torsion in the DNA helix mapping, while our adaptive frame keeps a consistent orientation along the whole curve, minimizing the overall torsion alonfg the DNA strand as can be observed in the lower part of the figure.

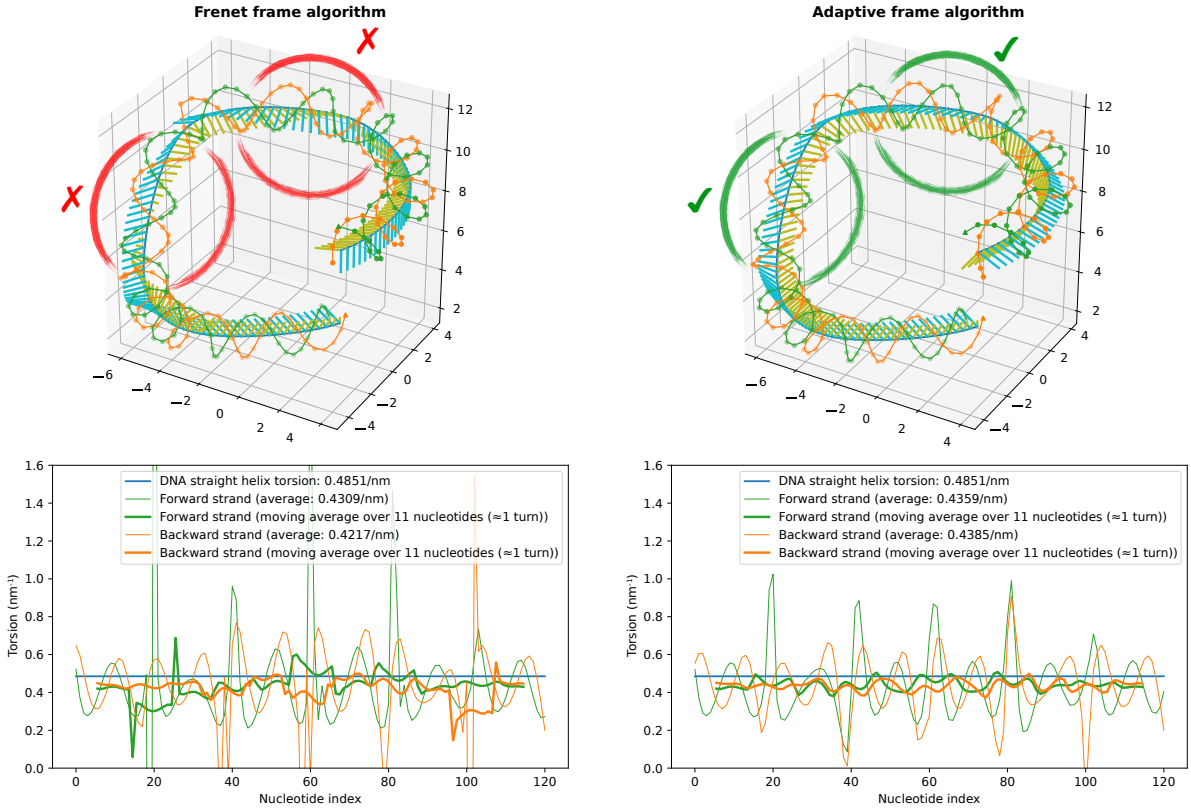


Figure S3: Frenet vs adaptive moving frame along a curve: the curve is shown in red and the computed frames at each nucleotide position are shown in green ($\mathbf{X}$) and cyan ($\mathbf{Y}$) ($\mathbf{Z}$ is not shown for clarity as it is always tangent to the curve). At the bottom: the values of the discrete torsion of the two forward and backward DNA strands in both models; in bold, the moving average taken over a full turn of each DNA strand shows that the iterative frame produces a smoother torsion whose value is closer to the torsion of a straight DNA helix.

## S1.6 Comparison of ENSnano curved DNA helix model with the human nucleosome core particle 2CV5 crystallographic data

Figures S5 and S6 evaluate the discrepancy between the DNA strands 1) as placed in space by ENSnano algorithm using the trajectory of the axis of the DNA helix in the human nucleosome core particle crystallographic data PDB-2CV5, and 2) as placed in the PDB file. Figure S6 compares the positions of the phosphates in both ENSnano model and crystallographic data. Figure S6 compares the positions of the nucleotides in both ENSnano model and crystallographic data. We observe a discrepancy of $0.444 \pm 0.219$ nm for the phosphates and $0.540 \pm 0.231$ nm for the nucleotides. Note that the DNA helix in the nucleosome core particle is constrained to adopt its shape by its interactions with the histones at its core, interactions which are not taken into account by ENSnano which relies on the sole trajectory of the helix to place the DNA strands.

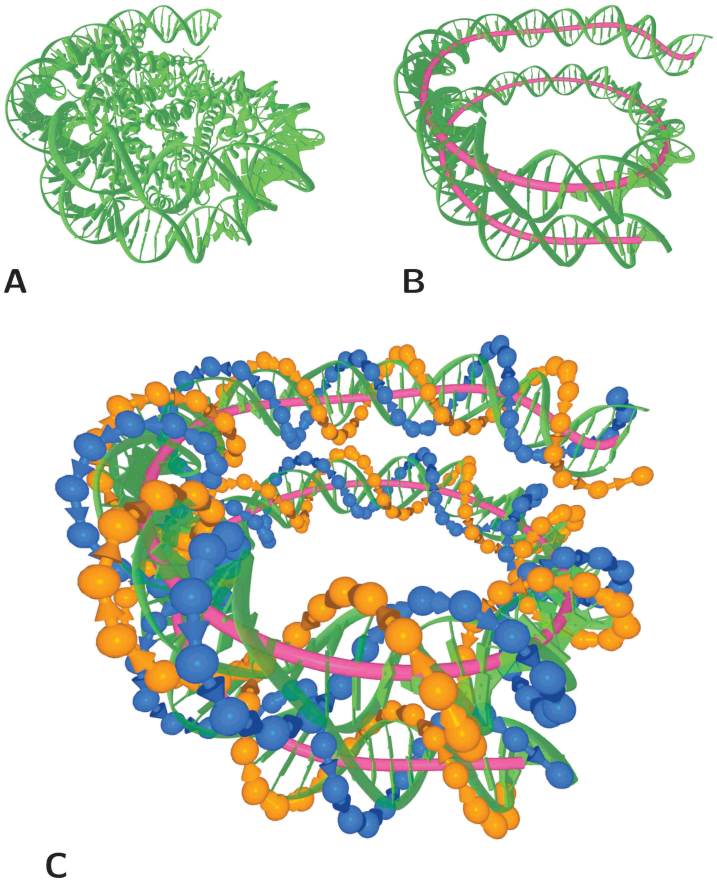


Figure S4: Curved DNA helix model generated by ENSnano from the crystallographic data of nucleosome. A) Crystallographic data PDB-2CV5; B) DNA helix axis trajectory $T$ (in pink) deduced from the PDB file; C) Curved DNA helix generated by ENSnano from the trajectory $T$ compared to the crystallographic data PDB-2CV5.

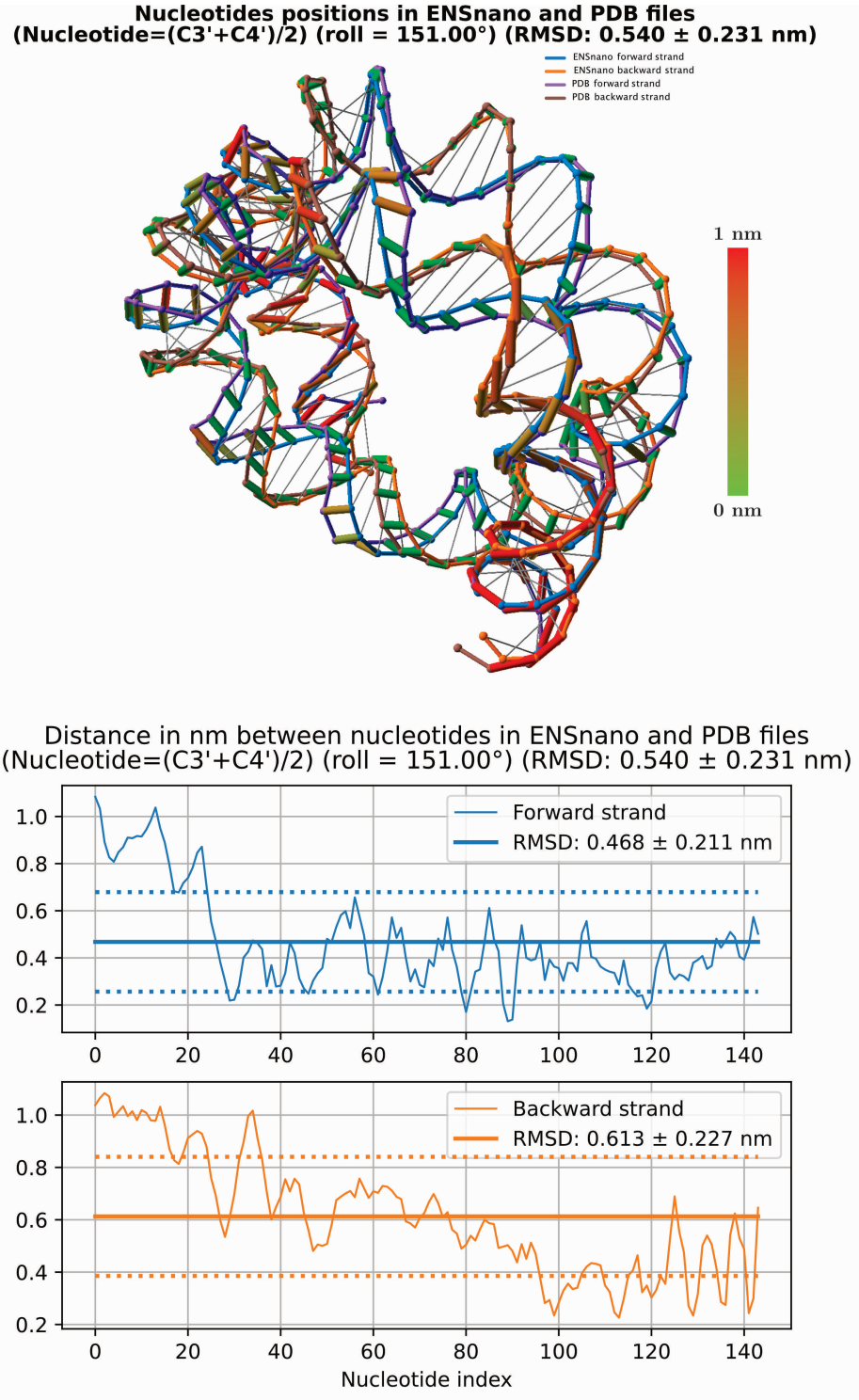


Figure S5: Our curved DNA helix model vs crystallographic data of nucleosome.

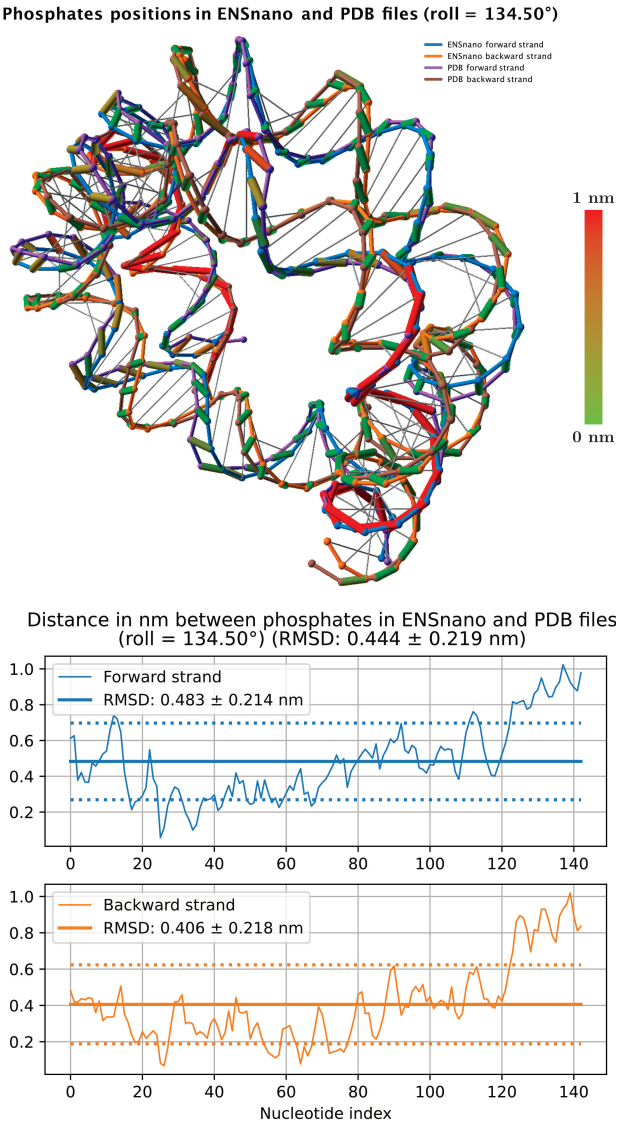


Figure S6: Our curved DNA helix model vs crystallographic data of nucleosome.

## S1.7 Curved DNA bundles

Curved DNA bundle are defined in ENSnano by attaching a grid to a Bezier curve as shown in fig. S7. The frames computed along the curve by algorithm SA1 are used to orient the grid. The grid can be either squared or honeycomb and has edges of length $H$ corresponding the target inter-helix axis distance (2.65 nm by default). The trajectory of each helix in the bundle simply follows the trajectory of the corresponding point in the grid along the curve (fig. S7B). To avoid self-collision of the origami design, each grid can be moved vertically at the control points of the Bézier curve as we did in our ⌘-origami (fig. S7D).

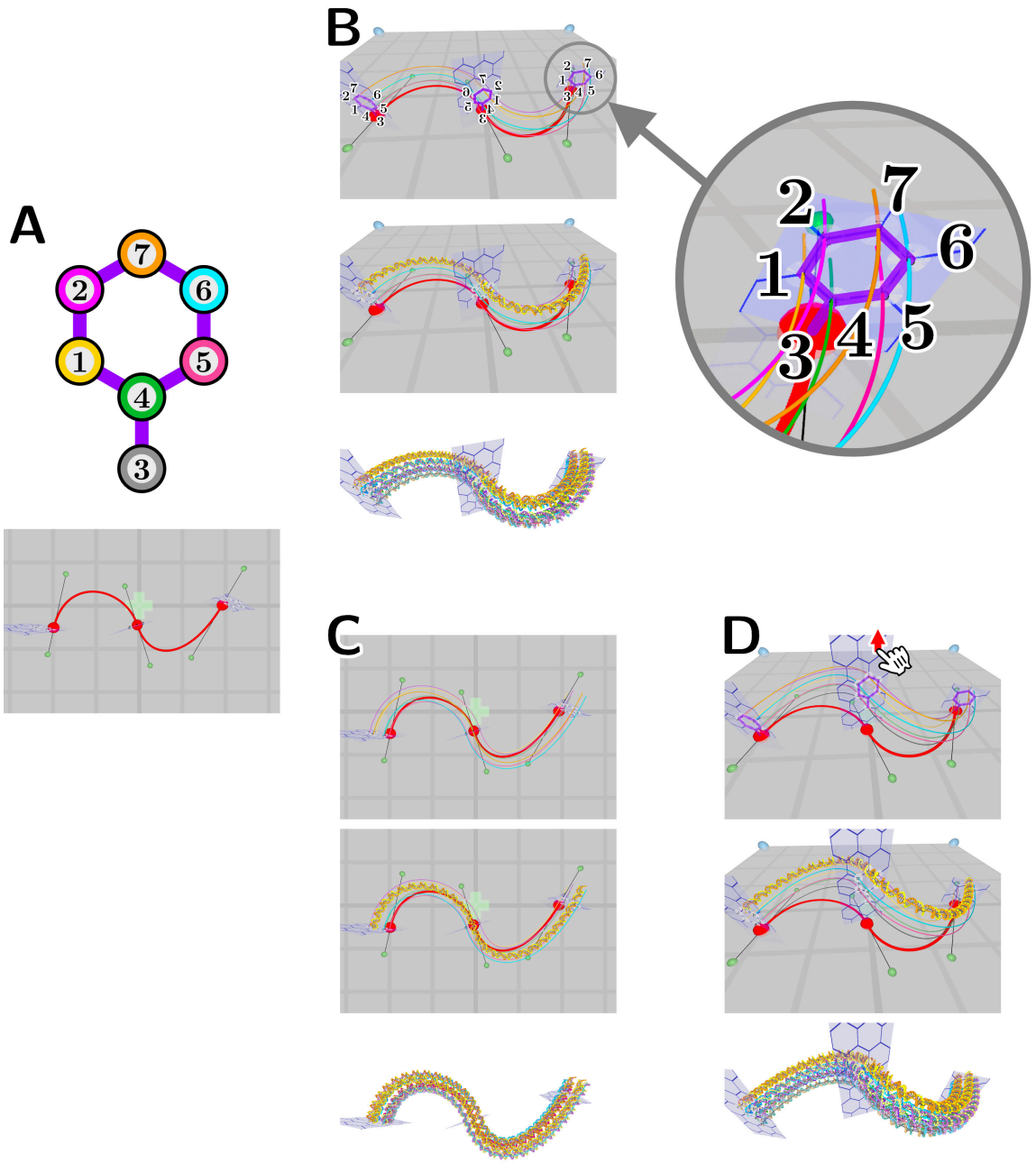


Figure S7: Grids-based routing of helices in curved DNA bundles: A) the helices' positions on the honeycomb grid; B) the trajectories of each helices is deduced by translating every point of the curve according to the grid; C) the resulting DNA bundle; D) grid can be moved vertically at Bézier control points, for instance to avoid self-collision.

## S1.8 2D embedding of curved DNA bundles

In ENSnano, DNA bundle helices trajectories are computed by translating the points of a Bézier curve according to the grid. It follows that we can use the grid to determine which nucleotides belongs to the same section of the DNA bundle and use this information to automatically align them in the 2D view as shown in fig. S8: even if the helices have very different lengths, their nucleotides are aligned accross them without the need for the user to add insertion nor deletion as one would do in caDNAno. ENSnano proceeds by automatically adapting the size of the cell of each nucleotide in the 2D view: enlarging/shortening it when the helix is shorter/longer respectively.

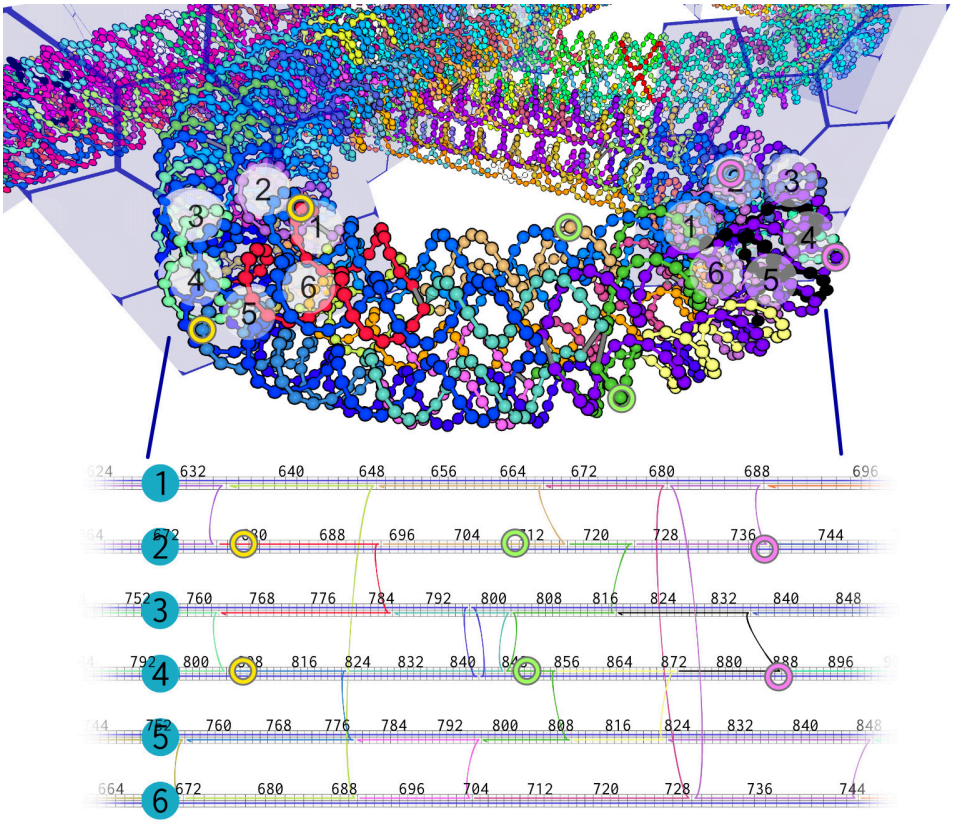


Figure S8: Automatic insertion- and deletion-less 2D embedding of curved DNA bundles: the circles mark nucleotides on helices 2 and 4 and their automatic positioning in the 2D view. Observe that even if helices 2 and 4 have very different lengths, their nucleotides belonging to the same section of the bundle are placed in the same section in the 2D view.

## S1.9 DNA parameters adjustment for closed curves

Closed (curved) DNA helices require special care as their strands need to wrap upon themselves, see fig. S9. DNA bundles require furthermore adjustment and will be handled in the next section. Single closed DNA helices are handled in a three steps process that aims at spreading the constraints evenly over the whole curve:

1. *Tune the rise:* the first step consists in tuning minimally the rise so that the length of curve corresponds to an integral number of base pairs. Let $L$ be the length of the Bézier curve. Let $N = \lfloor L/\Delta \rceil$ be the rounded number of base pairs fitting into the curve. We set $\tilde{\Delta} = L/N$ be the adjusted rise of DNA for this curve. Note that $\tilde{\Delta}$ differs from $\Delta$ by at most $\Delta/2N$ which is a few ‰ as soon as $N \gtrsim 200$.
2. *Compute the frames:* Use algorithm SA1 to compute the frames at every position and map the DNA strands along the curve accordingly.
3. *Tune the helicity:* the last step consists in aligning the angle of both ends of the strands, see fig. S11. Let $\Theta \in [-\pi, \pi)$ denotes the angle that the virtual $N+1$-th nucleotide makes with the 1st of the strand. We set $\tilde{\alpha} = \alpha - \Theta/N$ so that the angle difference gets compensated little by little over the whole length of the strand bringing both ends together. Note that, again, the relative difference between $\tilde{\alpha}$ and $\alpha$ is less that $\pi/N$ which accounts for a few ‰ as soon as $N$ is larger than a few hundred. Equivalently, we set $\tilde{\chi} = 1/(1/\chi - \Theta/N)$ so that $2\pi N/\tilde{\chi} = 2\pi N/\tilde{\chi} - \Theta$.

This process is motivated by the fact that we believe that the constraints on the rise (optimized first) are tighter than the constraints on the twist (optimized second) which can be absorbed by the DNA flexibility as was demonstrated by the variety of origamis which were designed an assembled successfully with helicity ranging from 10.2 to 10.8 base pairs per turn. Note that these adjustments are below the currently known precision on these parameters as soon as $N \gtrsim 500$, that is for strands of $\gtrsim 150$ nucleotides-long.

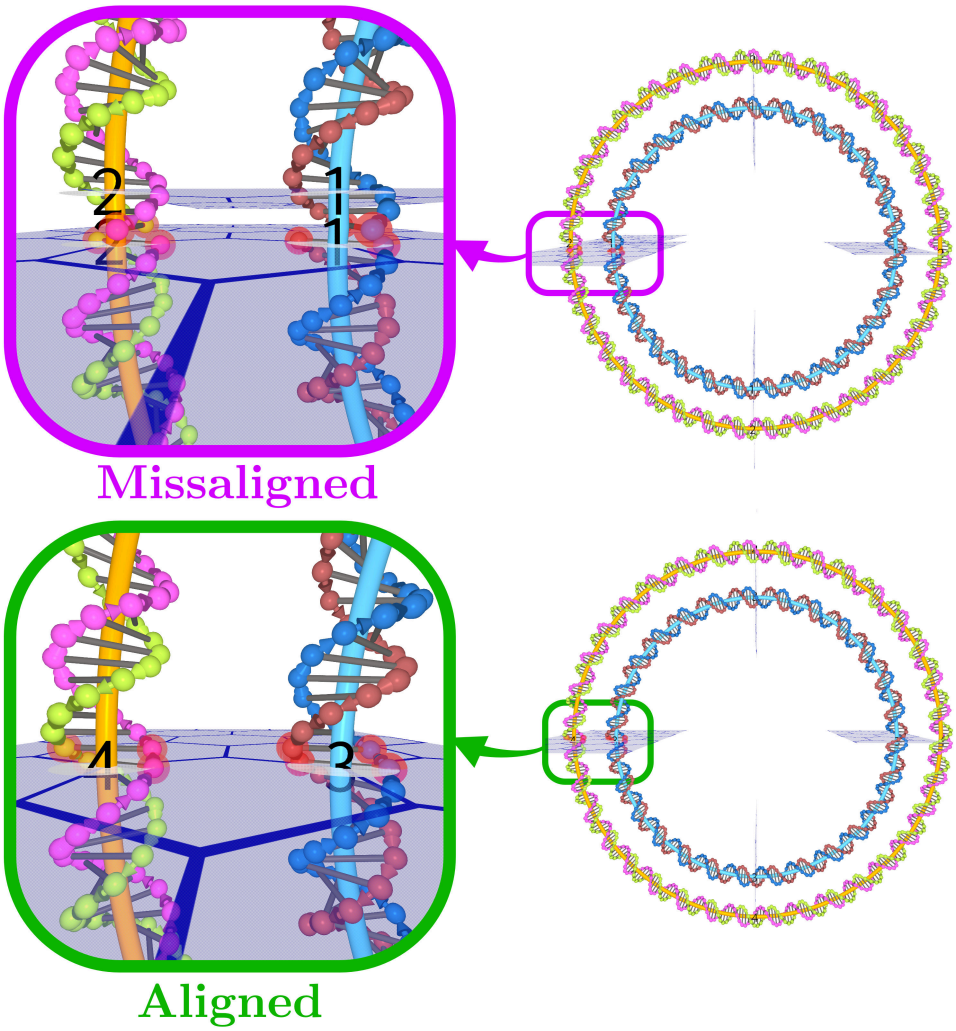


Figure S9: Rounding closed curve's length, twist so that both of its ends match

DNA helix bundles require furthermore adjustments of the parameters because in order for both ends of shifted curves to match, we need to align also the initial and final frames as shown in fig. S10. We proceed by modify Step 2 as follows:

2'. *Compute and adjust the frames for the Bézier curve supporting the DNA bundle:* Use algorithm SA1 to compute the frames at every position. Let $\Theta \in [-\pi, \pi)$ be the angle between the virtual $N+1$-th frame and the 1st. For $i = 1..N$, rotate the $i$-th frame $F_i$ by $-i \times \Theta/N$ around its $\mathbf{Z}$ axis to absorb $\Theta$ (see fig. S10). Interpolate using piecewise Bézier curves or Chebyshev polynomials the trajectories of the grid-points by which passes the helices of the bundle, as illustrated in fig. S10)(bottom). Finally, run the three steps in the section above for each of these trajectories as shown in fig. S11.

Note that each helix of the closed-curved bundle has its own adjusted rise and twist (or helicity). The resulting helix 3D embedding is shown in fig. S12.

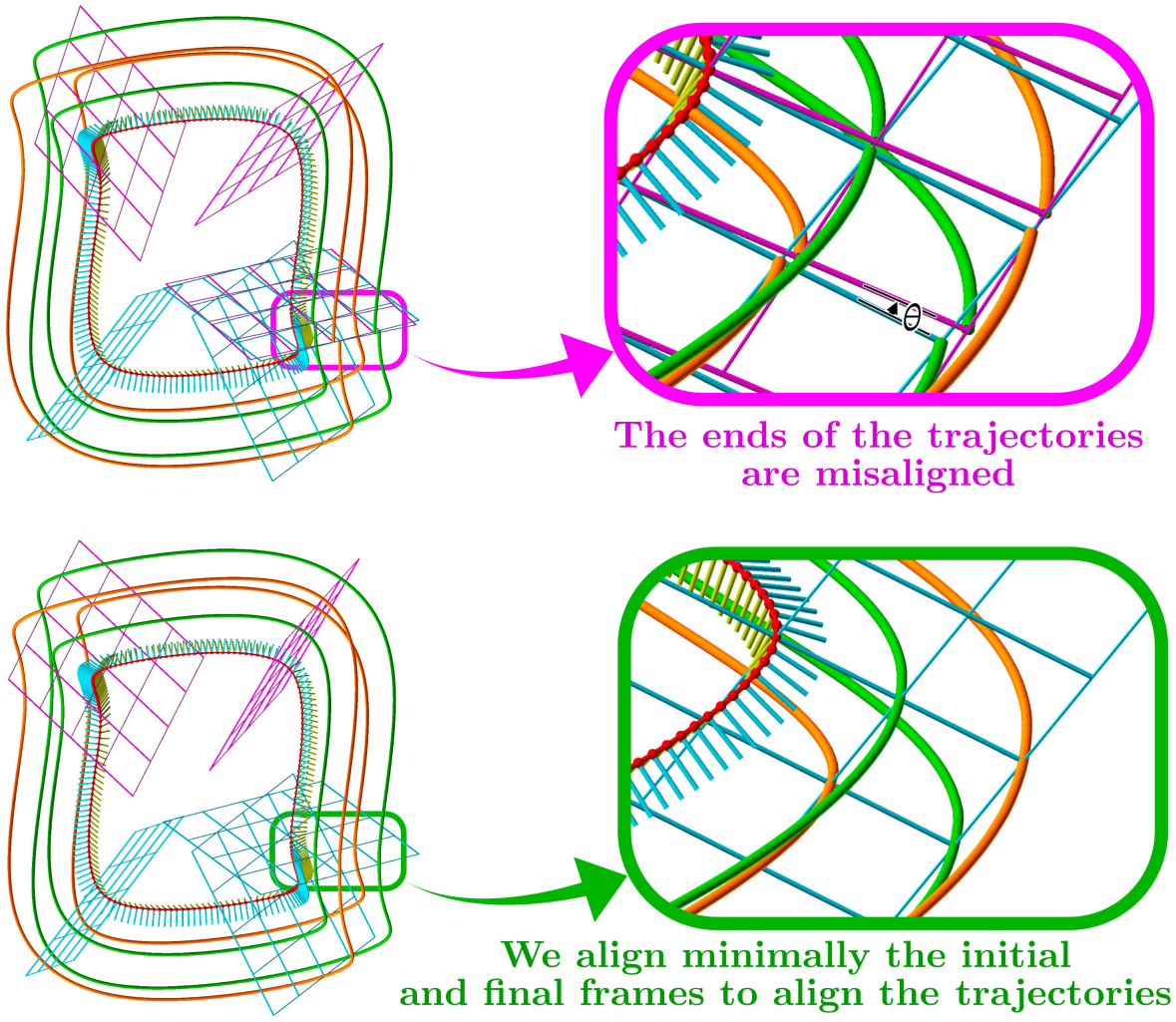


Figure S10: The case of closed curve bundle: 1) Adapt the DNA helix' rise so that the curve's length corresponds to an integer number of base pairs, then compute the iterative frames and rotate them progressively and minimally so that both of initial and final frames match

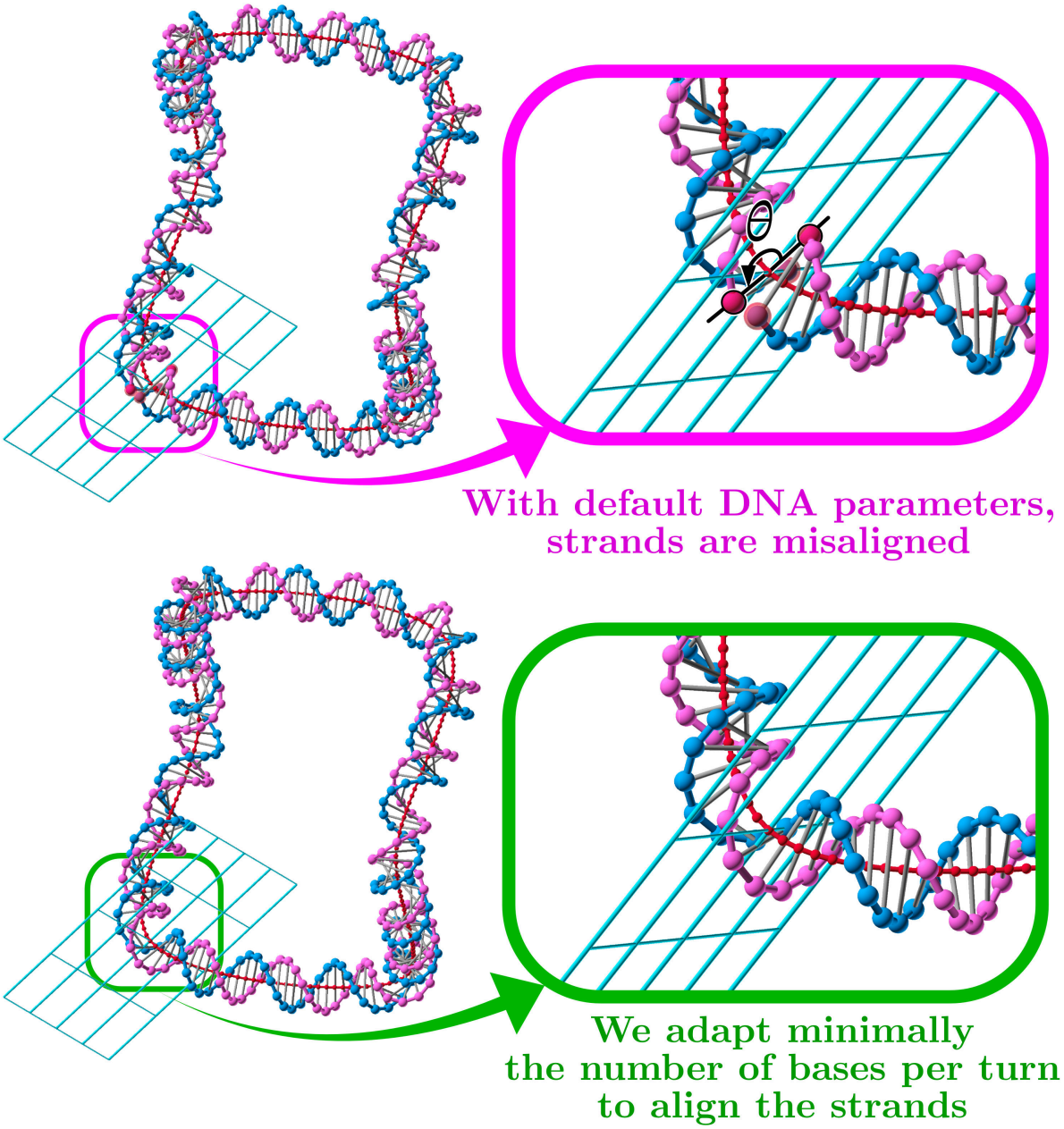


Figure S11: The case of closed curve bundle: 2) Adapt the helicity parameter minimally so that the ends of both strands align.

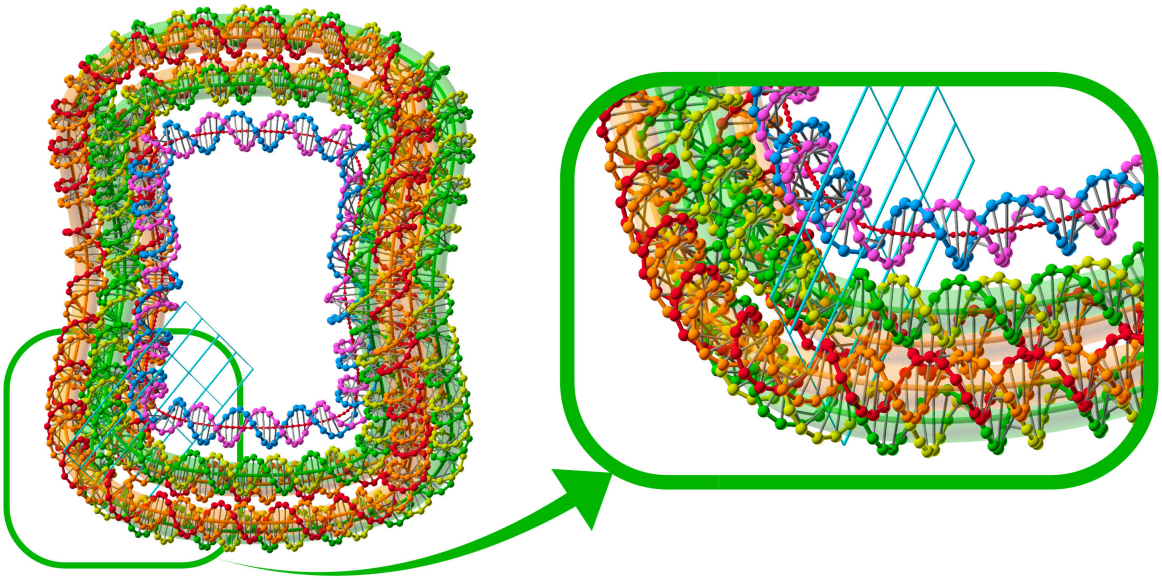

Figure S12: The case of closed curve bundle: 3) Finally, compute the frames and adapt the helix parameters as before for each shifted helix independently, resulting in closed DNA helices respecting the desired inter distance everywhere.

# S2 A four-loops bundle, Figures S13 to S35

## S2.1 General design of the four-loops bundle

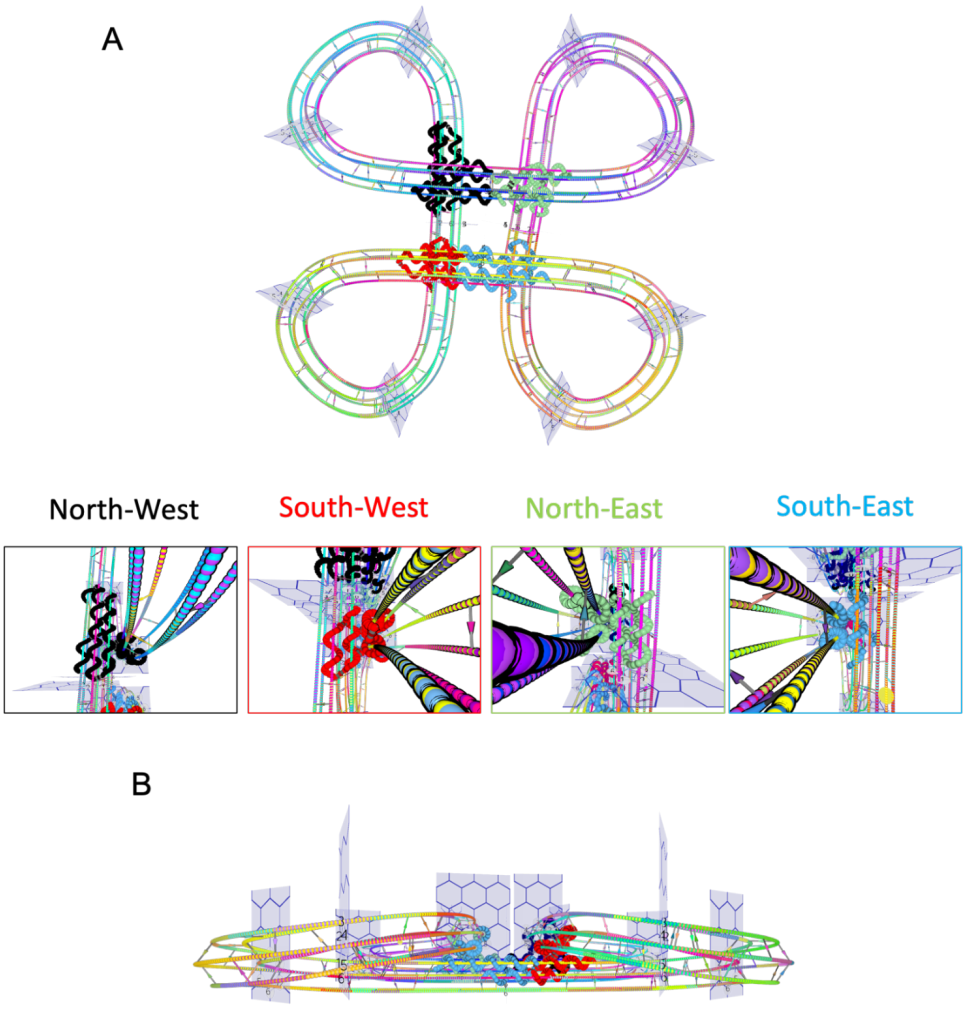


Figure S13: 3D view of the ⌘-origami design, line representation. A: Back view of the full design and side views of the four junctions (North-West, South-West, North-East, South-East). The staples involved in the junctions are displayed in helix representation (in black for North-West, red for South-West, green for North-East and blue for South-East) ; B: Bottom view. Each line represents a double helix of DNA. Transversal bars represent crossovers. The staples shown here are the core staples of the origami, the staples involved in the four junctions (NW, NE, SW, SE) and the staples of the origami in the close state.

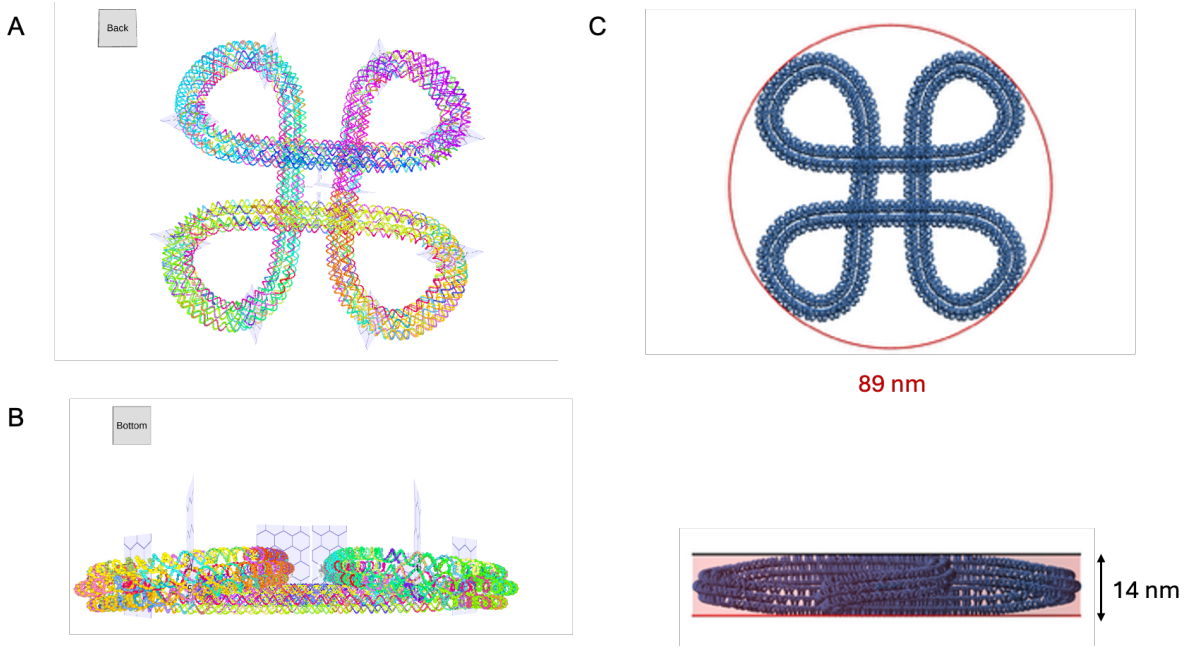


Figure S14: 3D view of the ⌘-origami design, helix representation. A: Back view; B: Bottom view. Each ball represents a deoxynucleotide. The staples shown here are the core staples of the origami, the staples involved in the four junctions (NW, NE, SW, SE) and the staples of the origami in the close state; C: Dimensions of the ⌘-origami. Top view (up), side view (bottom). Diameter of 89 nm (red circle), height of 14 nm.

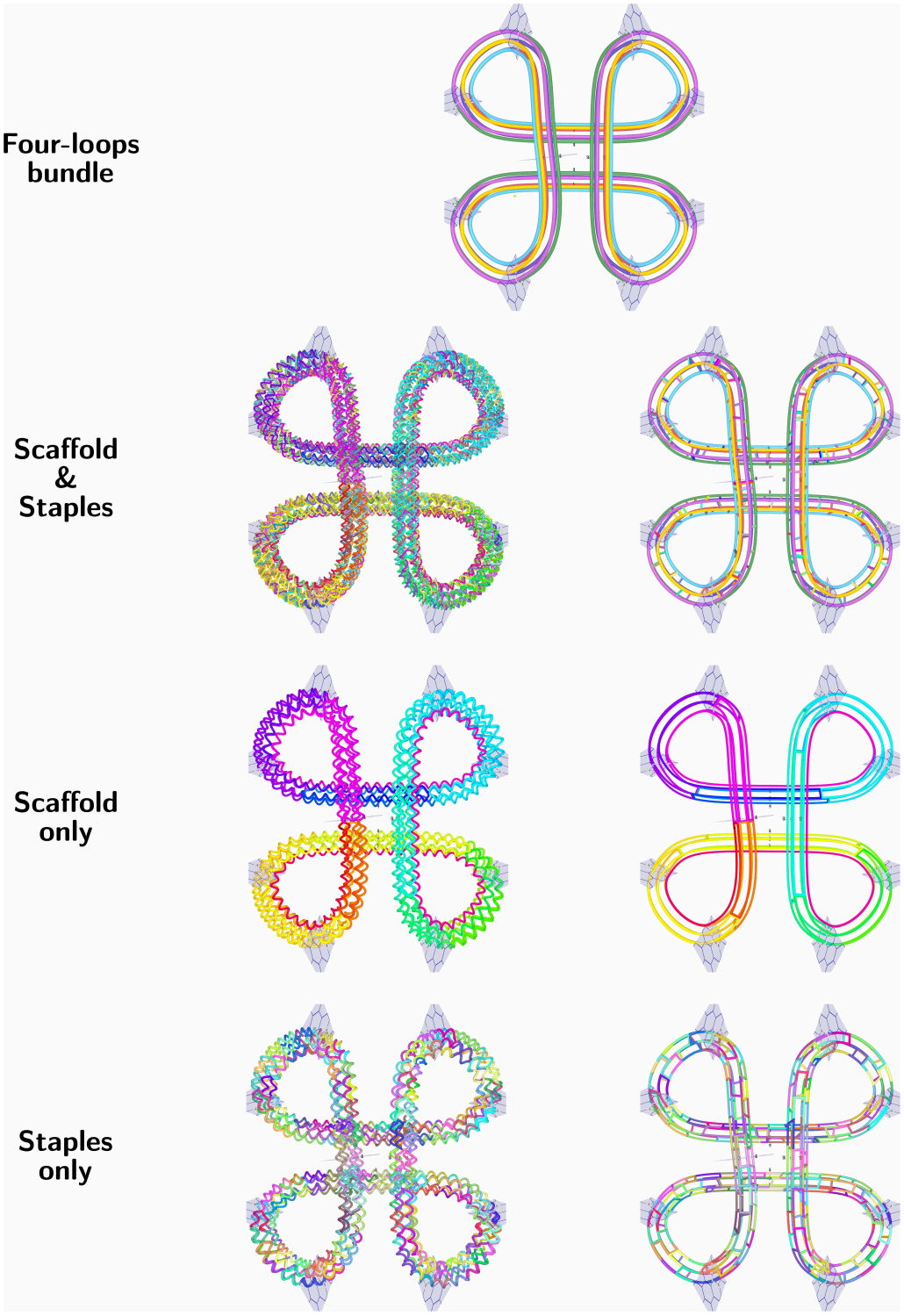


Figure S15: 3D view of the ⌘-origami design, helix (left) and line (right) representations. Bottom views of the six helices trajectories (top), the scaffold and staples together (middle up), the scaffold alone (middle down) and the staples alone (bottom). Transversal bars on the line representation represents a crossover. The staples shown here are the core staples of the origami, the staples involved in the four junctions (NW, NE, SW, SE) and the staples of the origami in the close join state.

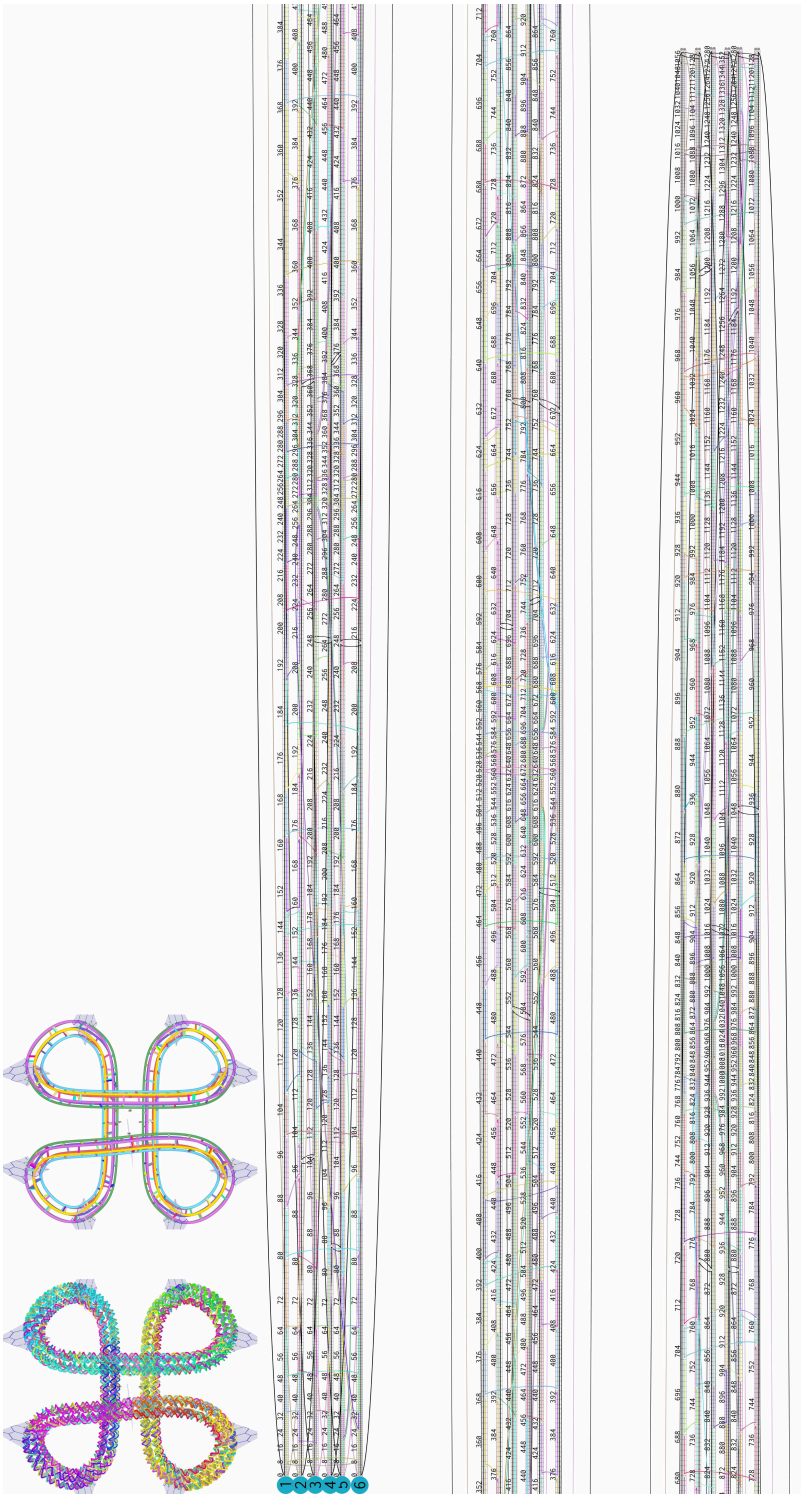

Figure S16: 2D view of the ⌘-origami design. Scaffold and staples. The staples shown here are the core staples of the origami, the staples involved in the four junctions (NW, NE, SW, SE) and the staples of the origami in the close state.

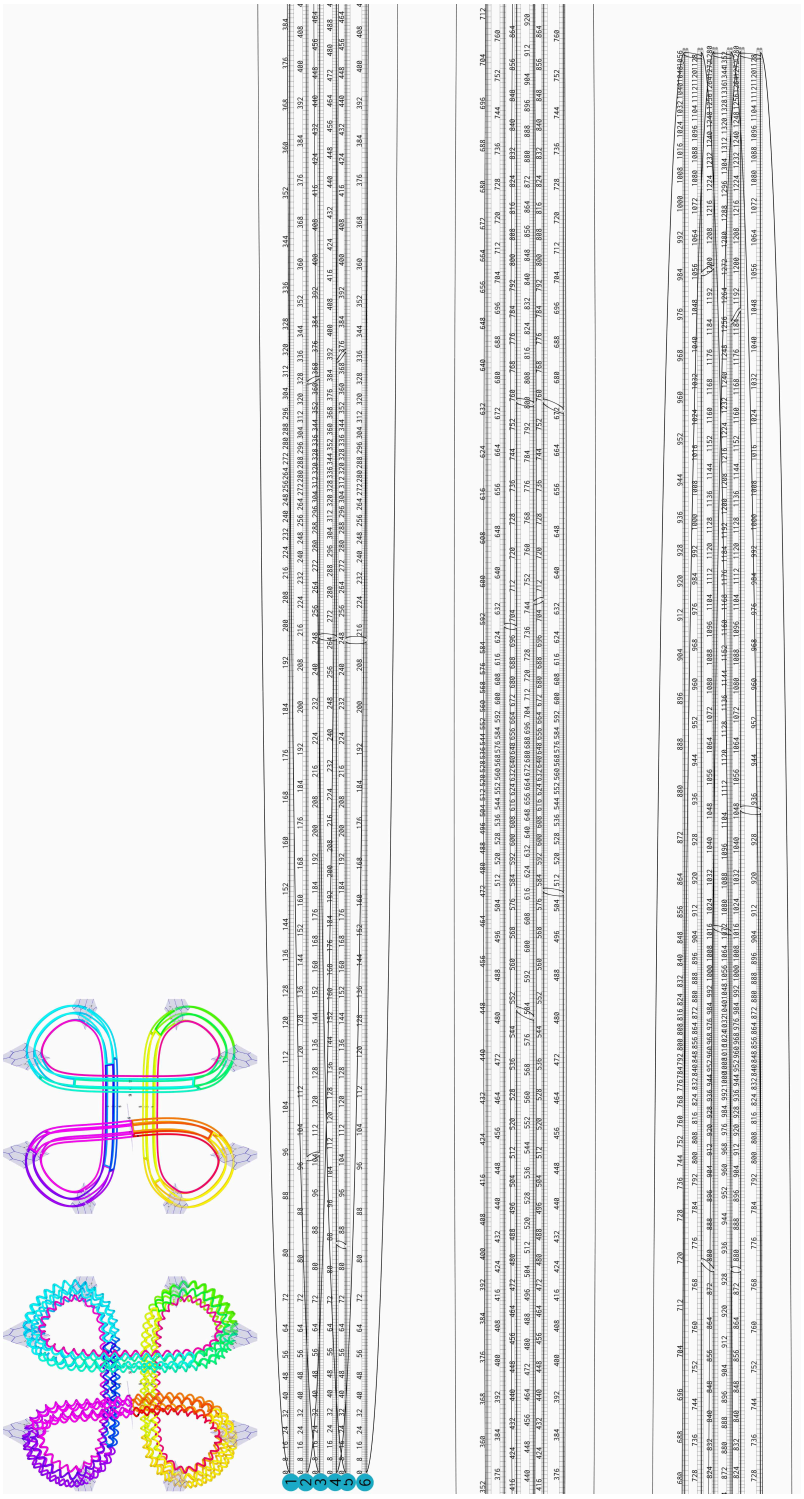

Figure S17: 2D view of the ⌘-origami design. Scaffold only.

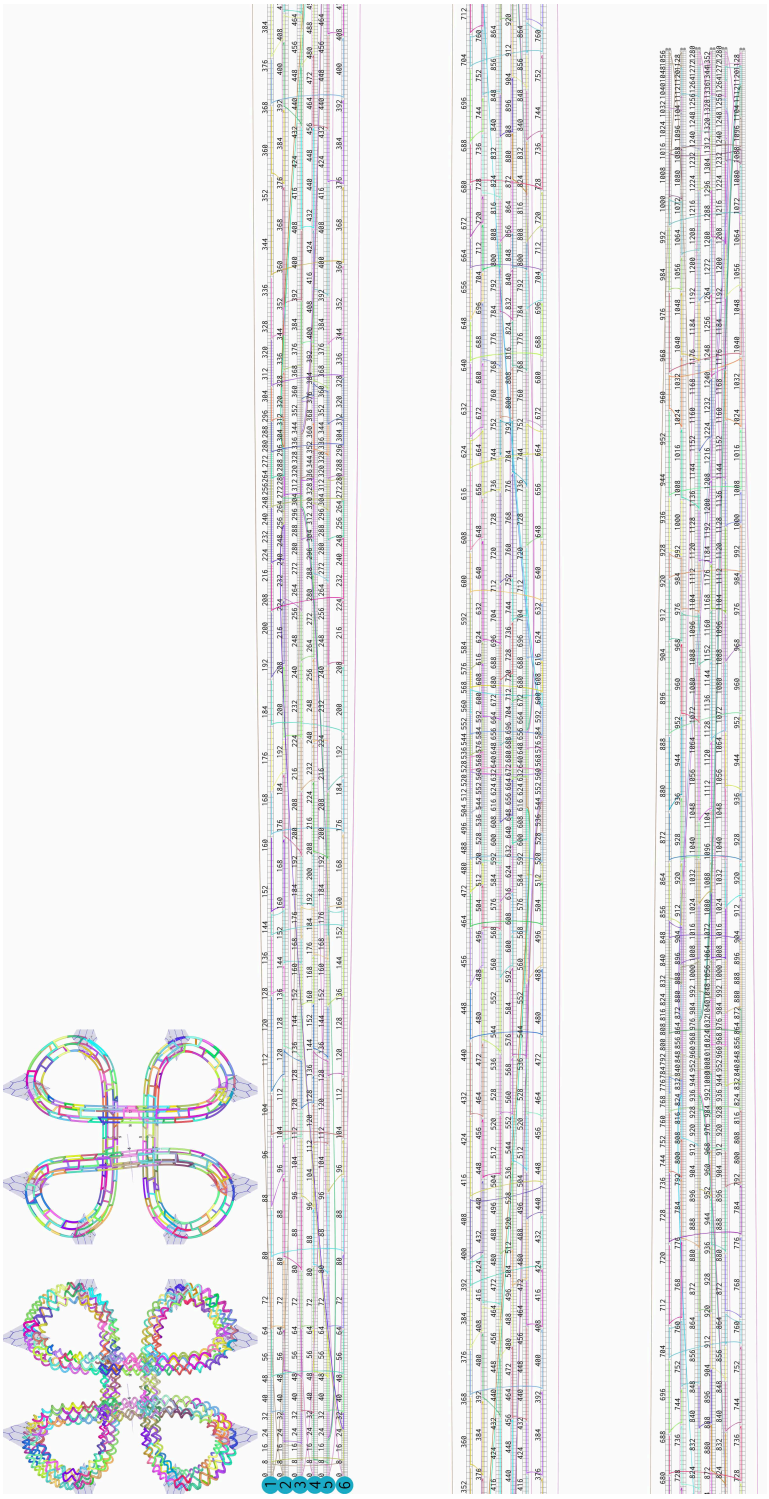

Figure S18: 2D view of the ⌘-origami design. Staples only. The staples shown here are the core staples of the origami, the staples involved in the four junctions (NW, NE, SW, SE) and the staples of the origami in the close state.

## S2.2 Patterning of scaffold and staples

In the ⌘-origami design, we used the classic ”leaf-shaped” scaffold consisting of several copies of the same leaf-pattern as illustrated in fig. S19

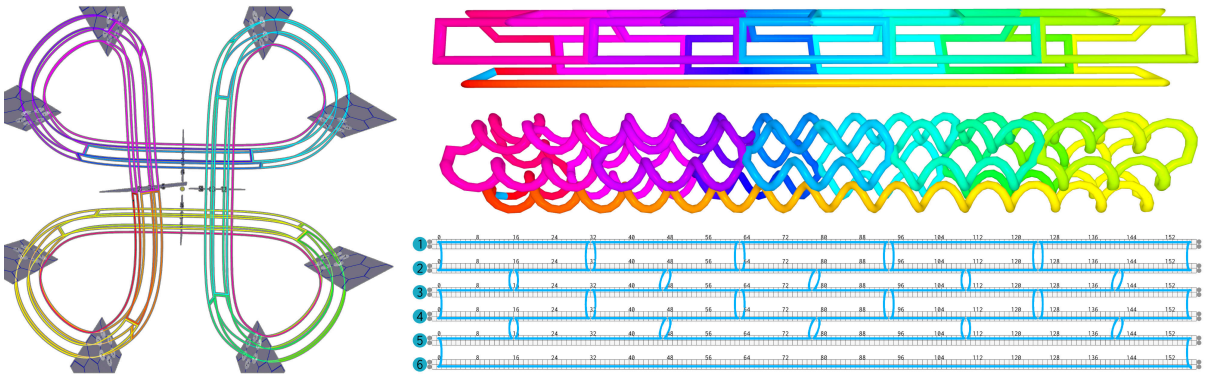

Figure S19: Leaf-shaped scaffold principle used in the ⌘-origami.

In all our designs, we favored the C-shaped staples pattern as illustrated in fig. S20.

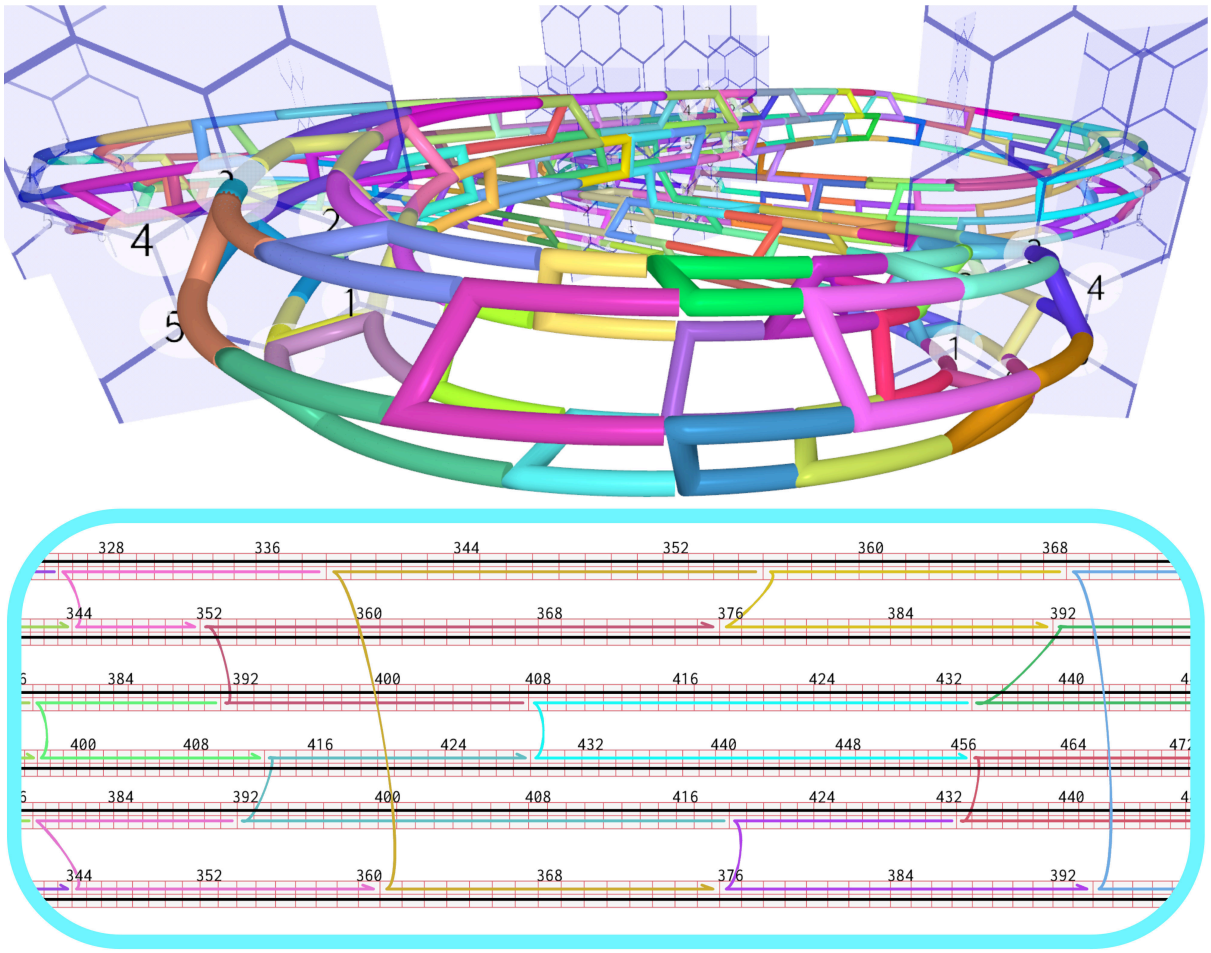


Figure S20: C-shaped staples principle used in every one of our origamis (illustrated here with the ⌘-origami).

## S2.3 Experimental validation of the design of the four-loops bundle

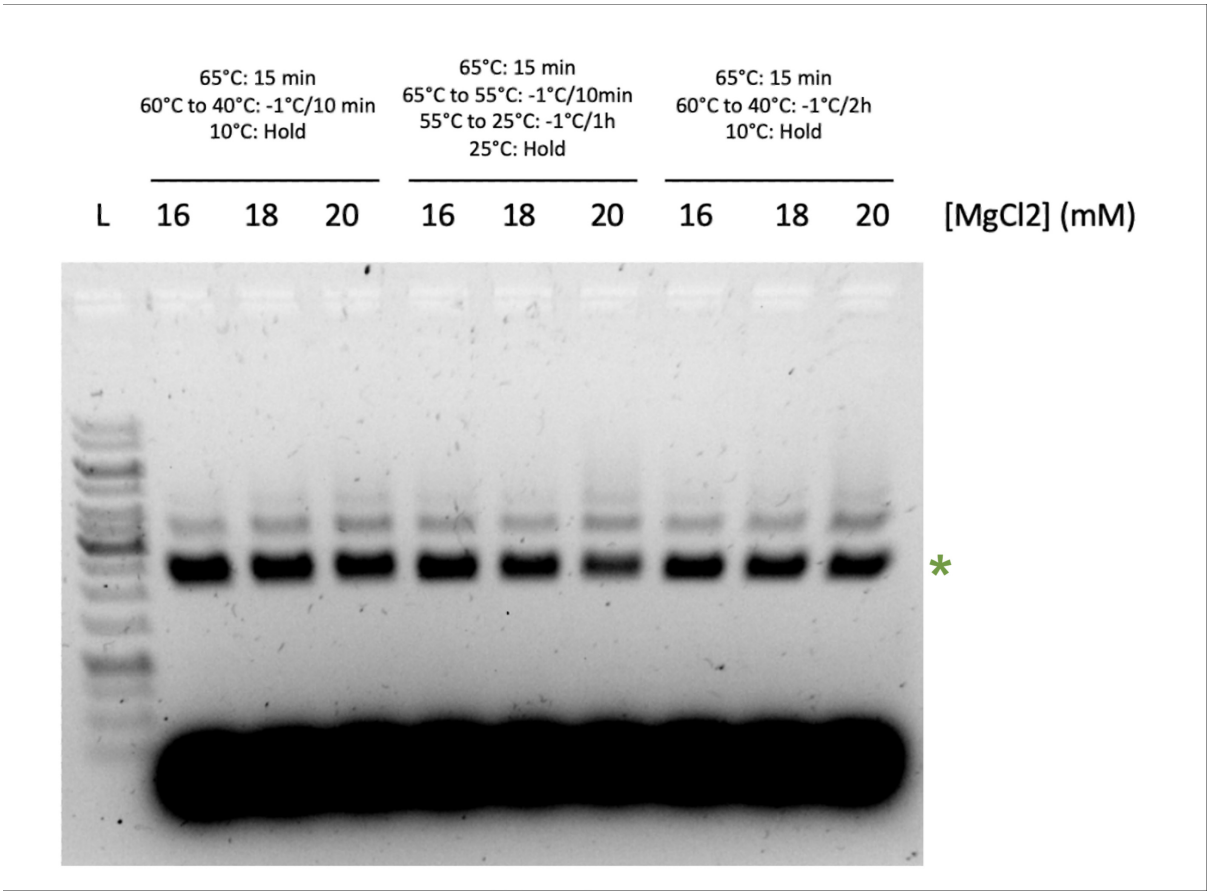


Figure S21: Gel analysis of the influence of $MgCl_2$ concentration and different folding ramps on folding quality of the ⌘-origami. The foldings were analyzed by agarose gel electrophoresis (1%). L: 1kb DNA ladder.

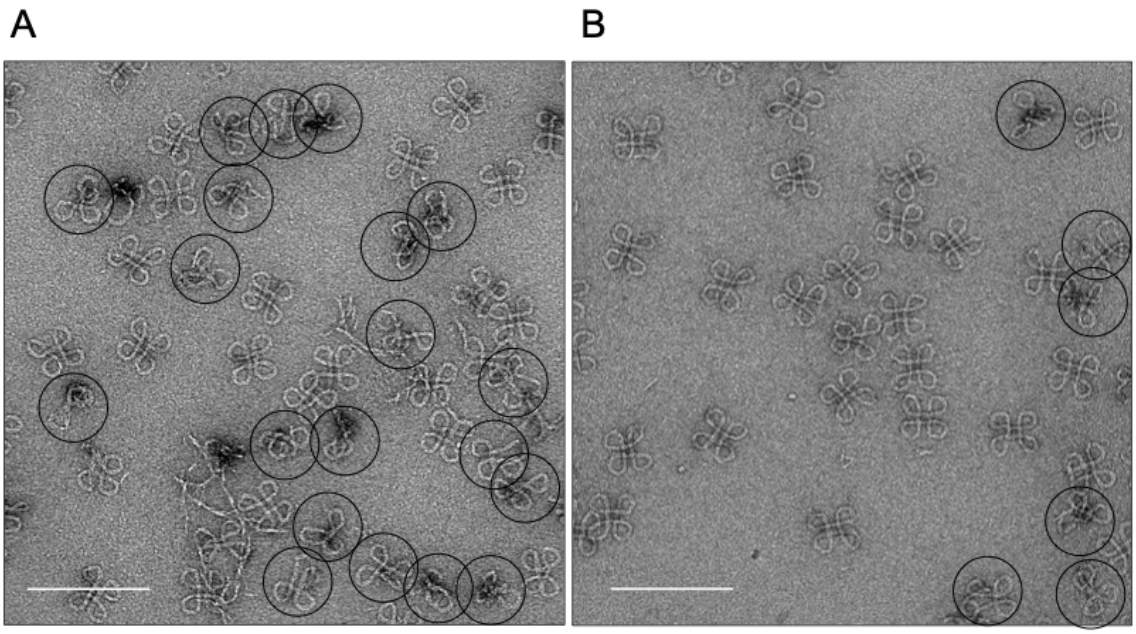


Figure S22: Transmission Electron Microscope (TEM) micrographs of purified ⌘-origami folded with 20 mM $MgCl_2$ with different folding ramps. A: ⌘-origami folded with the following folding ramp: 65°C during 15 minutes, 60°C to 40°C -1°C/10 minutes, 10°C Hold ; B: ⌘-origami folded with the following folding ramp: 65°C during 15 minutes, 60°C to 40°C -1°C/2h, 10°C Hold. Particles not folded in the full ⌘-origami are circled in black. Scale bar is 200 nm.

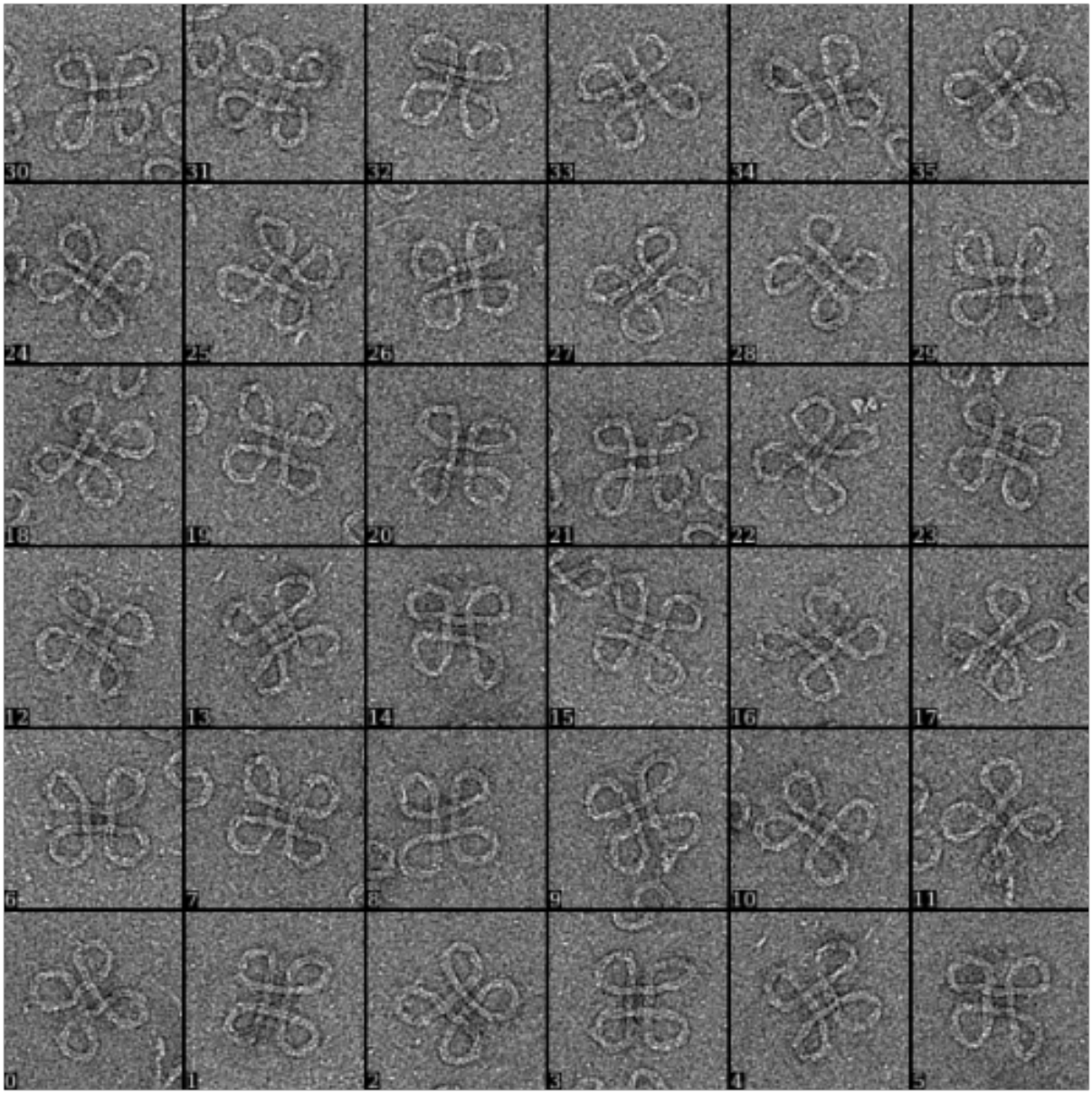

Figure S23: Transmission Electron Microscope (TEM) micrographs of typical particles of the ⌘-origami in optimal folding conditions. Each box is 132 nm x 132 nm.

## S2.4 Open/close and junctions design variants

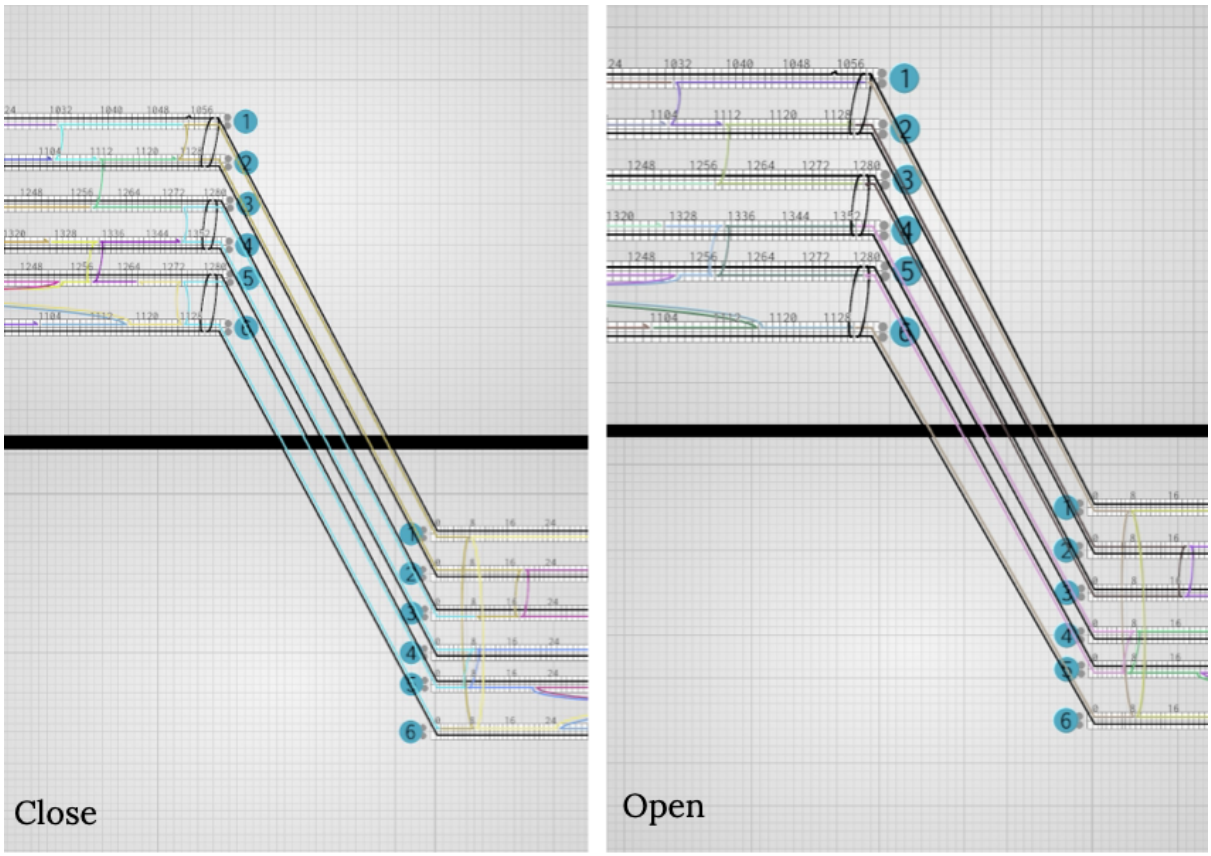


Figure S24: 2D view of the ⌘-origami design. View of the close state design (left) and the open state design (right). The open-T state design is the same as the open state design with extra poly-Ts added to prevent stacking. The scaffold is represented in black, staples in colors. For each representation, a horizontal bold black line splits the 2D view into two parts corresponding to the two ends of the bundle.

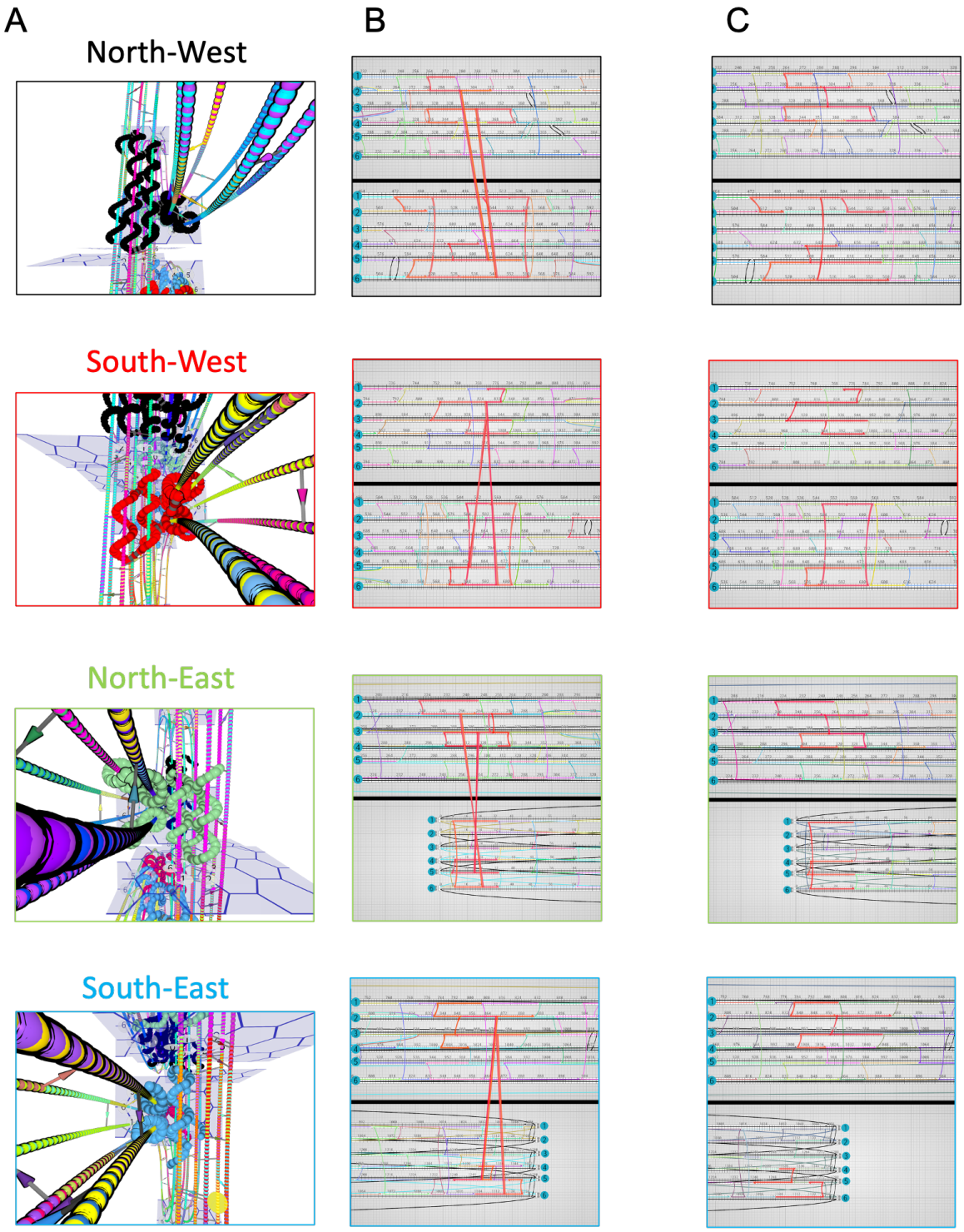


Figure S25: 3D and 2D views of the junctions of the ⌘-origami design. A: 3D side views of the four junctions with line representation (North-West, South-West, North-East, South-East). The staples involved in the junctions are displayed in helix representation (in black for North-West, red for South-West, green for North-East and blue for South-East); B: 2D views of the junctions' designs. The staples in bold red are the staples involved in the junctions. For each representation, a horizontal bold black line split the 2D view into two parts corresponding to the two layers of the ⌘-origami that we can see in the 3D view ; C: 2D views of the design of the junctions' locations when the junction is not made. The staples in bold red are the staples involved in the junctions, without making crossovers between the layers in this case.. For each representation, a bold black line splits the 2D view into two parts corresponding to the two layers of the ⌘-origami that we can see in the 3D view.

## S2.5 Study of different conformations of the four-loops bundle depending on the design

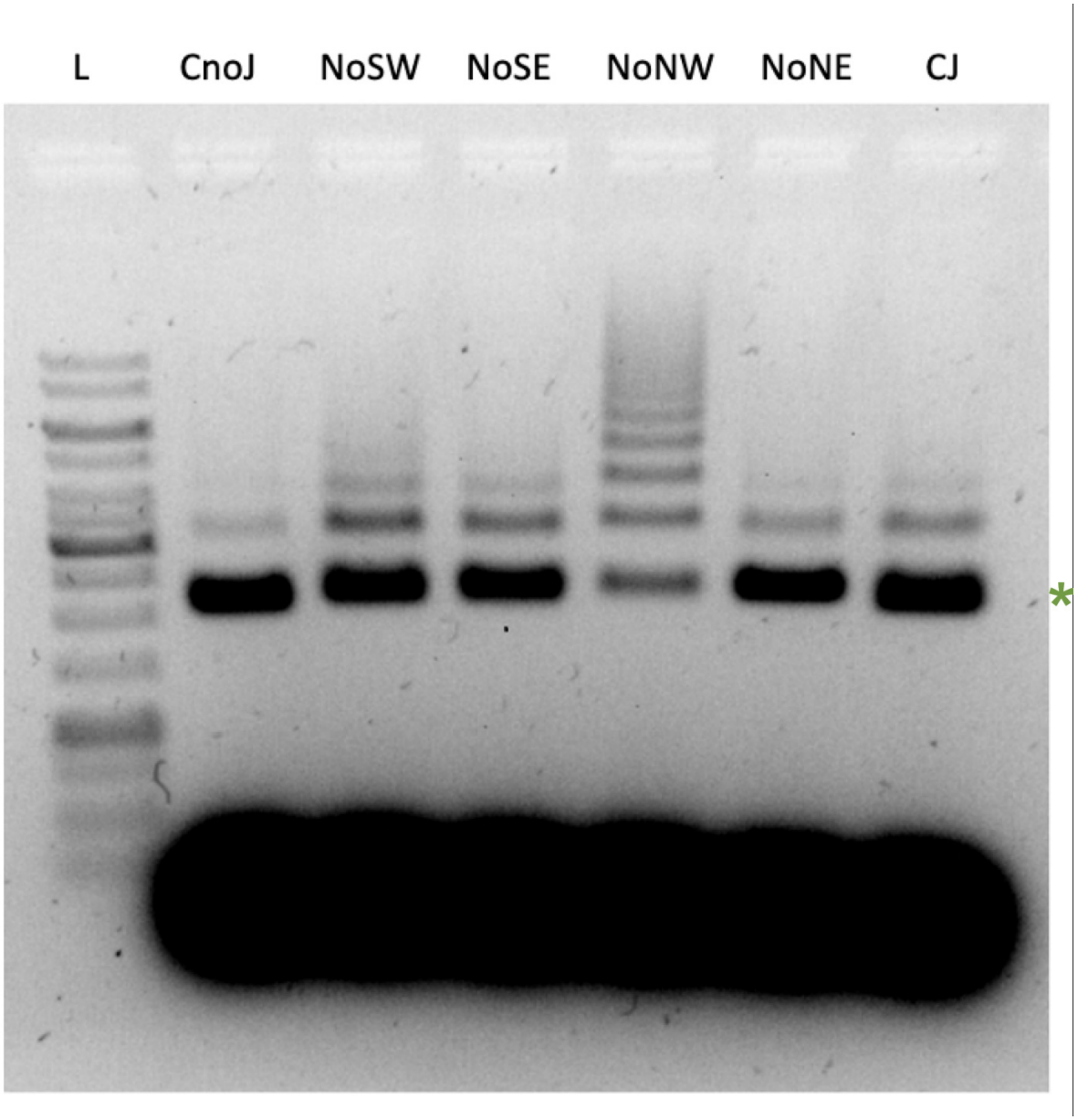


Figure S26: Gel analysis of the influence of the presence of junctions on the folding of the ⌘-origami. The foldings were analyzed by agarose gel electrophoresis (1%). L: 1kb DNA ladder ; CnoJ: ⌘-origami folded in the close state without the junctions NW, NE, SW, SE ; NoSW: ⌘-origami folded in the close state without the junction SW but with the junctions NW, NE, SE ; NoSE: ⌘-origami folded in the close state without the junction SE but with the junctions NW, NE, SW ; NoNW: ⌘-origami folded in the close state without the junction NW but with the junctions SW, NE, SE ; NoNE: ⌘-origami folded in the close state without the junction NE but with the junctions NW, SW, SE ; CJ: ⌘-origami folded in the close state with the junctions SW, NW, NE, SE.

Figure S27: Various structural conformations expected using plumber pipes linked with 3/4-turns corners.

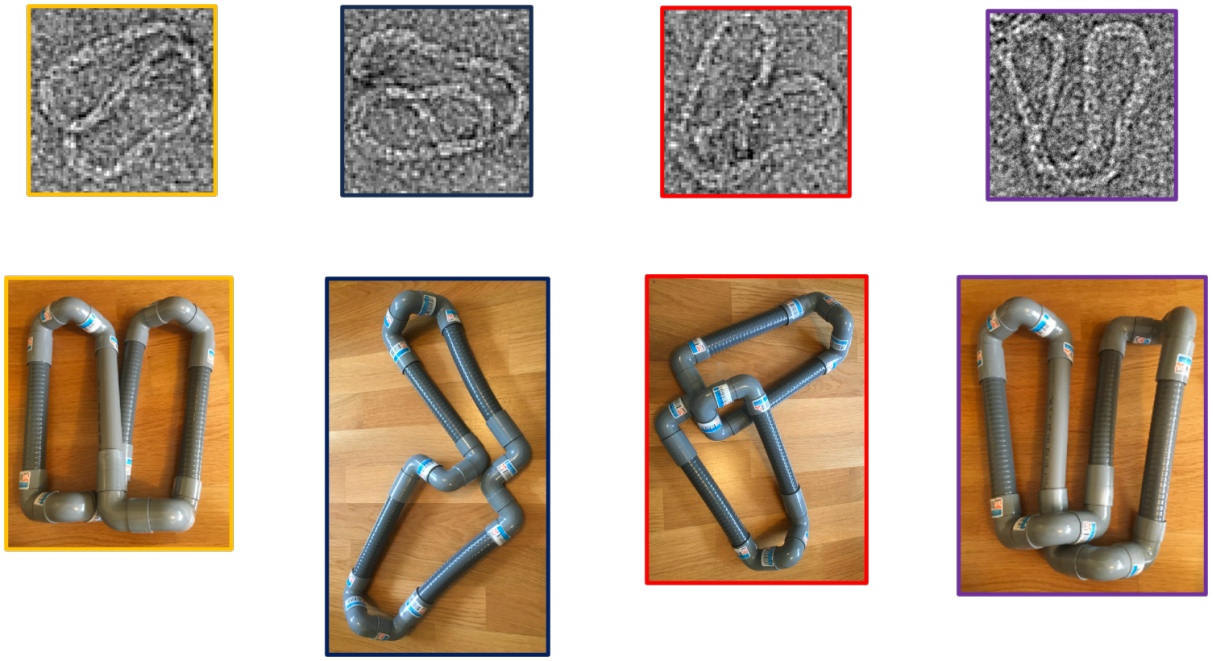

Figure S28: Realization of various shapes observed in Transmission Electron Microscope (TEM) micrographs of purified ⌘-origami using plumber pipes linked with 3/4-turns corners. ⌘-origami folded in the close state, without the junctions NE, SE, NW, SW. Box size of the TEM micrographs = 100 nm.

Interestingly, we observed that some origami folded in the full ⌘-shape even though only one of the four junctions was present, with a better yield when using the staples involved in the NW junction alone than with the other junctions (figs. S29 and S30).

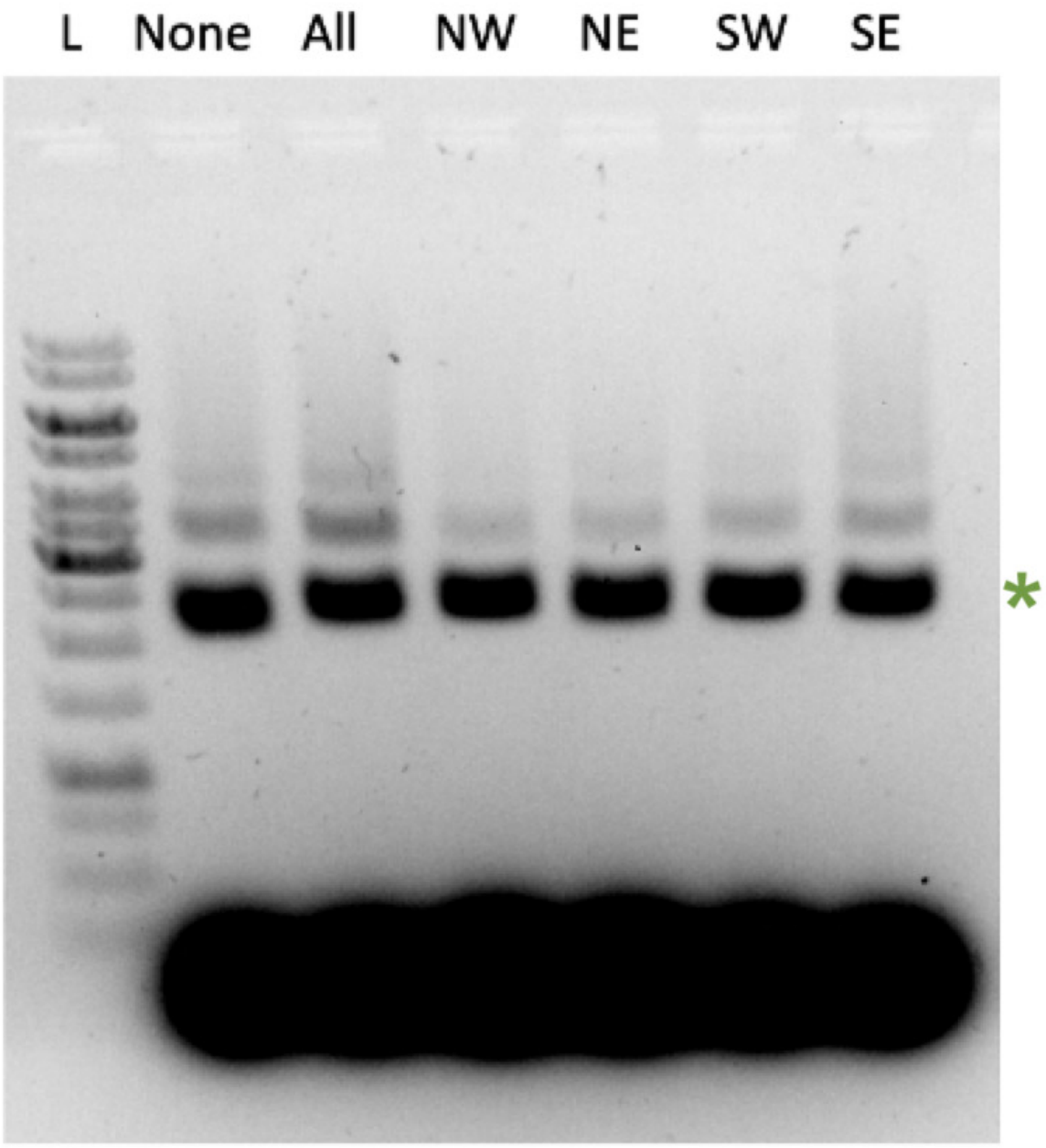


Figure S29: Gel analysis of the influence of the presence of junctions on the folding of the ⌘-origami. The foldings were analyzed by agarose gel electrophoresis (1%). L: 1kb DNA ladder ; None: ⌘-origami folded in the close state without the junctions NW, NE, SW, SE ; All: ⌘-origami folded in the close state with the junctions SW, NW, NE, SE ; NW: ⌘-origami folded in the close state with the junction NW and without the junctions SW, NE, SE ; NE: ⌘-origami folded in the close state with the junction NE and without the junctions SW, NW, SE ; SW: ⌘-origami folded in the close state with the junction SW and without the junctions NW, NE, SE ; SE: ⌘-origami folded in the close state with the junction SE and without the junctions SW, NE, NW.

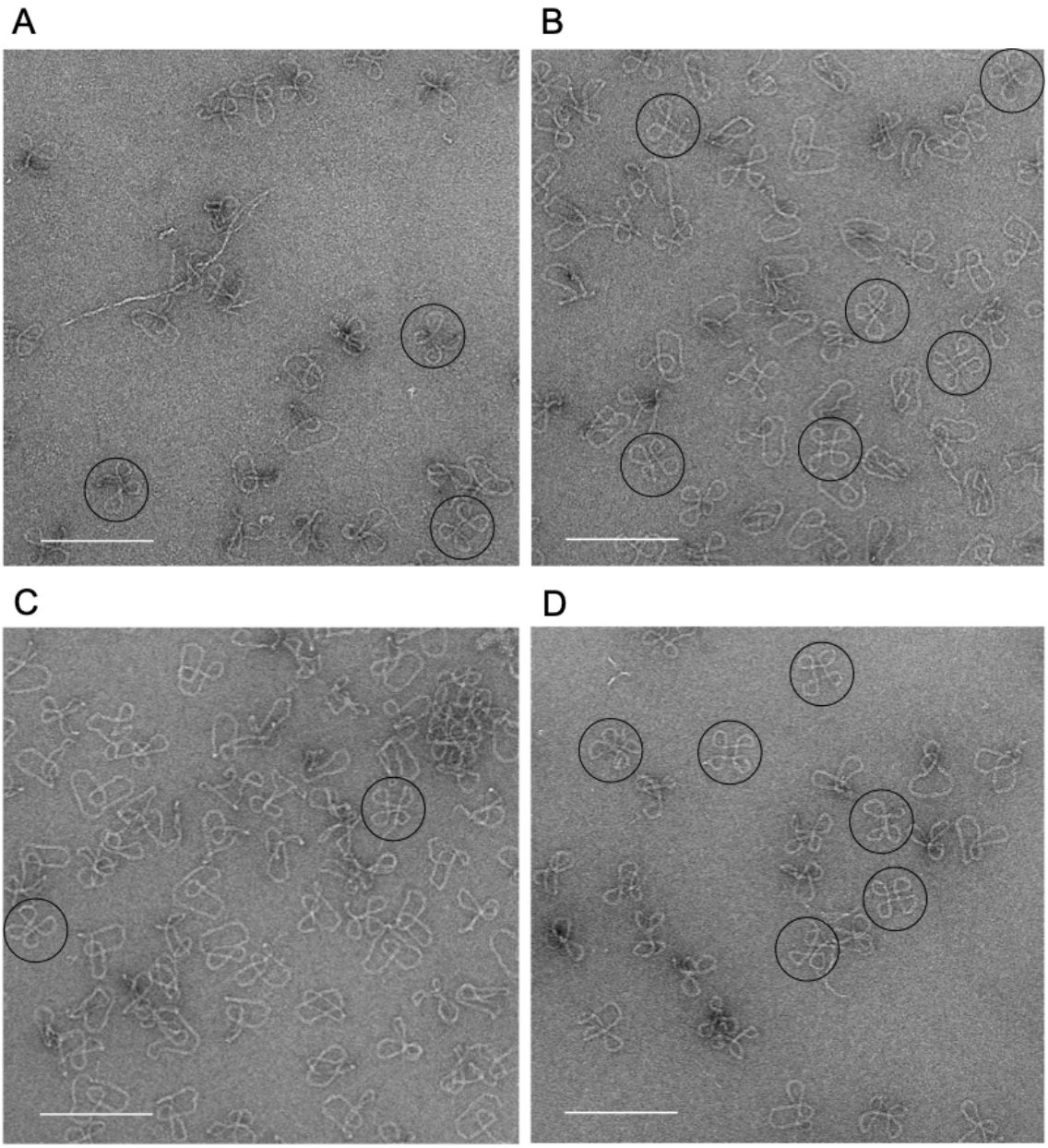


Figure S30: Transmission Electron Microscope (TEM) micrographs of purified ⌘-origami folded in the close state with only one junction out of four. A: ⌘-origami folded with the junction NE and without the junctions SE, NW, SW ; B: ⌘-origami folded with the junction SE and without the junctions NE, NW, SW ; C: ⌘-origami folded with the junction SW and without the junctions SE, NW, NE ; D: ⌘-origami folded with the junction NW and without the junctions SE, NE, SW. Particles folded in the full ⌘-origami are circled in black. Scale bar is 200 nm.

In the same way, we observed on agarose gel electrophoresis as well as with negative-stain transmission electron microscopy that the proportion of particles folded in the full ⌘-origami with the SE, SW and NE but not the NW junctions is less than when the origami is folded using any other triplet of junctions (figs. S26 and S31). These results together suggest that the NW junction staples stabilize the curved-shape better than the other junctions and is enough to stabilize the curvature in the full ⌘-shape.

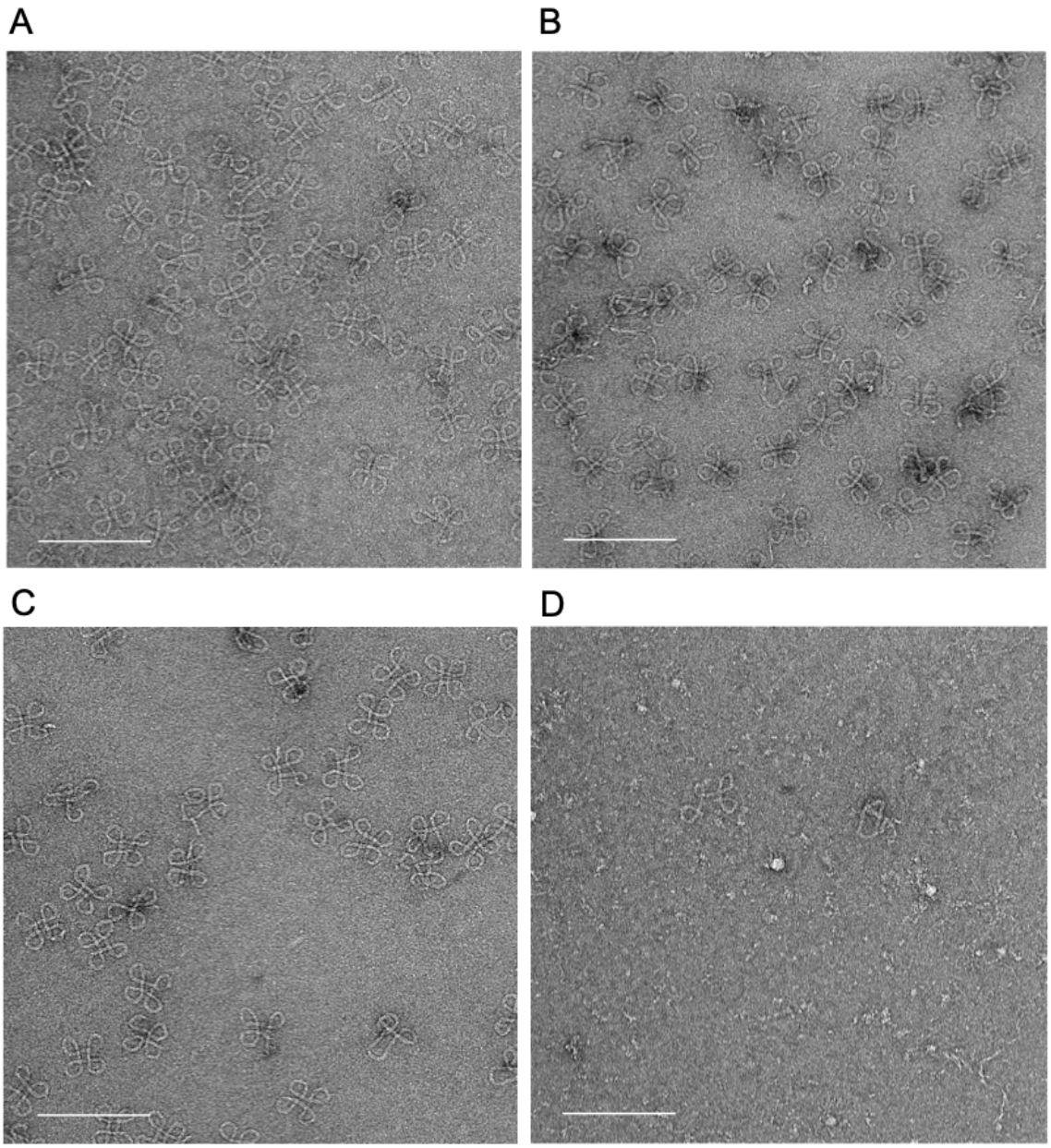


Figure S31: Transmission Electron Microscope (TEM) micrographs of purified ⌘-origami folded in the close state with three junctions out of four. A: ⌘-origami folded without the junction NE and with the junctions SE, NW, SW ; B: ⌘-origami folded without the junction SE and with the junctions NE, NW, SW ; C: ⌘-origami folded without the junction SW and with the junctions SE, NW, NE ; D: ⌘-origami folded without the junction NW and with the junctions SE, NE, SW. Scale bar is 200 nm.

Additionally, when trying to fold the ⌘-origami with only two junctions out of four, we observe that the ⌘-origami can reach its full ⌘-shape, with a better yield when using opposite junctions (e.g. NW and SE or NE and SW) rather than adjacent ones (e.g. NW and NE or NW and SW) (figs. S32 and S33). This can be logically explained by the fact that opposite junctions are in contact with the four sides while adjacent ones are only in contact with three.

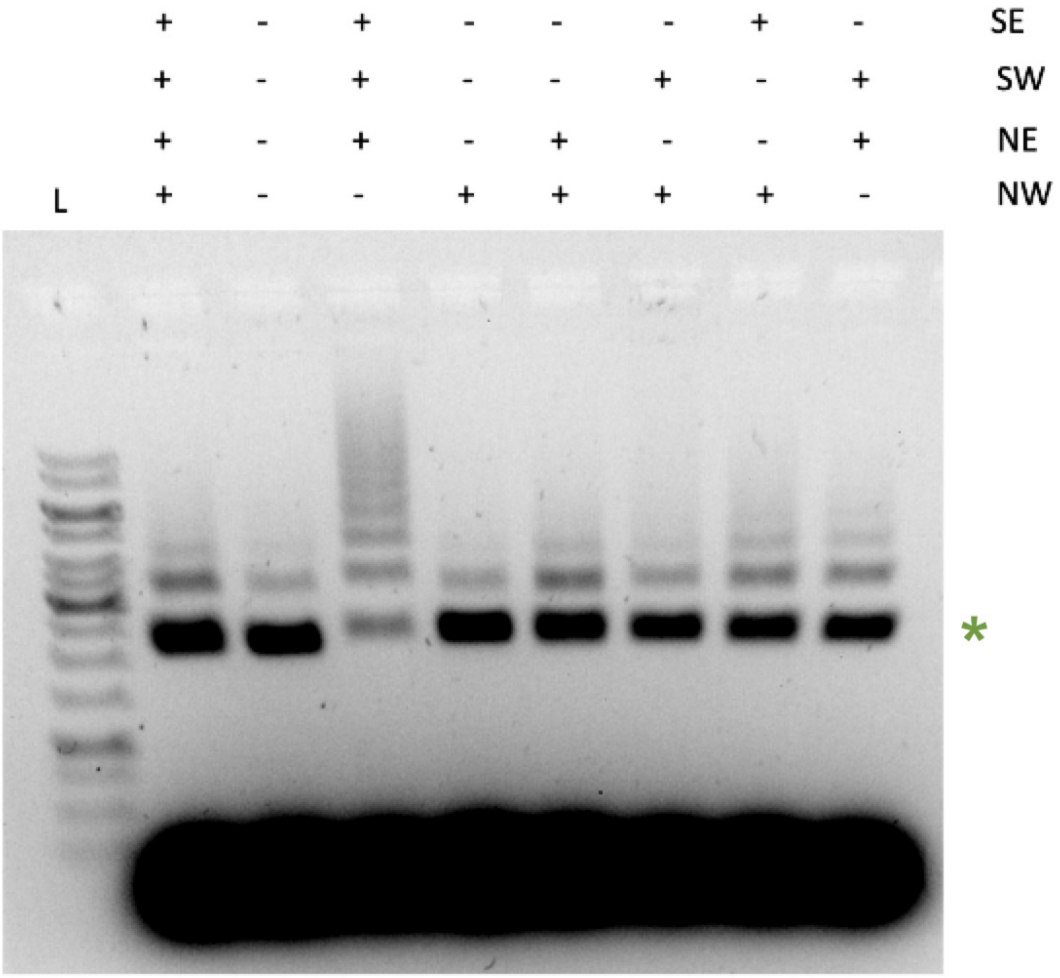


Figure S32: Gel analysis of the influence of the presence of junctions on the folding of the ⌘-origami. All the ⌘-origami were folded in the close state. The foldings were analyzed by agarose gel electrophoresis (1%). L: 1kb DNA ladder.

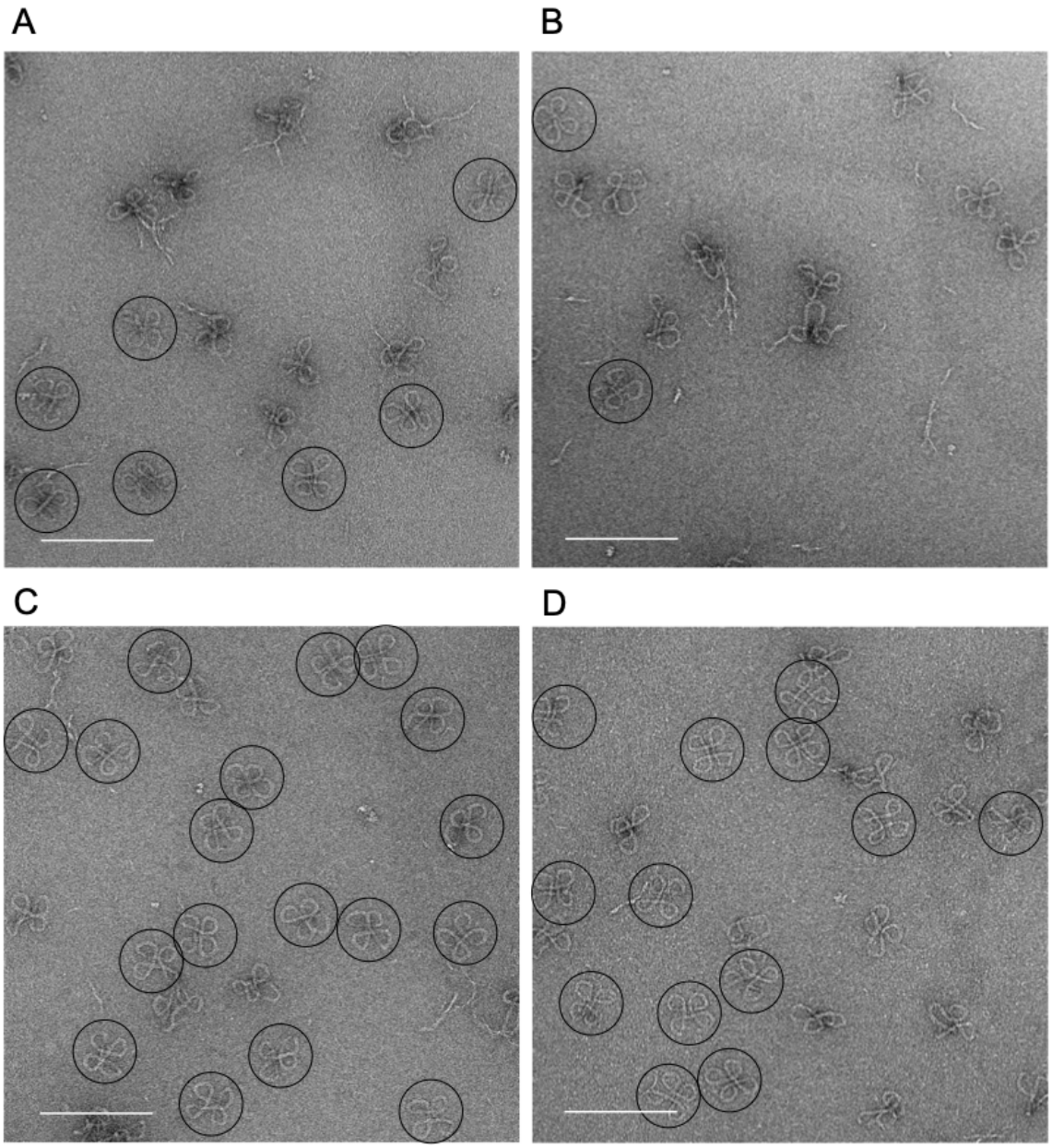


Figure S33: Transmission Electron Microscope (TEM) micrographs of purified ⌘-origami folded in the close state with two junctions out of four. A and B displays ⌘-origami with two adjacent junctions whereas C and D displays ⌘-origami with two opposite junctions. A: ⌘-origami folded with the junction NW and SW and without the junctions NE and SE ; B: ⌘-origami folded with the junction NW and NE and without the junctions SW and SE ; C: ⌘-origami folded with the junction NE and SW and without the junctions NW and SE ; D: ⌘-origami folded with the junction NW and SE and without the junctions NE and SW. Particles folded in the full ⌘-origami are circled in black. Scale bar is 200 nm.

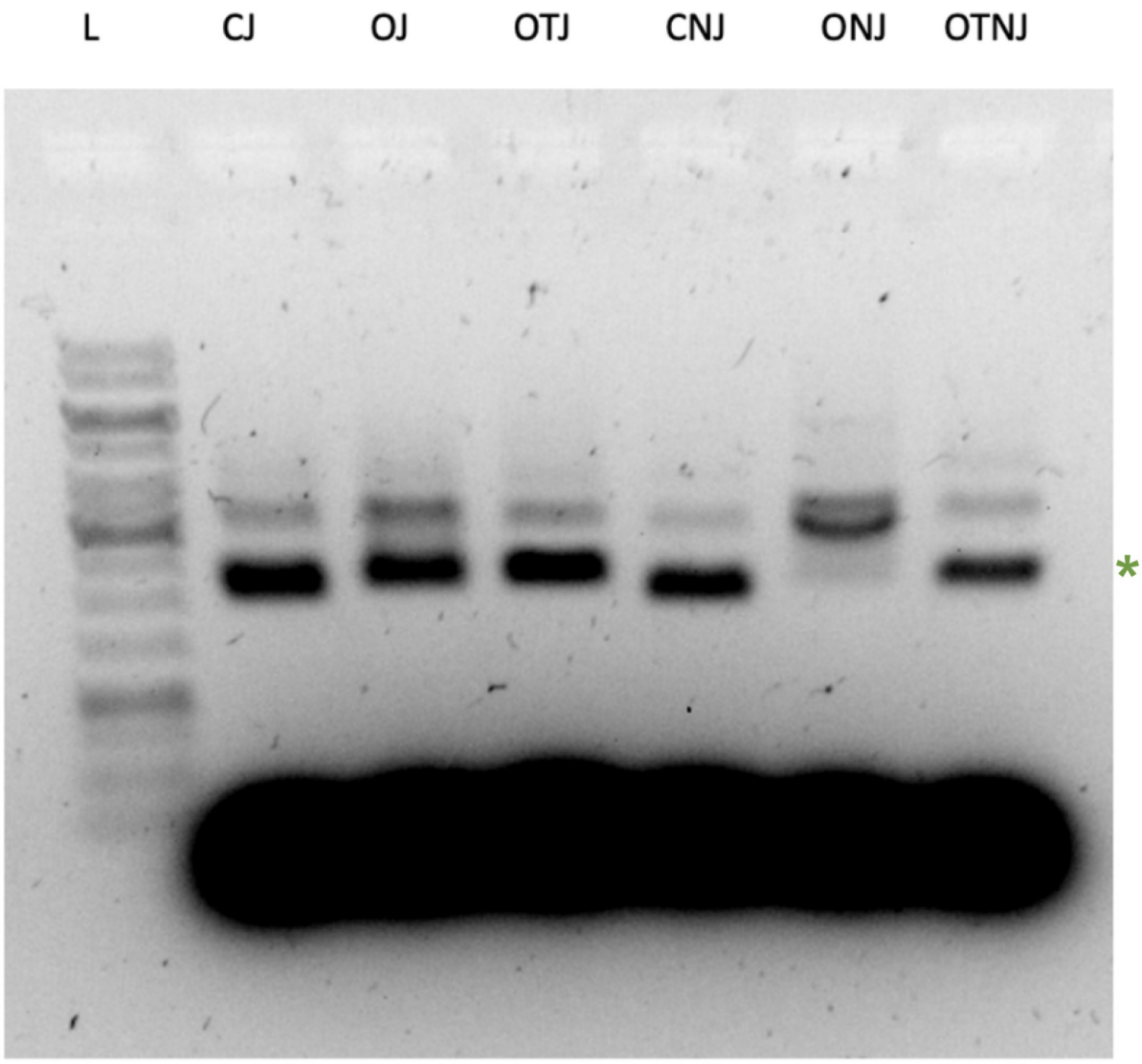


Figure S34: Gel analysis of the influence of the presence of junctions and open, open-T or close state on the folding quality of the ⌘-origami. The foldings were analyzed by agarose gel electrophoresis (1%). L: 1kb DNA ladder. CJ: ⌘-origami folded in the close state with the four junctions: NW, NE, SW, SE ; OJ: ⌘-origami folded in the open state with the four junctions: NW, NE, SW, SE ; OTJ: ⌘-origami folded in the open-T state with the four junctions: NW, NE, SW, SE ; CNJ: ⌘-origami folded in the close state without any of the four junctions: NW, NE, SW, SE ; ONJ: ⌘-origami folded in the open state without any of the four junctions: NW, NE, SW, SE ; OTNJ: ⌘-origami folded in the open-T state without any of the four junctions: NW, NE, SW, SE.

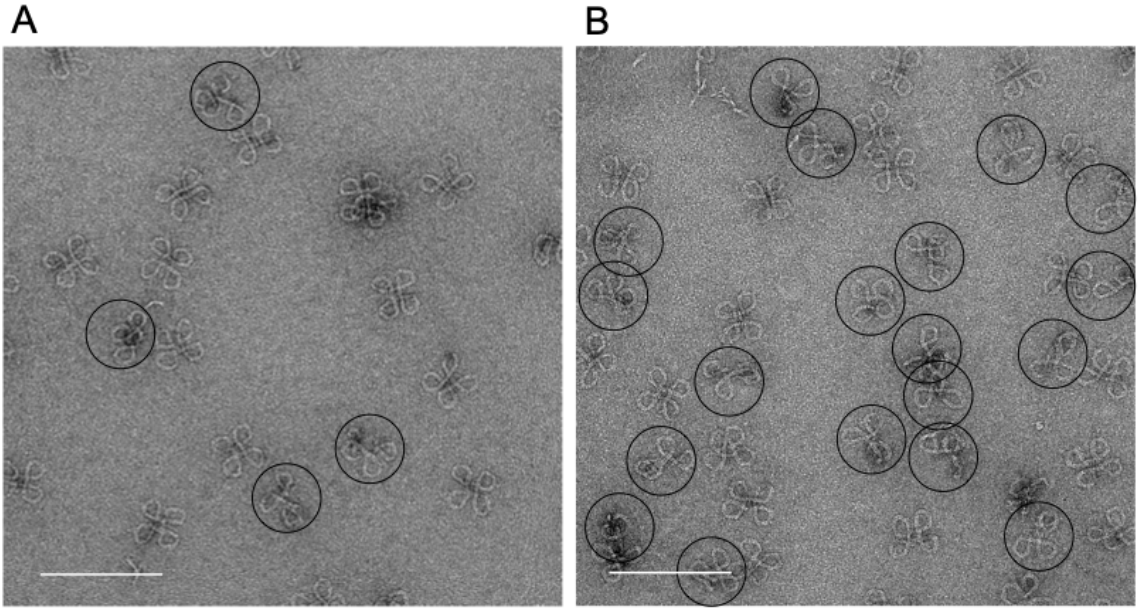


Figure S35: Transmission Electron Microscope (TEM) micrographs of purified ⌘-origami folded in different states with the four junctions NW, NE, SW and SE. A: ⌘-origami folded in the open state ; B: ⌘-origami folded in the open-T state. Particles not folded in the full ⌘-origami are circled in black. Scale bar is 200 nm.

# S3 Twisted revolution surfaces: model, parameters and helix routing algorithm, Figures S36 to S42

## S3.1 Initial helix spiraling route

Consider a continuously differentiable closed curve $S : u \in [0,1] \mapsto S(u)$ in the plane $(\mathbf{XZ})$. Let us denote by $\mathrm{rot}_\theta^U$ denotes the rotation of angle $\theta$ around the $\mathbf{U}$-axis. Consider a *twist* $\tau \in \mathbb{N}$. Let $S_\tau^R(t,u) = \mathrm{rot}_{2\pi t}^Z(R \cdot \mathbf{X} + \mathrm{rot}_{\pi\tau t}^Y(S(u))$ denotes the image of point $S(u)$ rotated by $\tau t$ half-turns around the $\mathbf{Y}$-axis, then translated by $R$ along the $\mathbf{X}$-axis and finally rotated by $t$ turn around the $\mathbf{Z}$-axis. The *$\tau$-twisted revolution surface* $S_\tau^R$ of $S$ with *revolution radius* $R$ is defined as the set of points, see fig. S36:

$$S_\tau^R = \{S_\tau^R(t,u) : t,u \in [0,1]\}$$

When $\tau = 0$, $S_0^R$ is simply the (untwisted) revolution surface with revolution radius $R$. When $\tau$ is even or when $\tau$ is odd and $S$ has a half-turn symmetry, $S_\tau^R$ is closed and continuously differentiable. The *section* $S_\tau^R(t)$ of the twisted revolution surface at $t$ turn (or, equivalently, at angle $2\pi t$) refers to the set:

$$S_\tau^R(t) = \{S_\tau^R(t,u) : u \in [0,1]\}$$

The designs considered in this paper correspond to:

- For the tori T1, ... T6: $S(u) = \big(2\cos(2\pi u), 0, \sin(2\pi u)\big)$ is the $(2,1)$-ellipse and $\tau$ ranges from 1 to 6;
- For the double-sphere DS: $S$ corresponds to the ☾ curve and $\tau = 0$;
- For the vault: $S$ corresponds to the profile of the vault protein and $\tau = 0$.

Let $P$ denotes the perimeter of $S$:

$$P = \int_u ||\dot{S}(u)||\, du, \text{ where } \dot{S}(u) = dS(u)/du$$

We denote by $s : \mathbb{R} \to \mathbb{R}$ the curvilinear abscissa of $S$:

$$s(x) = \int_{u=0}^{x} ||\dot{S}(u)||\, du, \text{ such that } P = s(1)$$

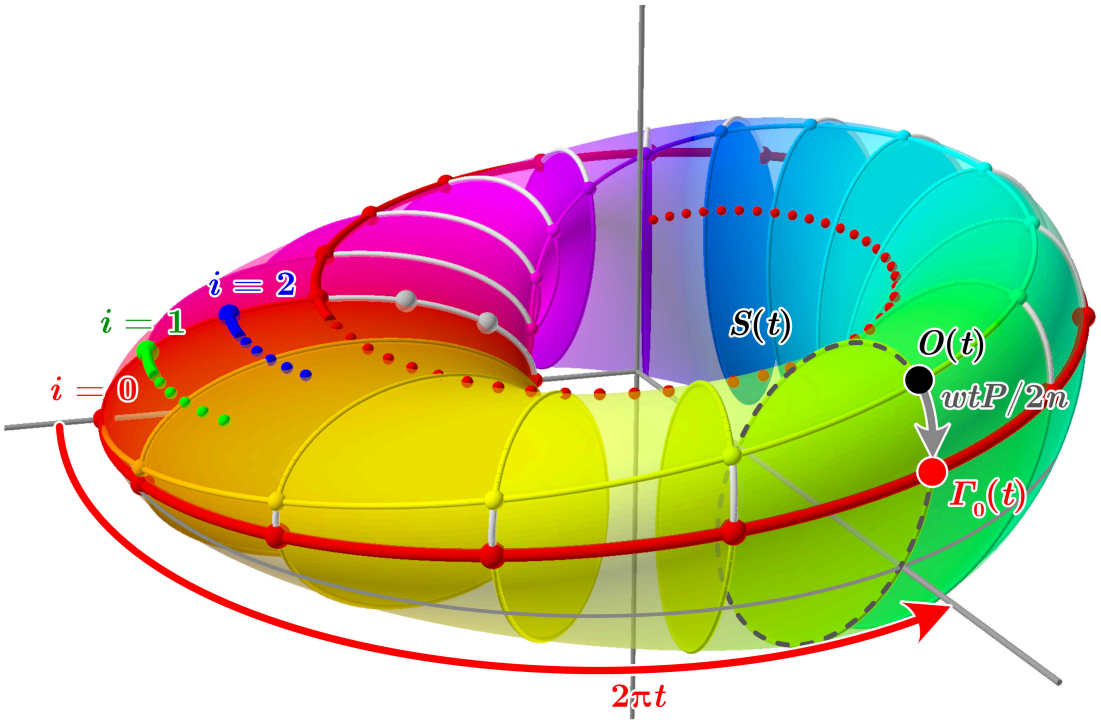


Figure S36: Initial helices routing.

and by $\sigma = s^{-1}$ its reciprocal, such that $\sigma(P) = 1$.

**The initial spiral helix routing** consists in routing $2n$ equally-spread helices per section according to a spiraling pattern. The number of helices is chosen to be even for allowing Given a revolution radius $R$, a *section scale* $\gamma > 0$, a *winding parameter* $w \in \mathbb{Z}$, the initial trajectories $(\Gamma_i)$ passing through $2n$ helices per section are defined:

$$\Gamma_i(t) = \gamma \cdot S_\tau^{(R/\gamma)}(t, \sigma((i + wt)P/2n)), \text{ for } t \in \mathbb{R} \text{ and } i = 0, 1, \dots$$

The principle is the following: on the initial section ($t = 0$ turn) the $2n$ helices are equally spread along the section, separated by $P/2n$ measured along the section (before $\gamma$-rescaling). Then the distance measured along the section between them is kept constant but their position within the current section is shifted linearly as they rotate around the revolution axis, so that when a full turn is completed ($t = 1$), they have moved by an integral number of $P/2n$ (namely $(i + w)$ times $P/2n$), so that they connect to one of the initial helix, resulting into a set of spirals covering the whole target surface. The way the helices are connected together depends on the winding parameter $w$. Precisely: when $\tau$ is even, Helix $i$ connects to Helix $(i + w) \bmod 2n$ after a full turn; whereas Helix $i$ connects to Helix $(i + n + w) \bmod 2n$ after a full turn when $\tau$ is odd. It follows that Spiral $i$ is the concatenation of all one-turn helix segment indexed in $(i + w\mathbb{Z}) \bmod 2n$ when $\tau$ is even, and by $(i + (n + w)\mathbb{Z}) \bmod 2n$ when $\tau$ is odd. If $k = \gcd(2n, w)$ when $\tau$ is even, and $k = \gcd(2n, n + w)$ when $\tau$ is odd,[1] then there are exactly $k$ spirals making each exactly $2n/k$ turns around the revolution axis. Note that if we want $k$ to be even, for instance to ensure the existence of a proper scaffold routing, then we need $w$ to be even if $\tau$ is even, and $w$ to have the same parity as $n$ if $\tau$ is odd.

The winding parameter not only influences the number of spirals and their number of turns around the revolution axis, but also the curvatures of the helices and their fit to the surface. This influence will be explored in the next section. Finally, one could think that the section scale $\gamma$ should be set to $2nH/P$ so that the inter-spiral distance $\gamma P/2n = H = 2.65\,\text{nm}$ equals the desired inter-DNA helix axis distance. However, as this inter-spiral distance is measured along the section, it does not reflect to the real distance between the neighboring spirals and it needs to be adjusted to the angle taken by the spirals against the sections, which in turns depends on $\gamma$ and $w$. This is why we need a special rescaling algorithm detailed in the following section S3.2.

[1] where $\gcd(a, b)$ denotes the greatest common divisor of integers $a$ and $b$.

## S3.2 Helix routing and scaling algorithm

As mentioned earlier, when the surface goes through abrupt changes of curvature, the helices hit the section with a tight angle and their distance along the section must be adjusted. This is for instance the case at the entrance of the tunnels in the double sphere designs or in the most twisted tori (T3 and above). As shown in fig. S38, the distance between consecutive helices measured along the sections must be increased when the helices hit the section with a tight angle. As a consequence, we need to scale up the sections accordingly. This in turn requires to adjust the revolution radius, until a proper set of parameter (section scale, revolution radius) is found so that the total helix length matches the target scaffold length. We have designed a special algorithm to solve this non-linear optimization system. Our algorithm relies on a coarse-grained finite element system mapped according to $m$ equally spaced sections, typically $m \sim 20-200$, see fig. S37. Each of the $k$ helices, each making $q = 2n/k$ turns, is broken into $qm$ segments joining as many masses sliding along the $m$ sections. Within each section, the masses are linked by springs whose empty lengths $(\ell^0_{ij})$ are adaptively adjusted so that the segments corresponding to the helices are equally spaced at distance $H$ (by default $H = 2.65\,\text{nm}$) from each other as explained next. In order to ensure that the helices stay as straight as possible, we add an angular spring around each mass so that the angle between its two adjacent helix segments ($\beta$ in fig. S37) is pushed toward $180°$.

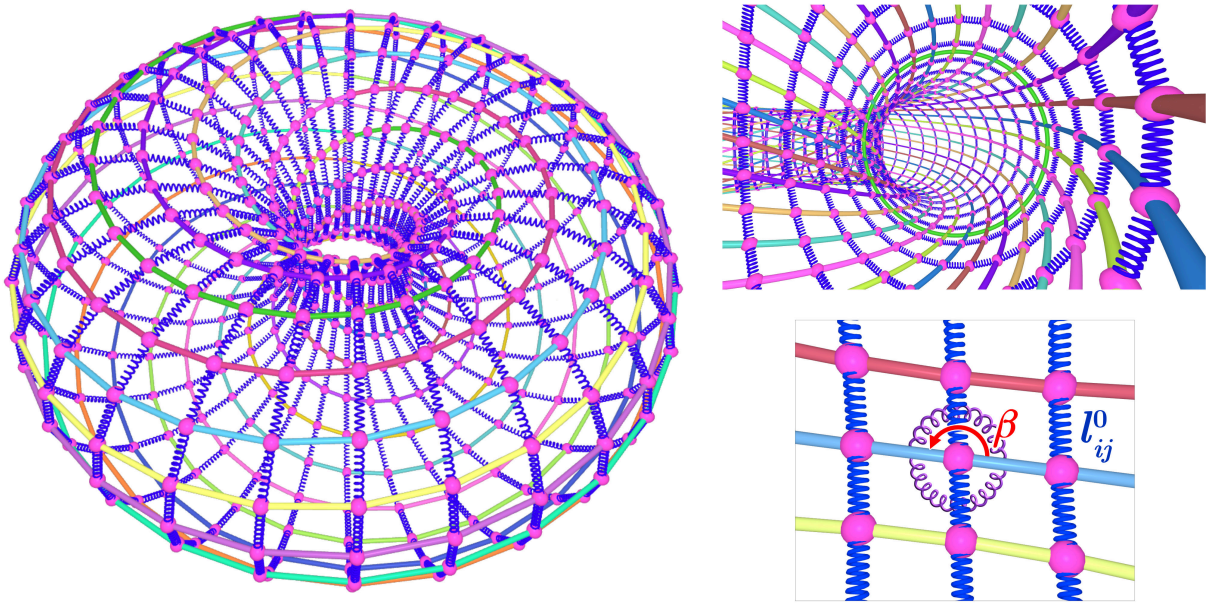


Figure S37: The coarse-grained finite element system used to optimize the helix trajectories.

**Our algorithm** proceeds as illustrated in fig. S38. It consists in two alternating phases: section scaling and revolution radius scaling, see fig. S38-C. During the section scaling, the revolution radius is fixed and the section are rescaled until the helices are $H$ appart from each other. In order to do so, we let the masses converge to an equilibrium while adaptively adjusting the empty lengths of the springs to take into account the current incident angles of both segments of helices with the section: using the notations in fig. S38-C2, we want the distance $d$ between two neighboring masses to verify that $d\cos\alpha_1 \approx H \approx d\cos\alpha_2$; at every step of the simulation, we thus adjust the empty length of each spring to $l^0_{ij} := (H/\cos\alpha_1 + H/\cos\alpha_2)/2$ and rescale the sections accordingly so that their perimeters are on average equal to the sum of the empty length of their springs. When the equilibrium is reached, we turn to the revolution radius phase: as illustrated in fig. S38-C2, the algorithm uses Chebyshev interpolation to compute a continuous trajectory for each of the $k$ helices, compute their lengths in base pairs (rounding to the nearest integer) If the total length equals to the target scaffold length, the process ends. Otherwise the revolution radius is adjusted (reduced if the total length is higher, increased otherwise) and the algorithm goes back to the section rescaling phase.

As the process may not converge to the exact length of the scaffold, the user may interrupt the process at any time and the algorithm enforce the total length to the length of the scaffold by tuning *a minima*

the rise of the $k$ helices. This is useful without any harm when the process bounces between two integers surrounding the target value (e.g. between $7248$ and $7250$ when the target length is $7249$).

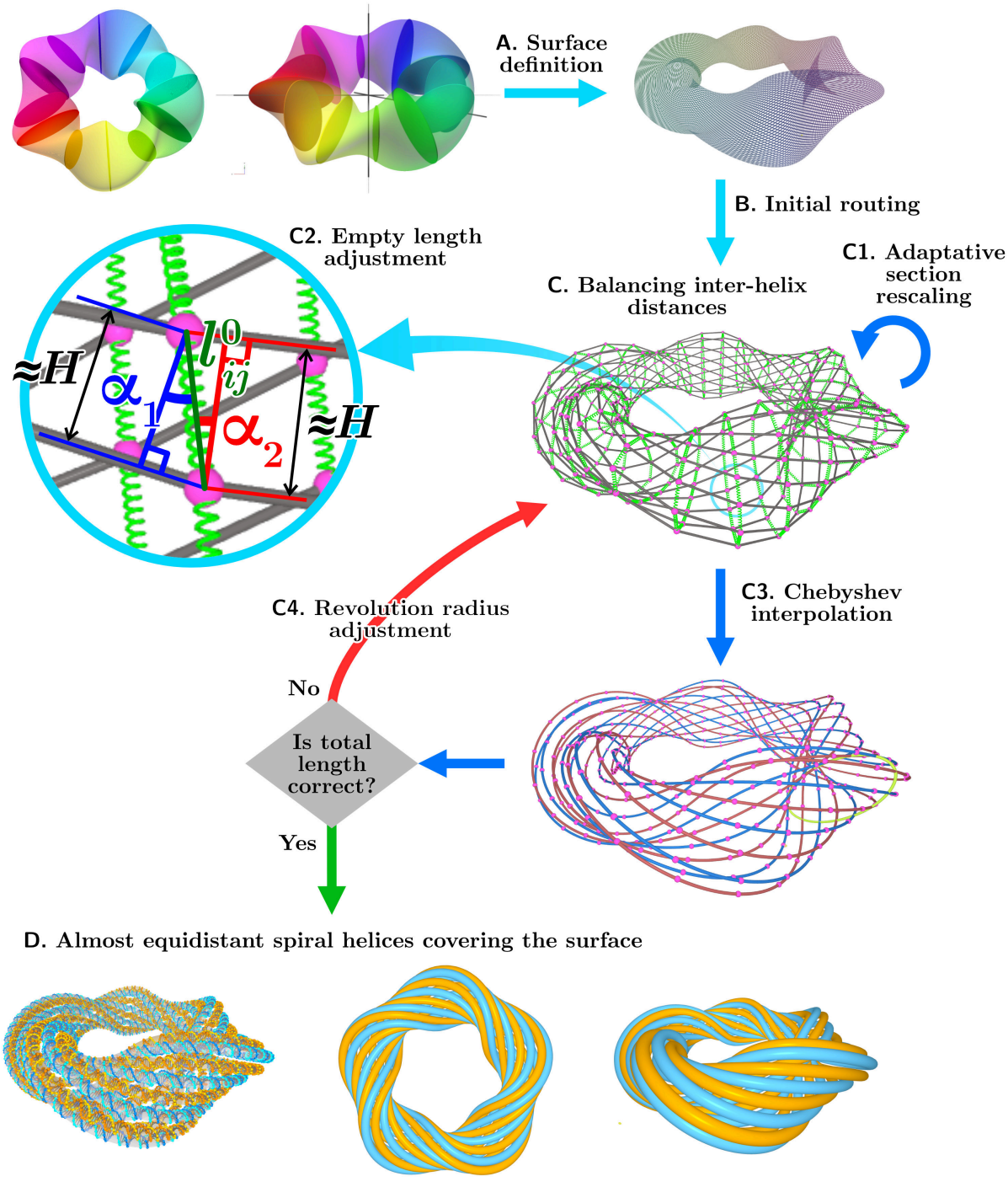


Figure S38: Helix routing and scaling algorithm

## S3.3 The winding parameter

The winding parameter controls the coiling and super-coiling of the spirals. Indeed, when Helix $i$ completes a full turn, it completes $\tau/2 + w/2n$ turns (super-coils) around the section axis. As shown in fig. S39, adjusting this parameter allows to select a set of initial trajectories that fits the surface while minimizes their torsion and curvature, and thus hopefully maximizing their foldability. ENSnano allows to tune this parameter to find the best winding parameter suited for your target surface.

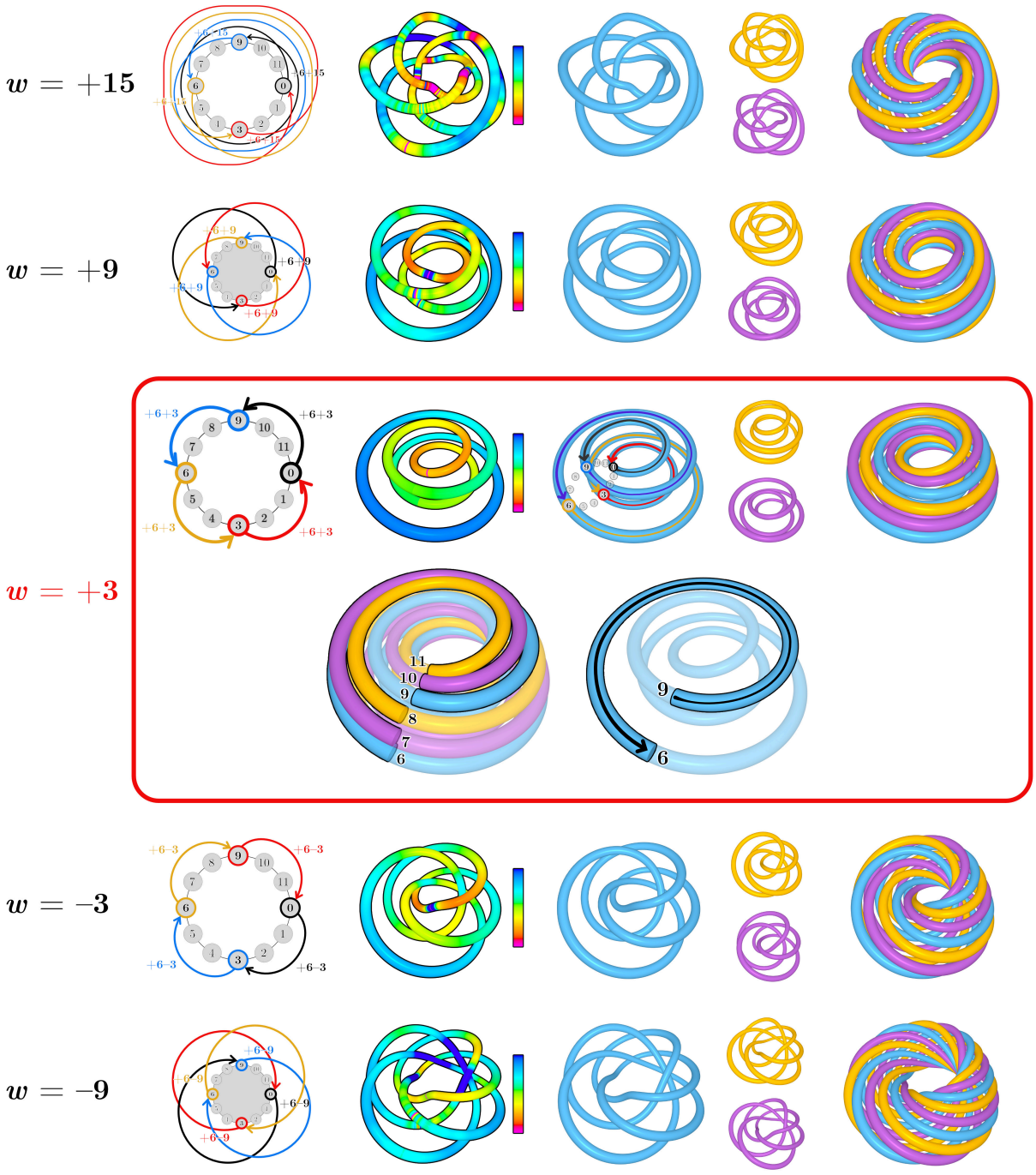


Figure S39: Influence of the winding parameter on the coiling, supercoiling and curvature of the helix spiraling trajectories in a virtual design with $12 = 2n$ helices per section. Setting $w = +3$ produces the smoothest trajectories. Curvature color ranges from 5 nm to 20 nm.

## S3.4 Torsion of the resulting helices as a function of the winding parameter

Figure S40 shows the average absolute value of the torsion measured along the resulting helix trajectories for the designs DS, and T1 to T6 for different values of the winding parameters (the closest possible around the chosen value for our designs). Observe that the winding parameter chosen for the origami design (marked with a red star) is the one minimizing the torsion along the helices. Observe as well that the torsion increases in designs T1 to T6 allowing to challenge our design paradigm with increasing curvature and torsion complexities.

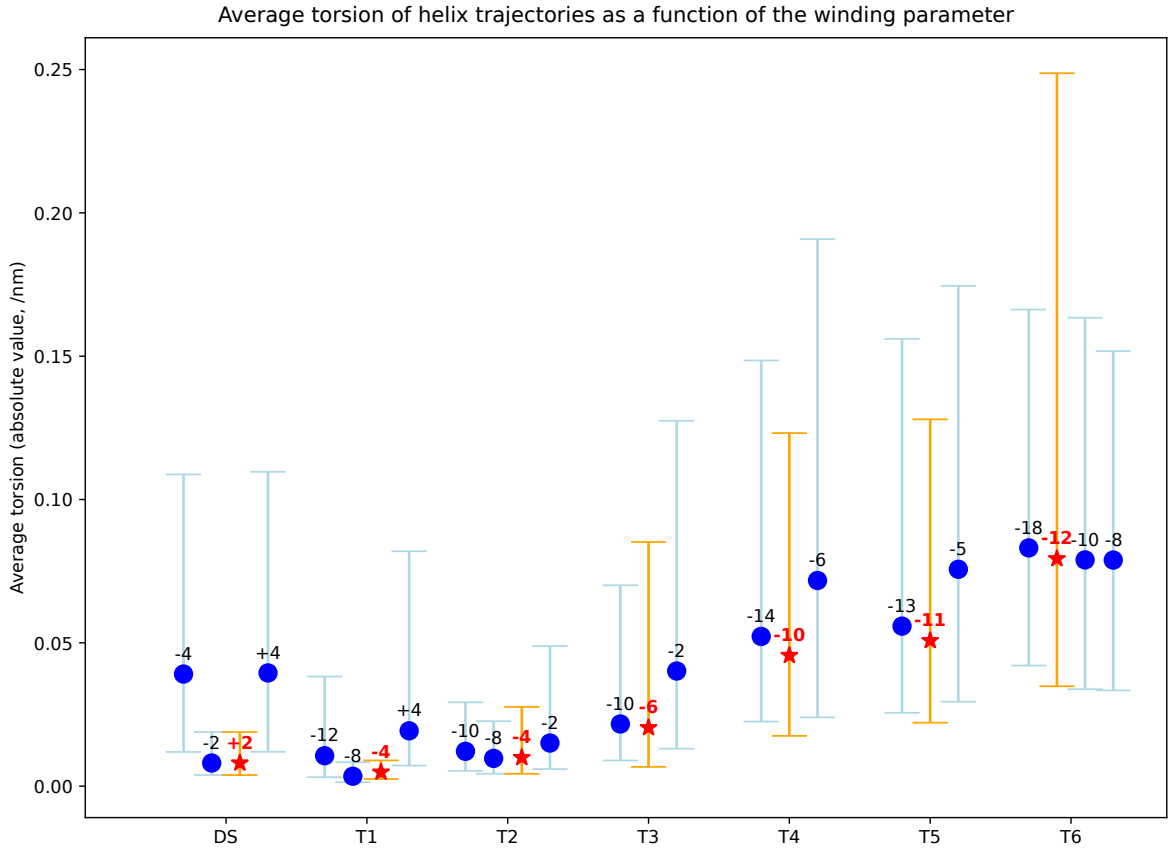


Figure S40: Average absolute torsion measured in $\mathrm{nm}^{-1}$ along the different helix trajectories as a function of the winding parameter $w$ for the designs DS, and T1 to T6. The value of the winding parameter is indicated on top of each point. The chosen winding parameter is indicated by a red star for each design.

## S3.5 Impact on the helix trajectory torsion of the helix routing and scaling algorithm

Figure S41 shows the evolution of the average absolute torsion (in $nm^{-1}$) of the helices trajectories computed during the execution of the helix routing and scaling algorithm (fig. S38). We observe that the angular springs (fig. S37) allow to reduce significantly the torsion of the helix trajectories during the first steps of the algorithm during which the inter-helix distances are balanced. The torsion then stabilizes while the algorithm finely tunes the shape scale to match the target scaffold length in the remaining steps.

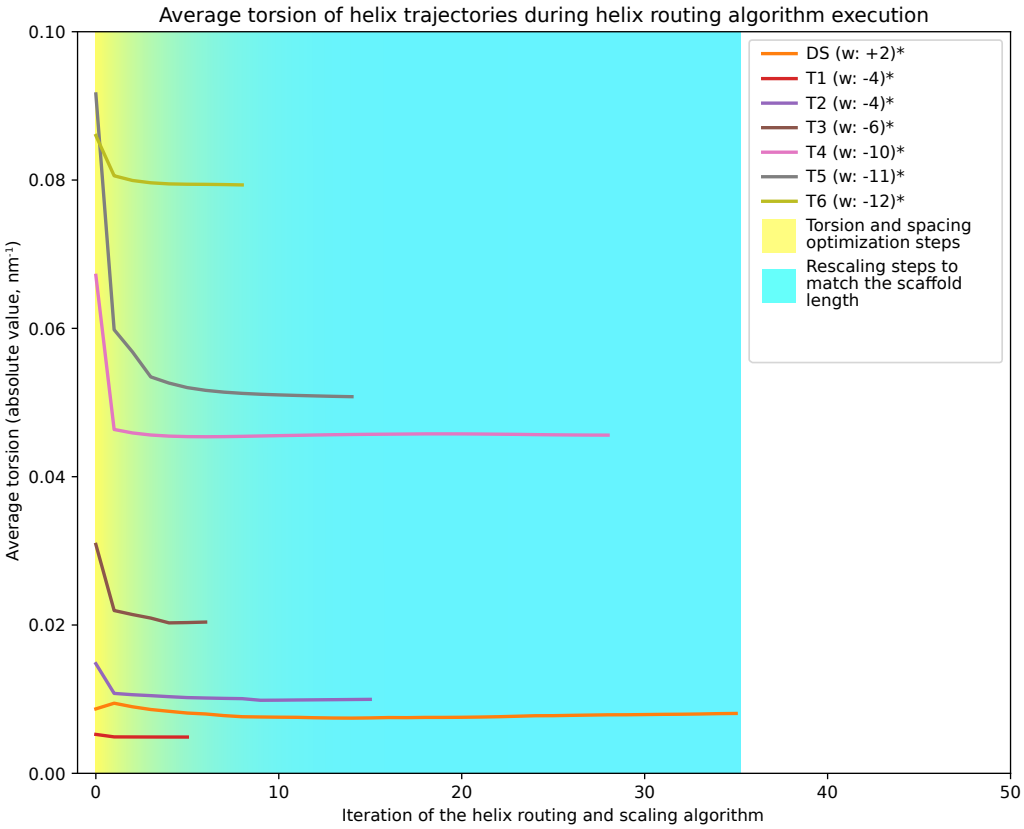


Figure S41: Evolution of the average torsion along the helices during the execution of the helix routing and scaling algorithm (fig. S38) for the designs DS and T1 to T6 with the chosen winding parameters. For every design, the torsion drops during the first stages of the algorithm during which the inter-helix distance are balanced and the trajectories are "rectified" and then the torsion remains quasi-constant during the second phase of the algorithm where the shape scale is finely tuned to reach the target scaffold length.

## S3.6 Torsion of the helix trajectories for all designs

Figure S42 shows the absolute value of the torsion measured along each helix trajectory for all the designs. Observe that the torsion in the vault and double-sphere DS reaches its peak in the tunnels where the helices sustain the highest slope change. Observe that the torsion increases significantly from T1 to T6, demonstrating that DNA helices sustains more and more strain from T1 to T6 (mostly in the inner circle).

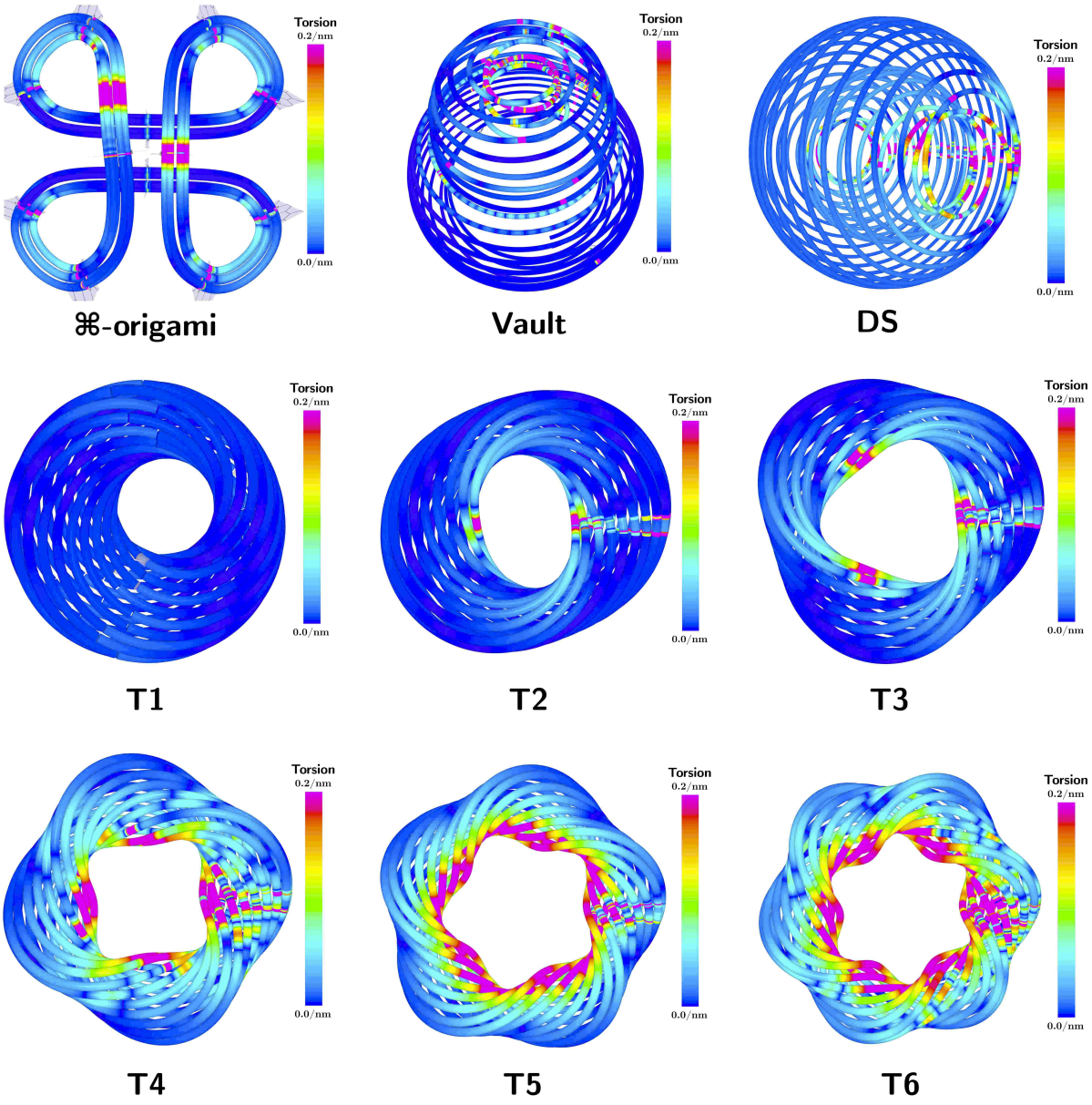


Figure S42: Absolute value of the torsion along each helix trajectory for all designs. Scale bar are uniform and range from $0.0\,\mathrm{nm}^{-1}$ (blue) to $0.2\,\mathrm{nm}^{-1}$ (purple).

# S4 Experimental validation of spiral-based design for hollow shaped toroidal surfaces, Figures S43 to S92

## S4.1 Tori designs

### S4.1.1 Torus I design

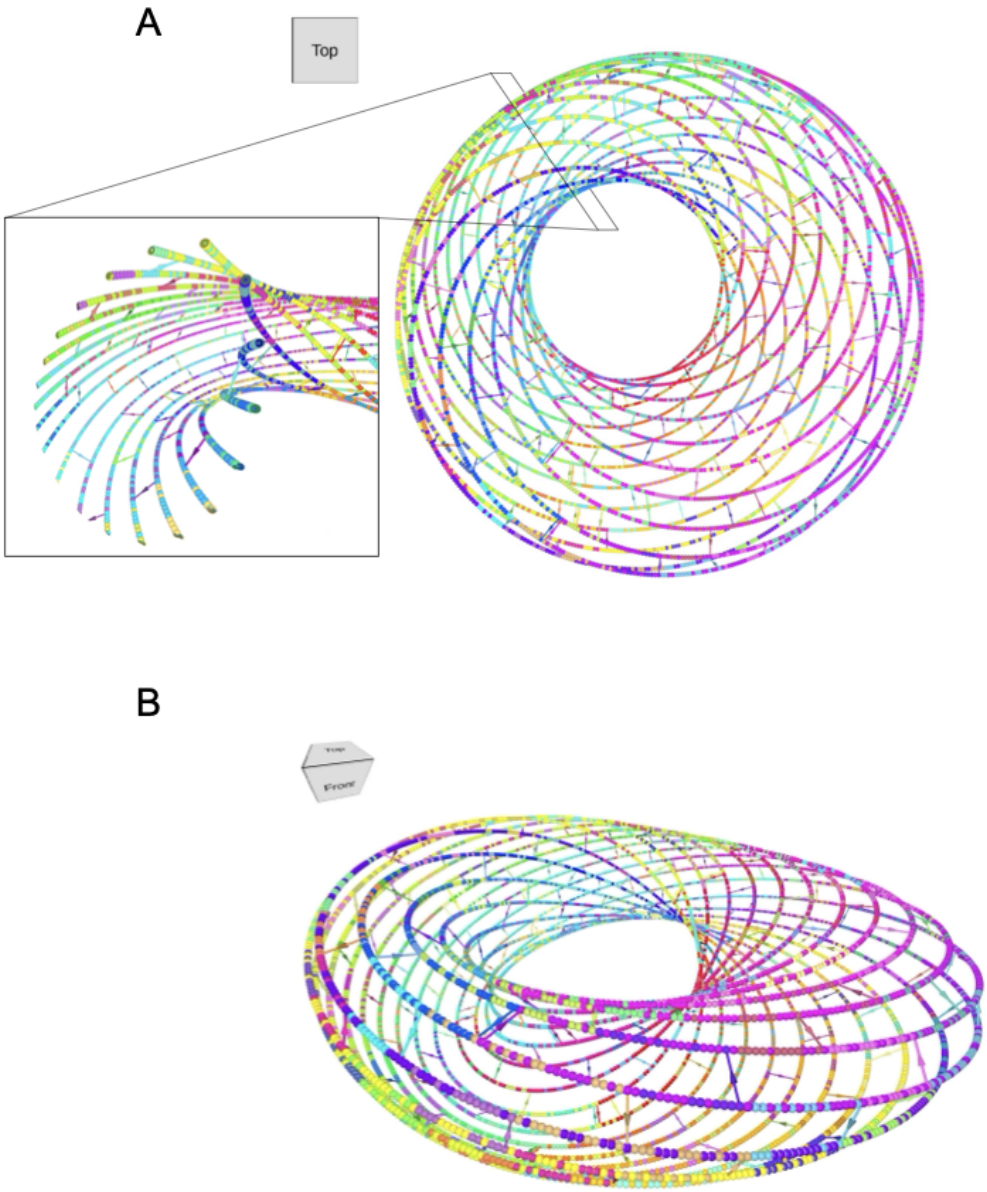


Figure S43: 3D view of the T1 design, line representation. A: Top view and cross-section; B: side view. Each line represents a double helix of DNA. Transversal bars represent crossovers.

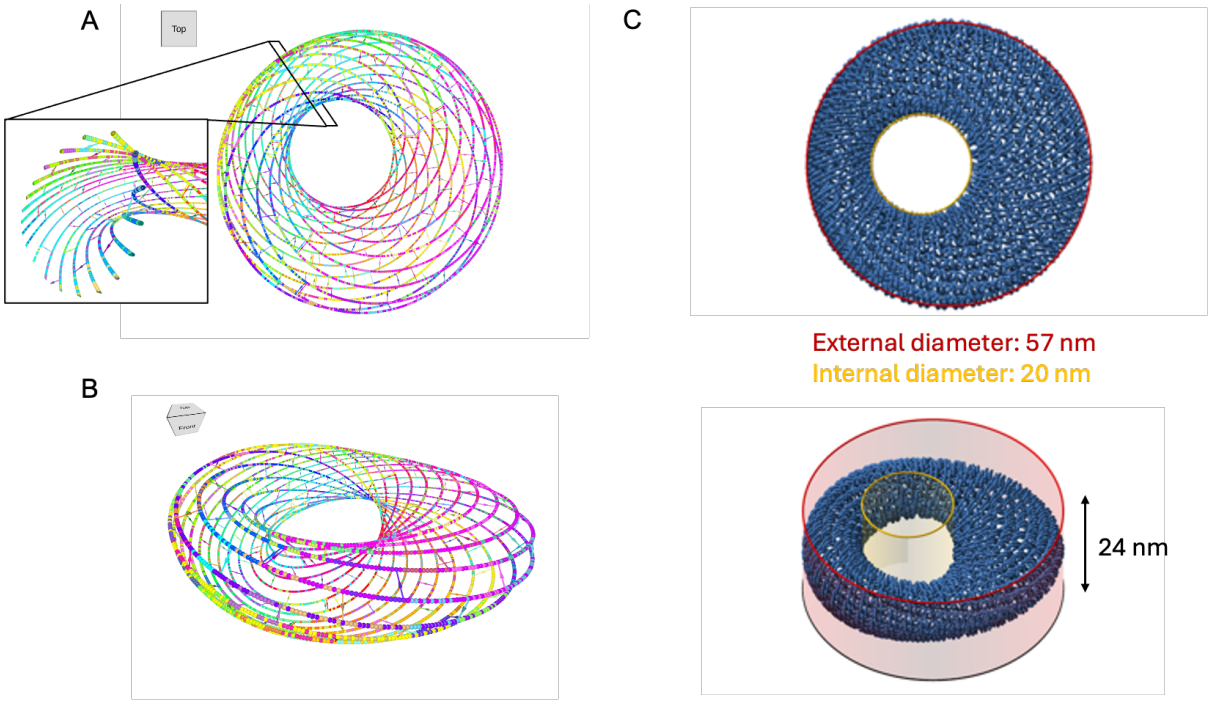


Figure S44: 3D view of the T1 design, helix representation. A: Top view and cross-section; B: side view. Each ball represents a deoxynucleotide; C: Dimensions of the T1 origami. Top view (up), side view (bottom). External diameter of 57 nm (red circle), internal diameter of 20 nm (yellow circle), height of 24 nm.

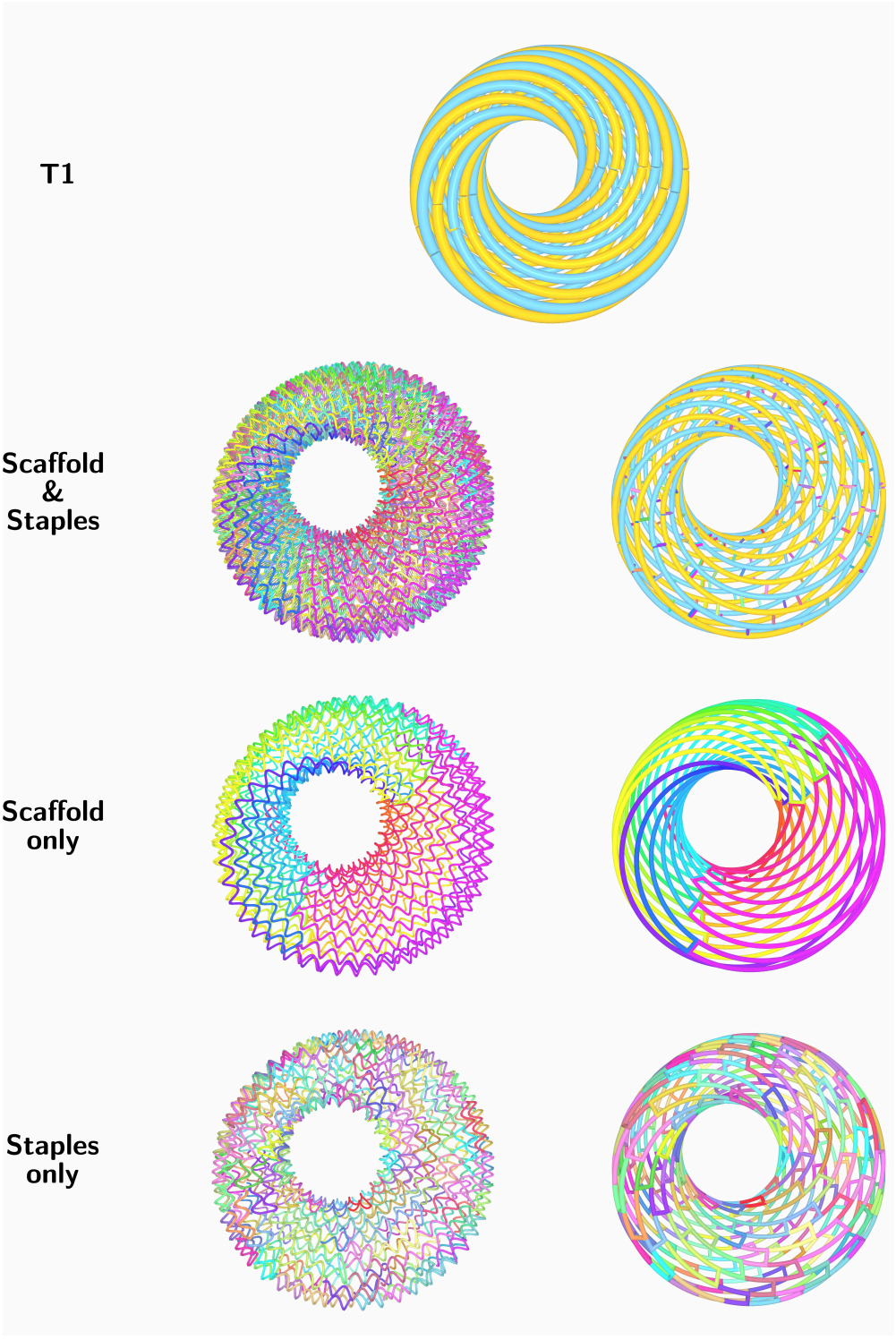


Figure S45: 3D view of the T1 design, helix (left) and line (right) representations. Views of the two spirals (top), the scaffold and staples (middle up), the scaffold (middle down) and the staples (bottom). Transversal bars on the line representation represents a crossover.

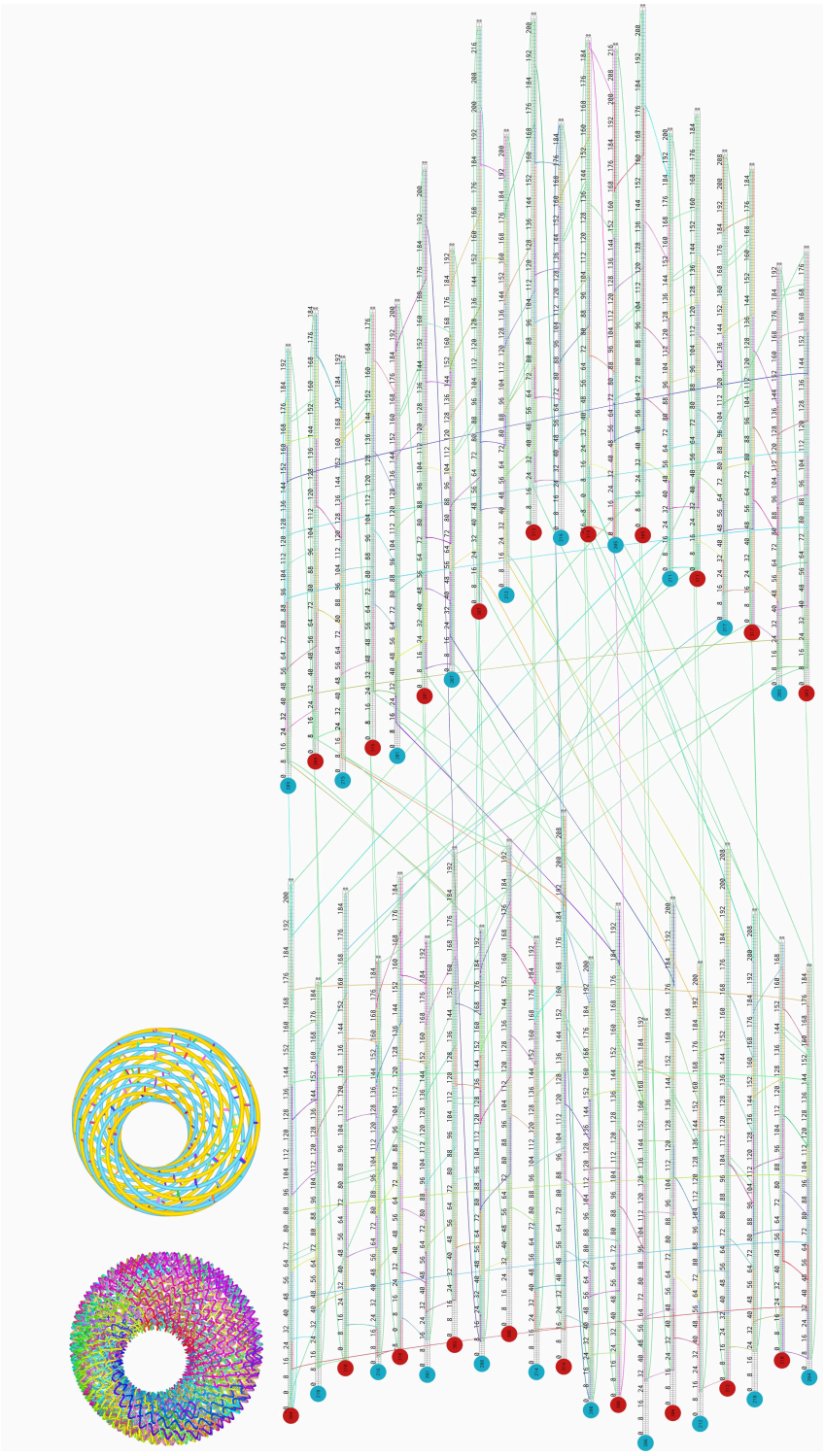

Figure S46: 2D view of the T1 design. Scaffold and staples.

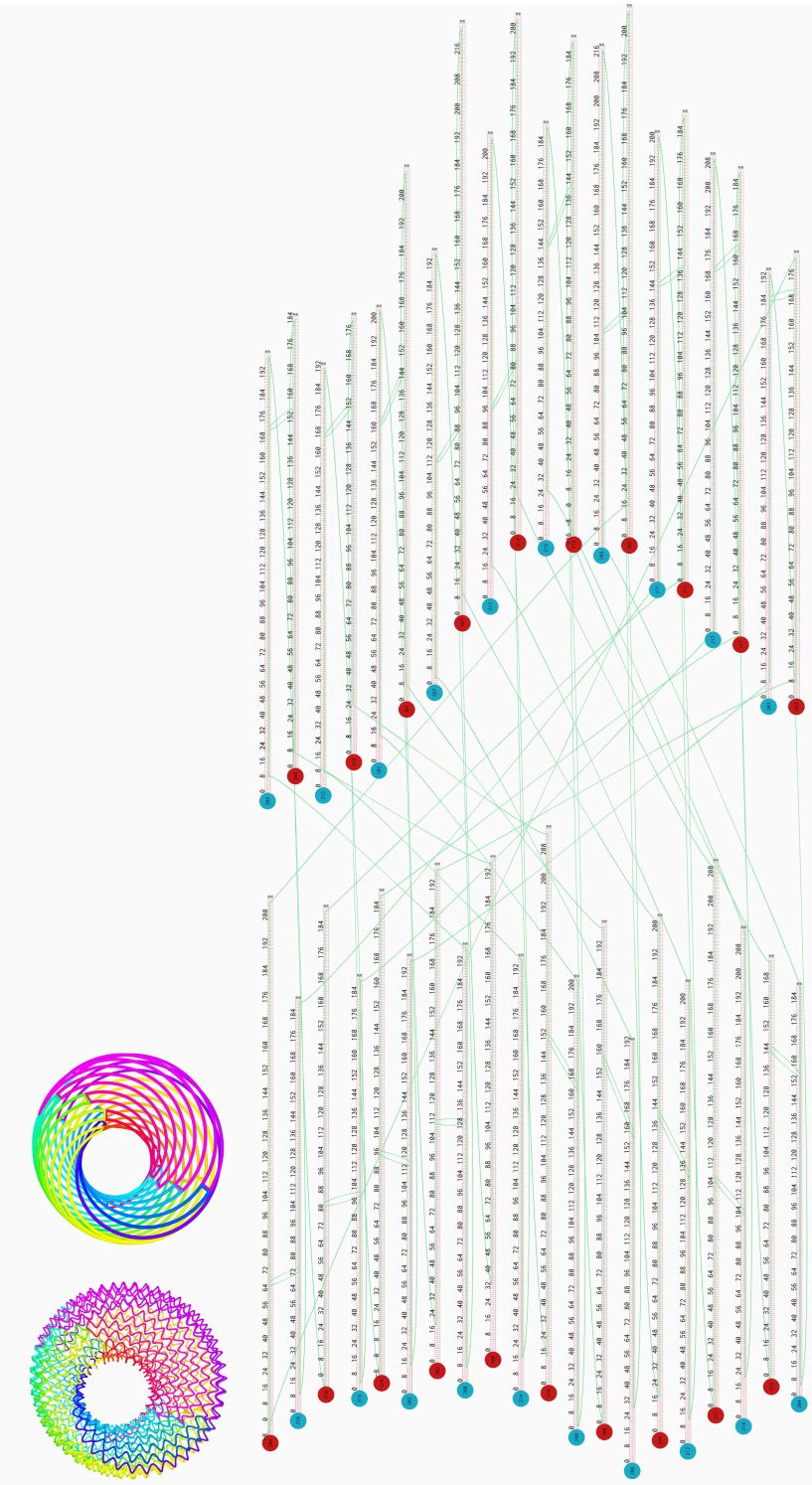

Figure S47: 2D view of the T1 design. Scaffold only.

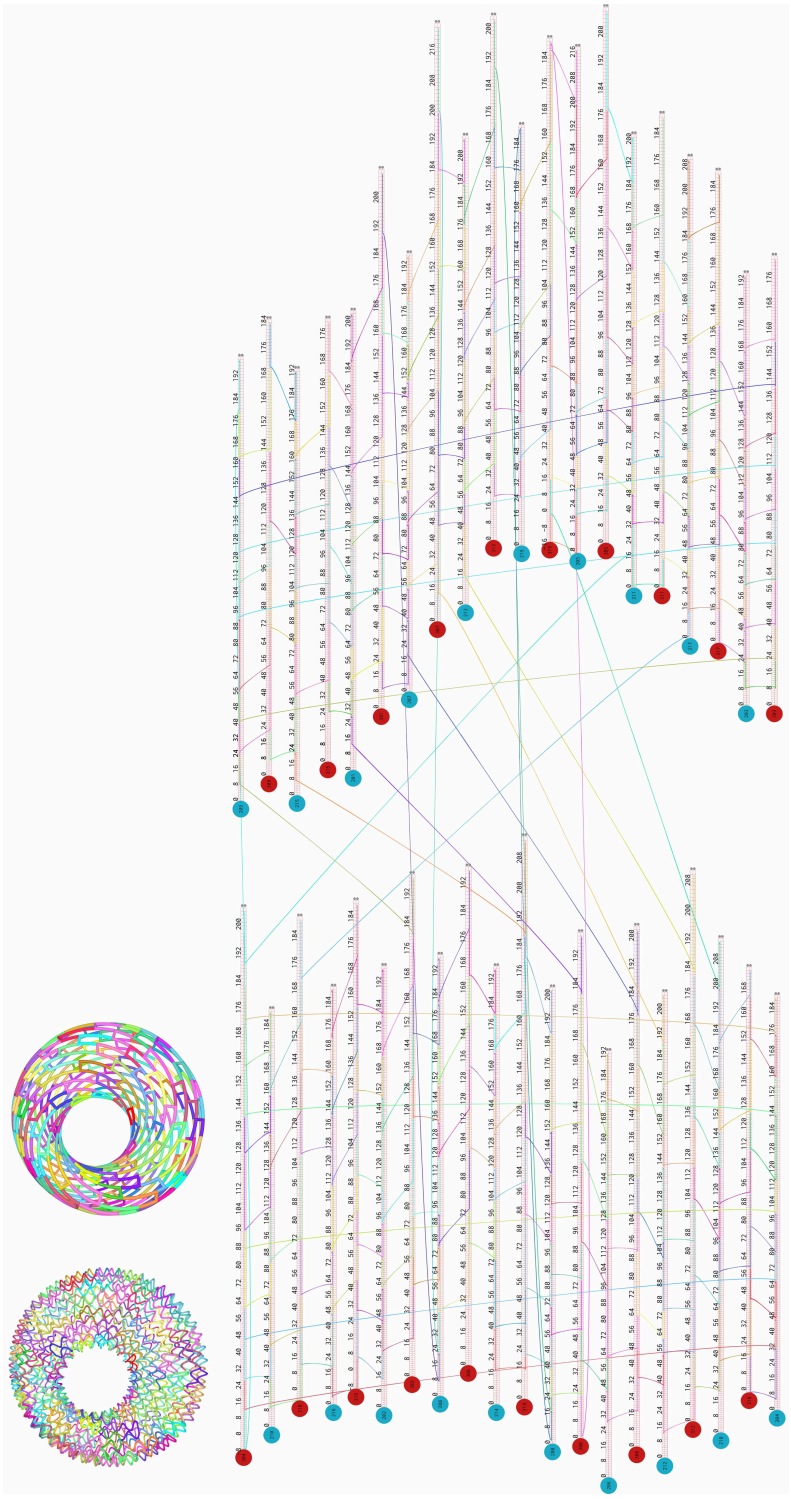

Figure S48: 2D view of the T1 design. Staples only.

### S4.1.2 Torus 2 design

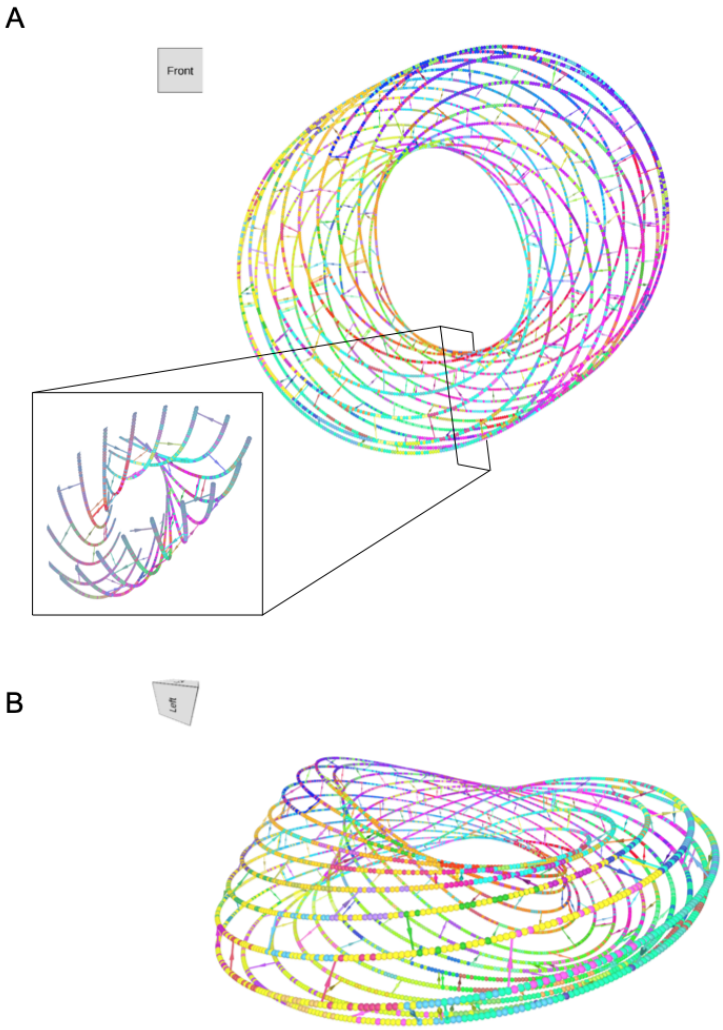


Figure S49: 3D view of the Torus 2 design, line representation. A: Front view and cross-section; B: side view. Each line represents a double helix of DNA. Transversal bars represent crossovers.

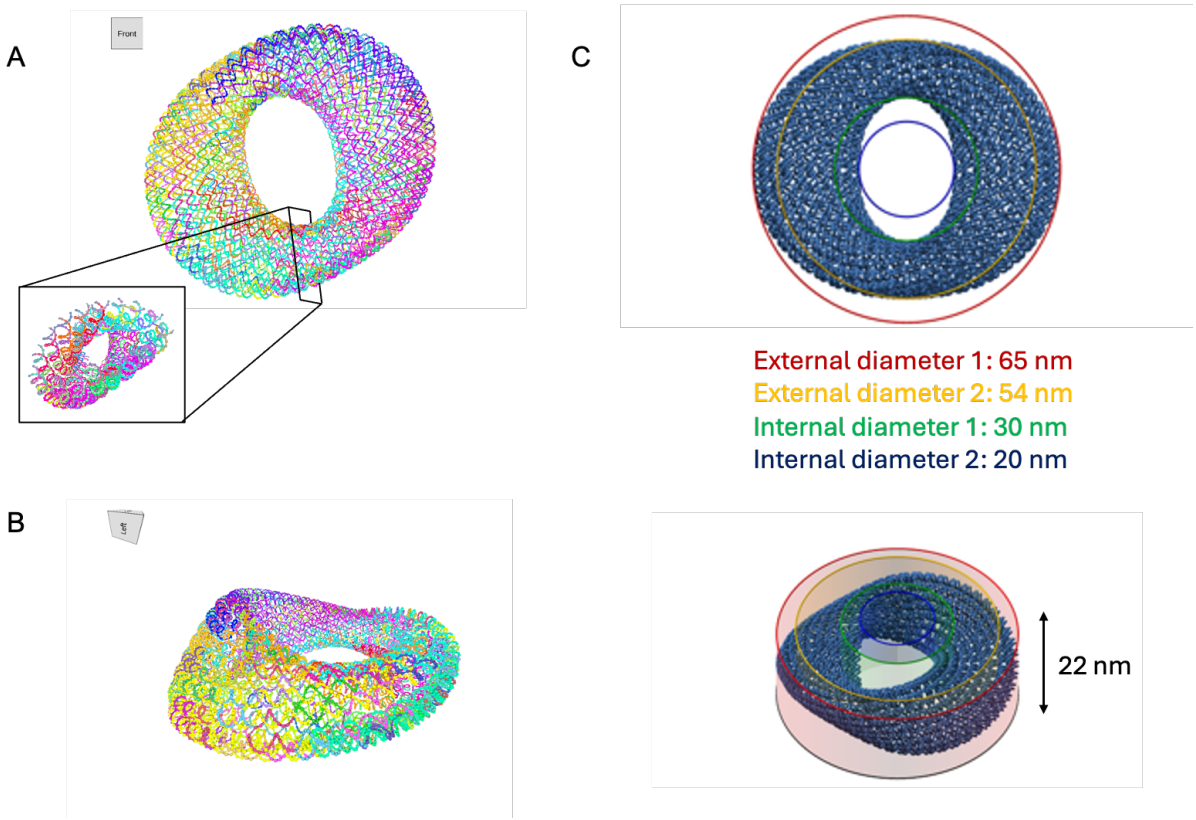


Figure S50: 3D view of the Torus 2 design, helix representation. A: Front view and cross-section; B: side view. Each ball represents a deoxynucleotide; C: Dimensions of the T2 origami. Front view (up), side view (bottom). External diameter 1 of 65 nm (red circle), external diameter 2 of 54 nm (yellow circle), internal diameter 1 of 30 nm (green circle), internal diameter 2 of 20 nm (blue circle), height of 22 nm.

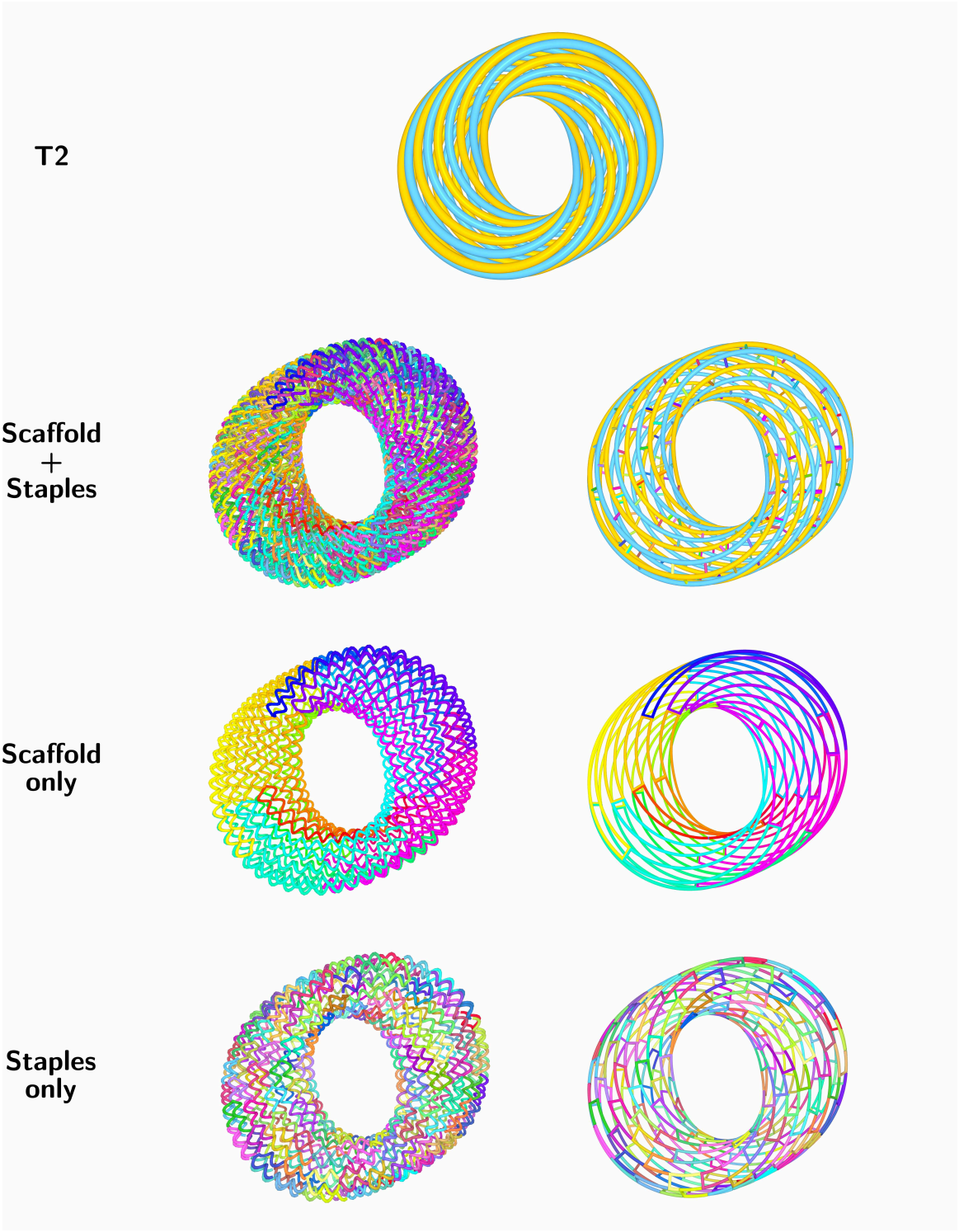


Figure S51: 3D view of the T2 design, helix (left) and line (right) representations. Views of the two spirals (top), the scaffold and staples together (middle up), the scaffold (middle down) and the staples (bottom). Transversal bars on the line representation represents a crossover.

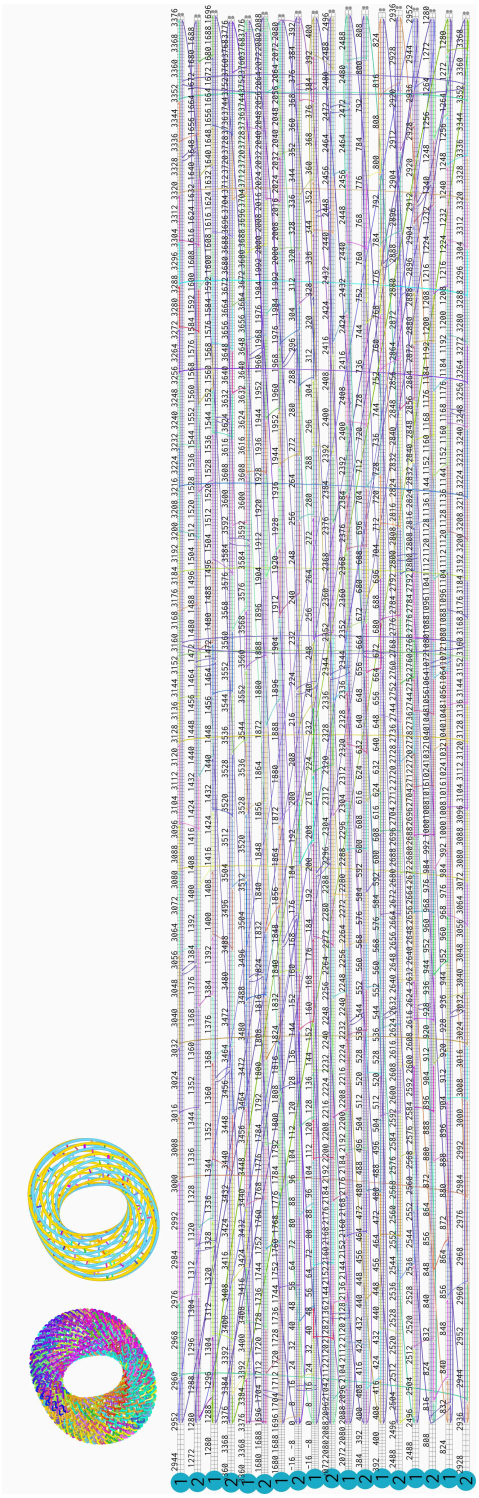

Figure S52: 2D view of the Torus 2 design. Scaffold and staples.

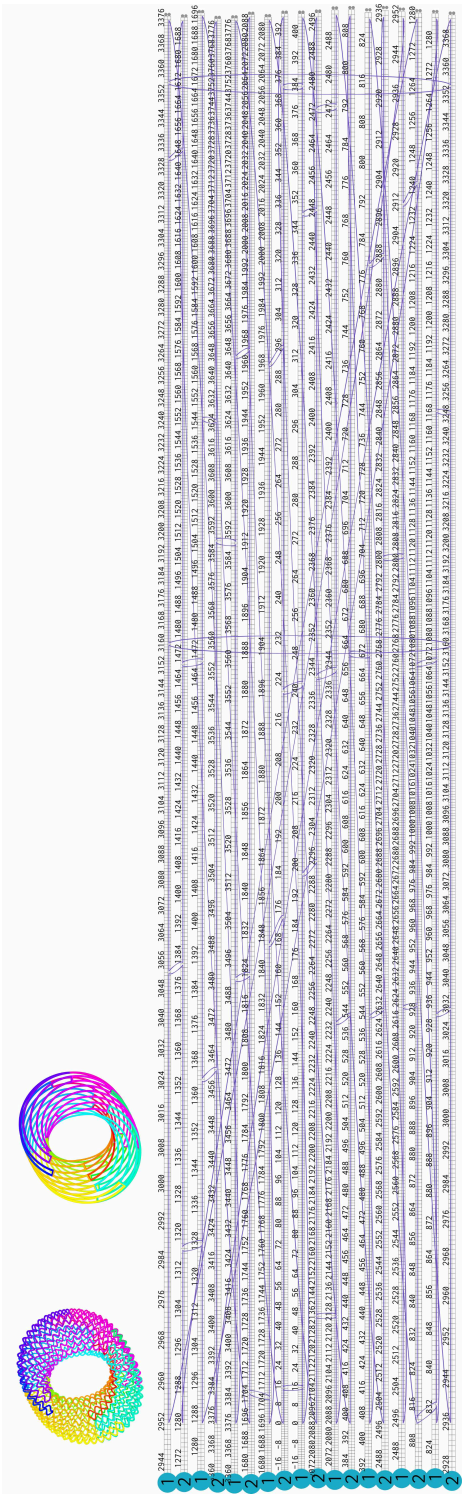

Figure S53: 2D view of the Torus 2 design. Scaffold only.

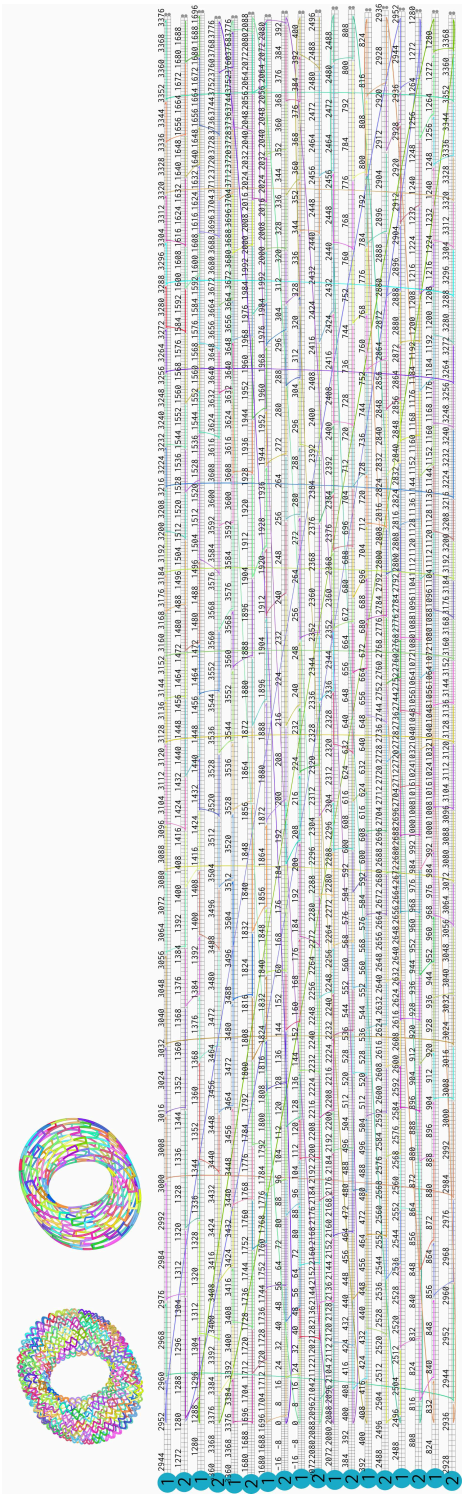

Figure S54: 2D view of the Torus 2 design. Staples only.

### S4.1.3 Torus 3 design

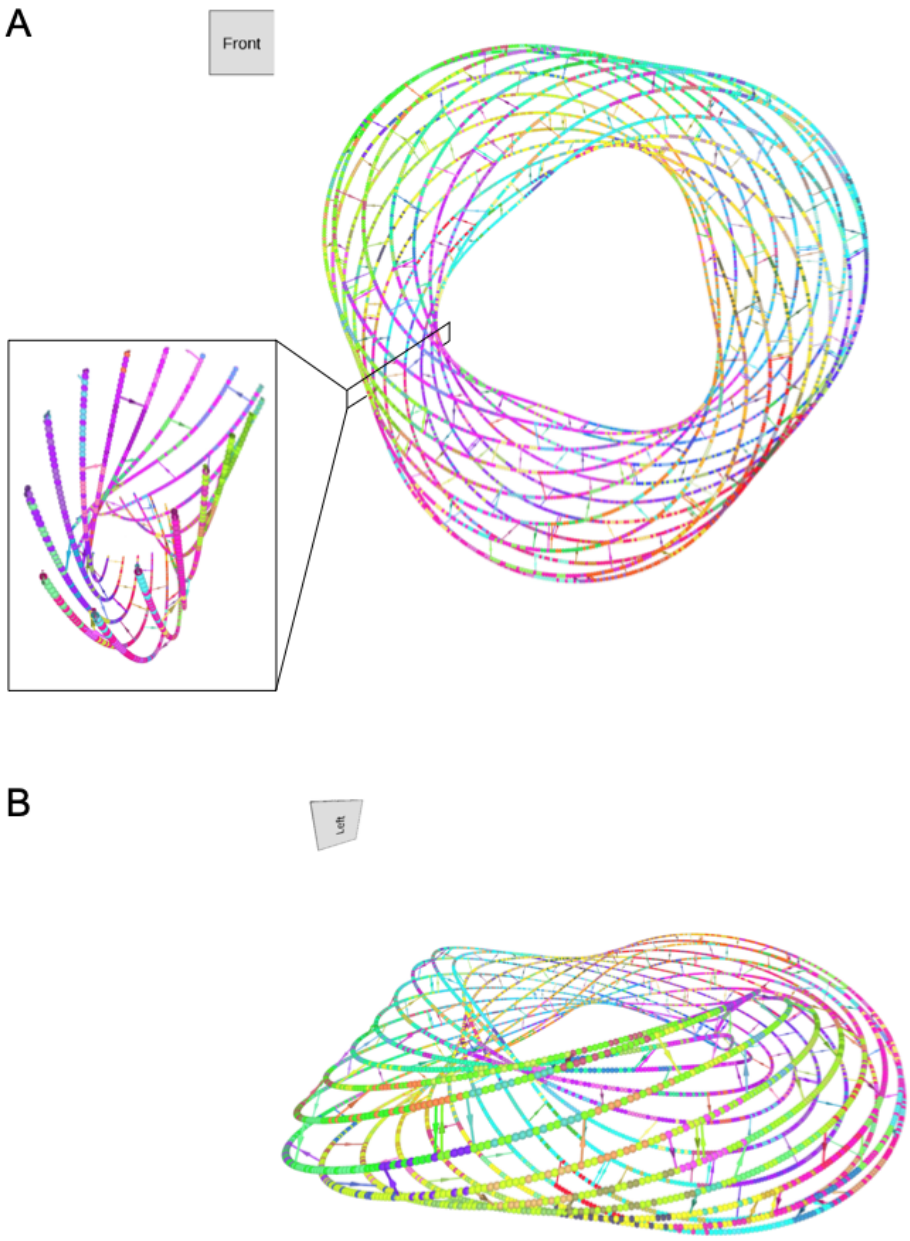


Figure S55: 3D view of the Torus 3 design, line representation. A: Front view and cross-section; B: side view. Each line represents a double helix of DNA. Transversal bars represent crossovers.

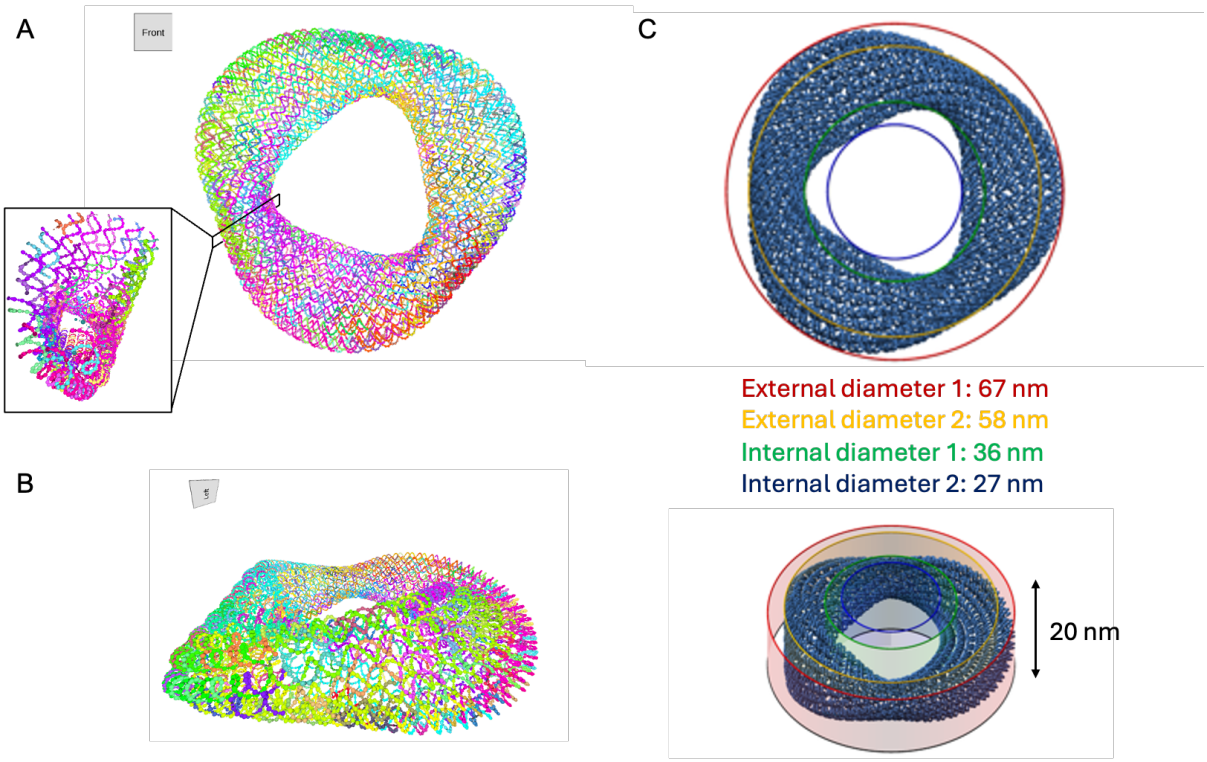


Figure S56: 3D view of the Torus 3 design, helix representation. A: Front view and cross-section; B: side view. Each ball represents a deoxynucleotide; C: Dimensions of the T3 origami. Front view (up), side view (bottom). External diameter 1 of 67 nm (red circle), external diameter 2 of 58 nm (yellow circle), internal diameter 1 of 36 nm (green circle), internal diameter 2 of 27 nm (blue circle), height of 20 nm.

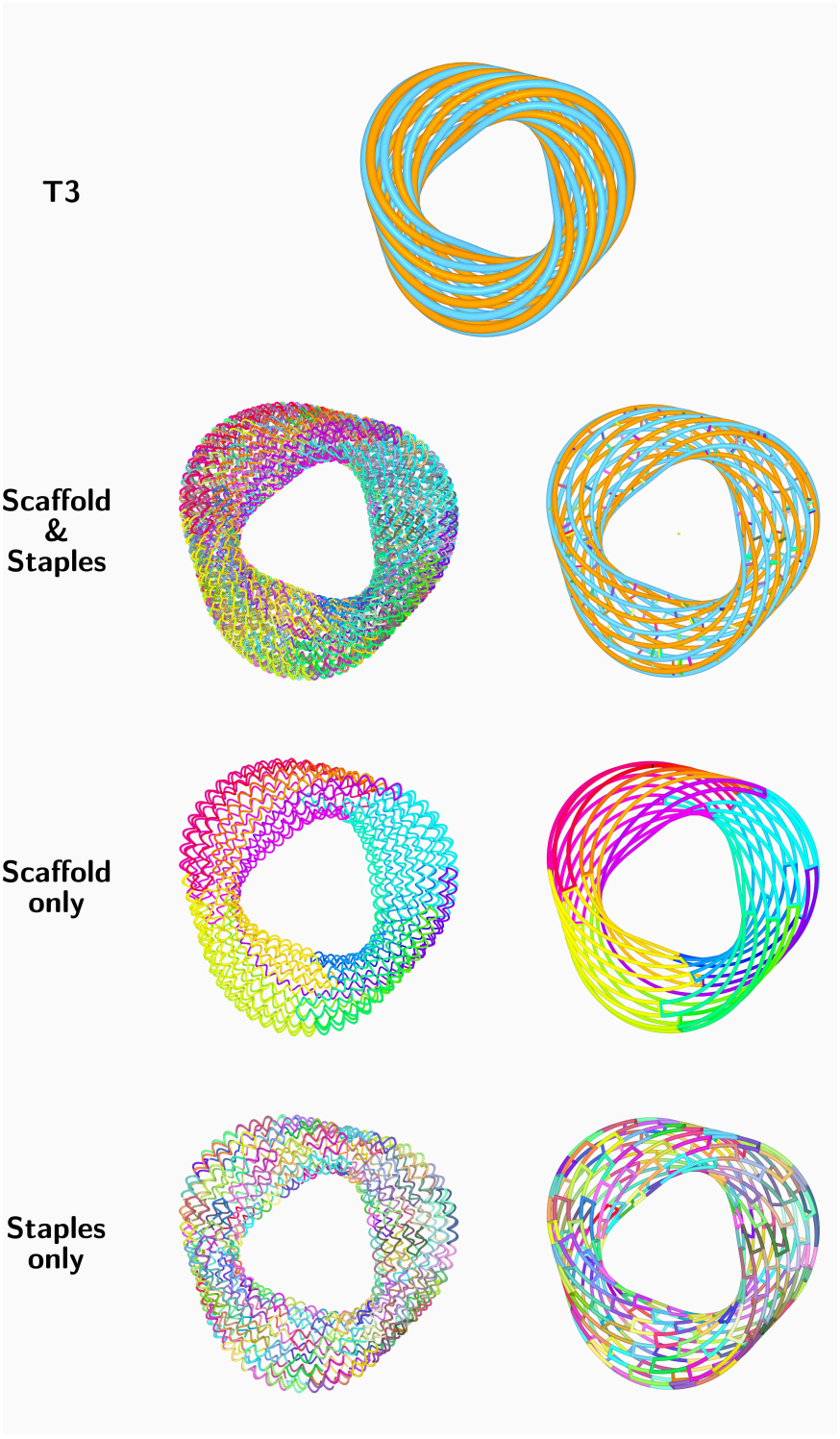


Figure S57: 3D view of the T3 design, helix (left) and line (right) representations. Views of the two spirals (top), the scaffold and staples (middle up), the scaffold (middle down) and the staples (bottom). Transversal bars on the line representation represents a crossover.

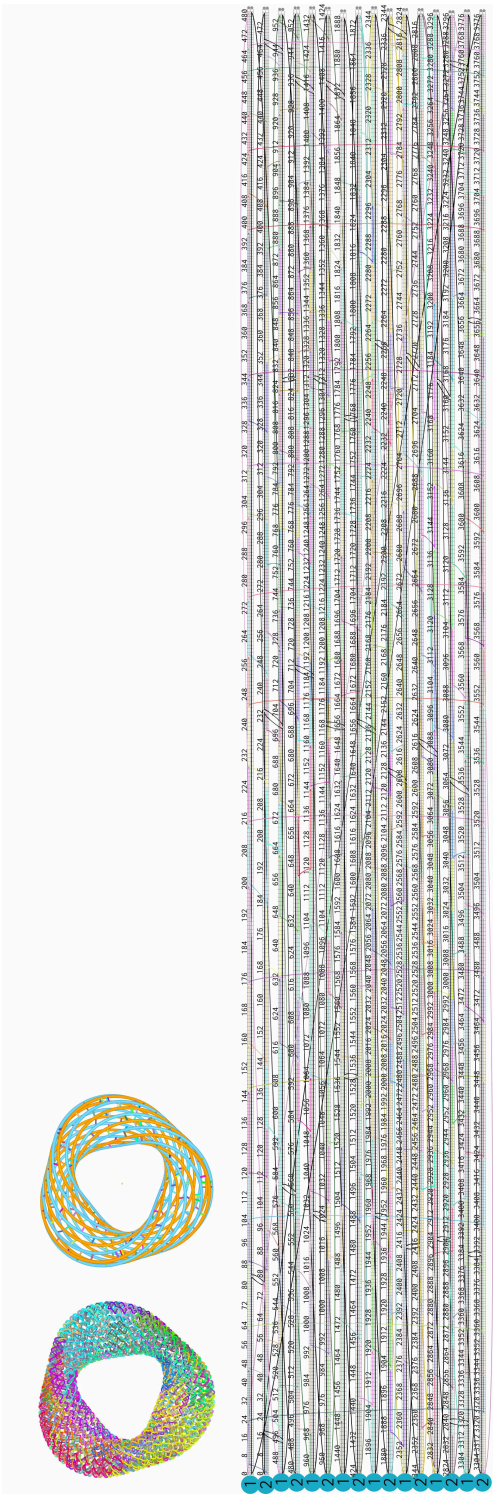

Figure S58: 2D view of the Torus 3 design. Scaffold and staples.

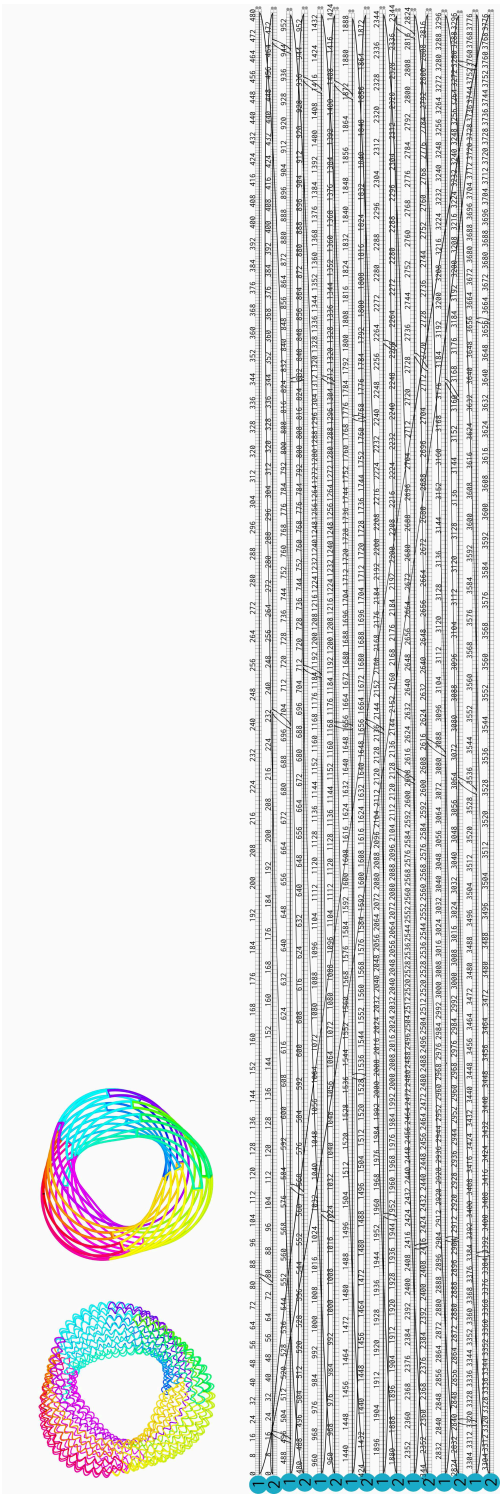

Figure S59: 2D view of the Torus 3 design. Scaffold only.

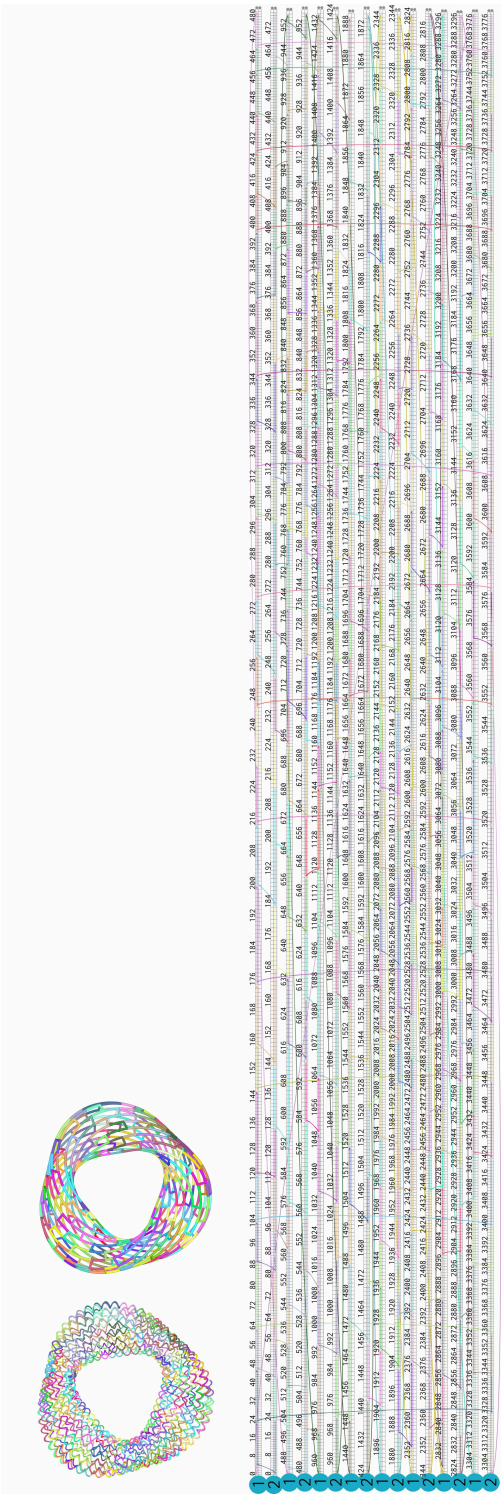

Figure S60: 2D view of the Torus 3 design. Staples only.

### S4.1.4 Torus 4 design

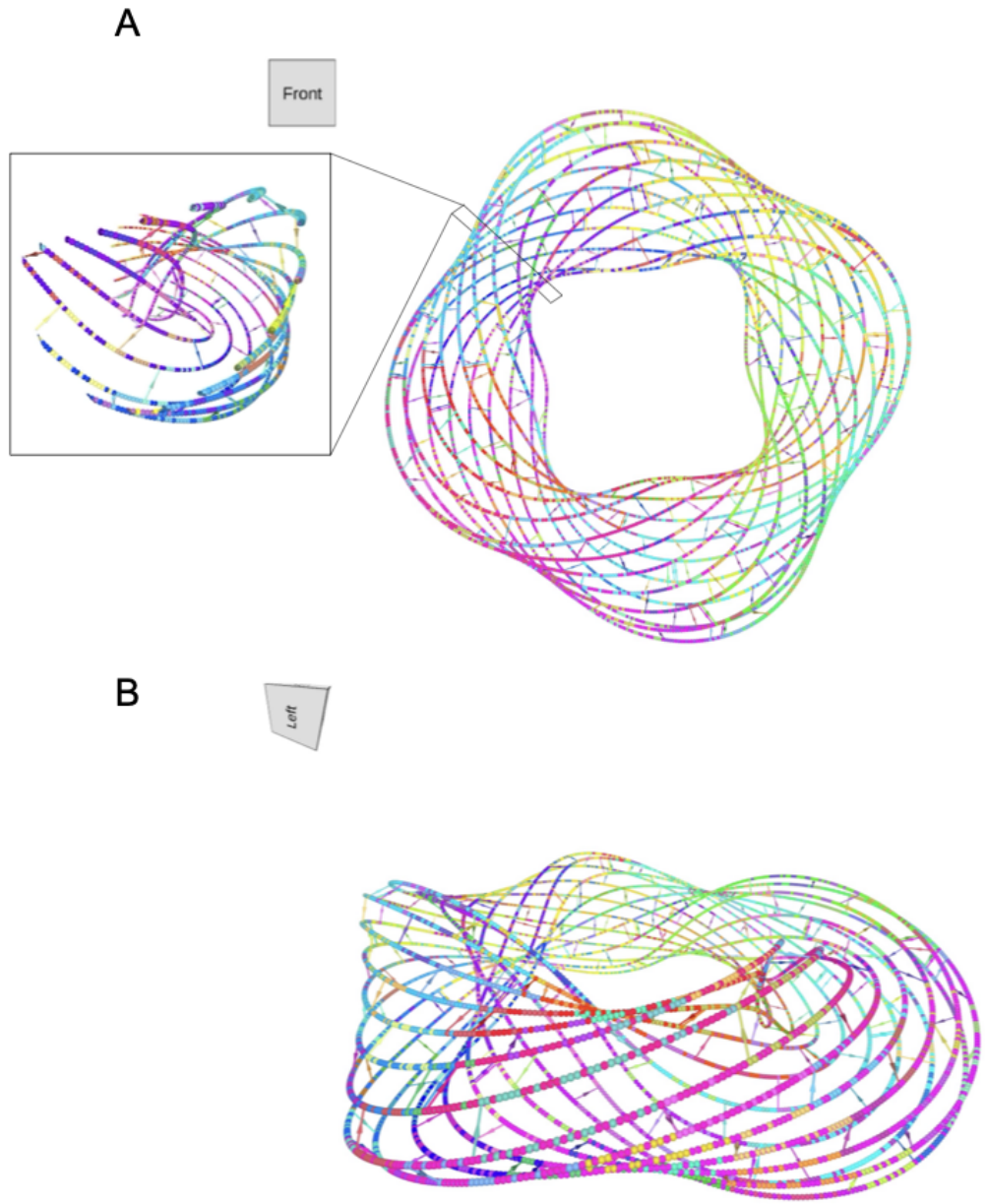


Figure S61: 3D view of the Torus 4 design, line representation. A: Front view and cross-section; B: side view. Each line represents a double helix of DNA. Transversal bars represent crossovers.

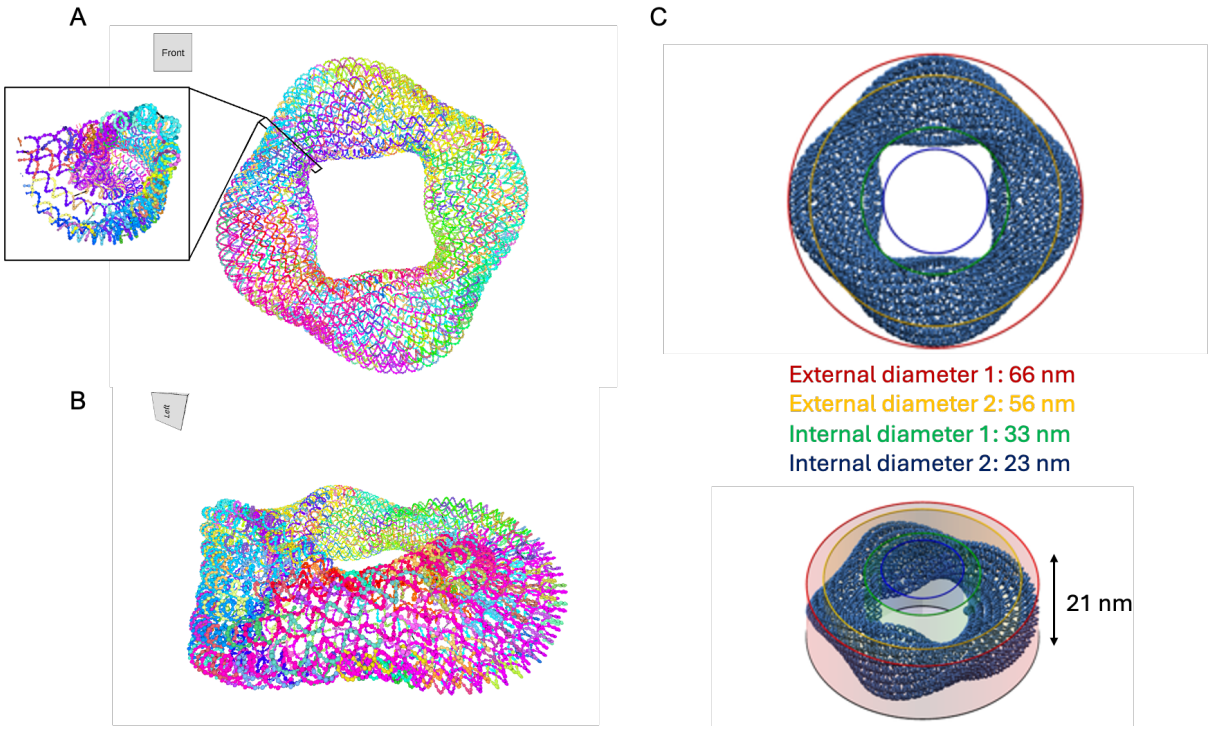


Figure S62: 3D view of the Torus 4 design, helix representation. A: Front view and cross-section; B: side view. Each ball represents a deoxynucleotide; C: Dimensions of the T4 origami. Front view (up), side view (bottom). External diameter 1 of 66 nm (red circle), external diameter 2 of 56 nm (yellow circle), internal diameter 1 of 33 nm (green circle), internal diameter 2 of 23 nm (blue circle), height of 21 nm.

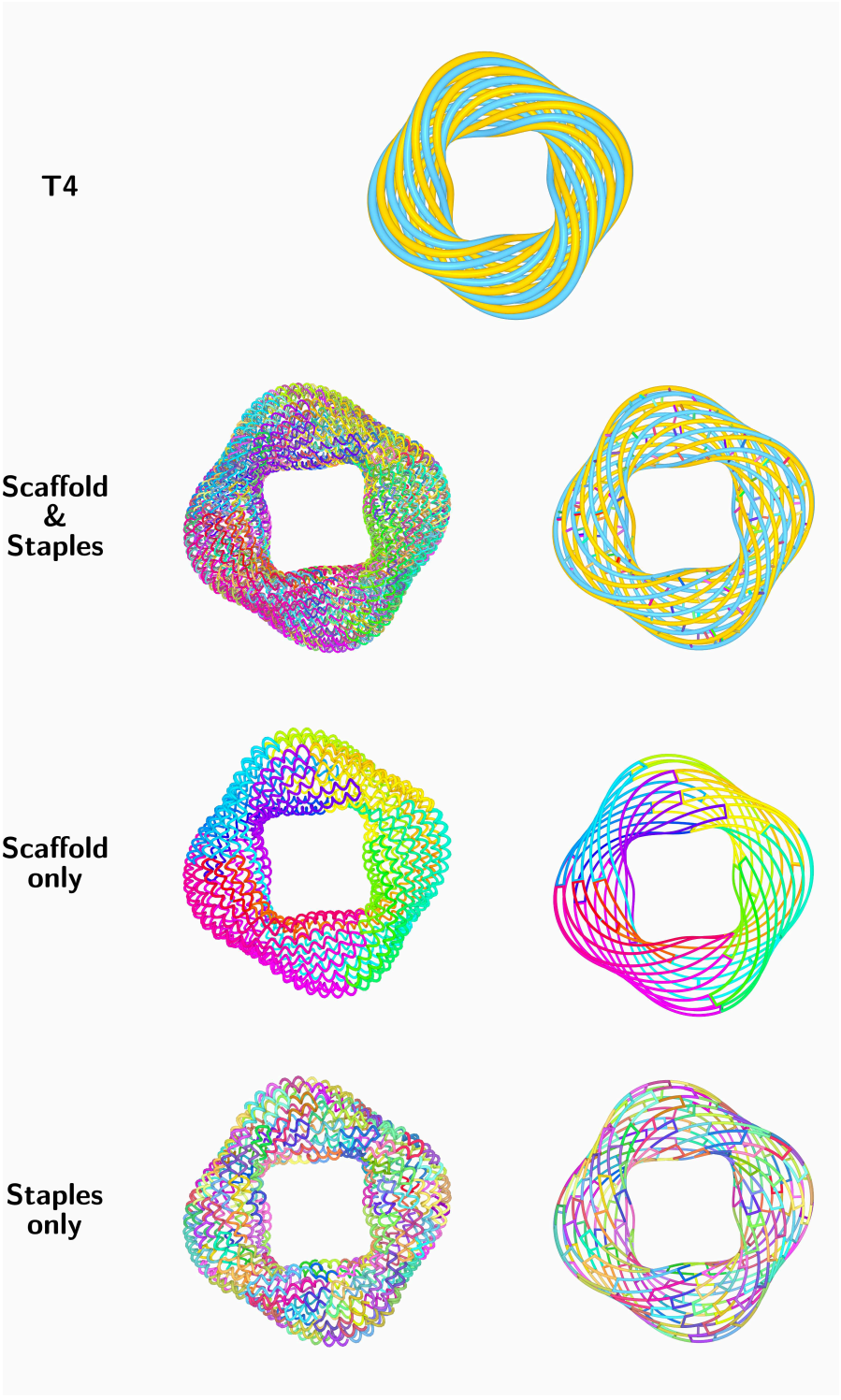


Figure S63: 3D view of the T4 design, helix (left) and line (right) representations. Views of the two spirals (top), the scaffold and staples (middle up), the scaffold (middle down) and the staples (bottom). Transversal bars on the line representation represent a crossover.

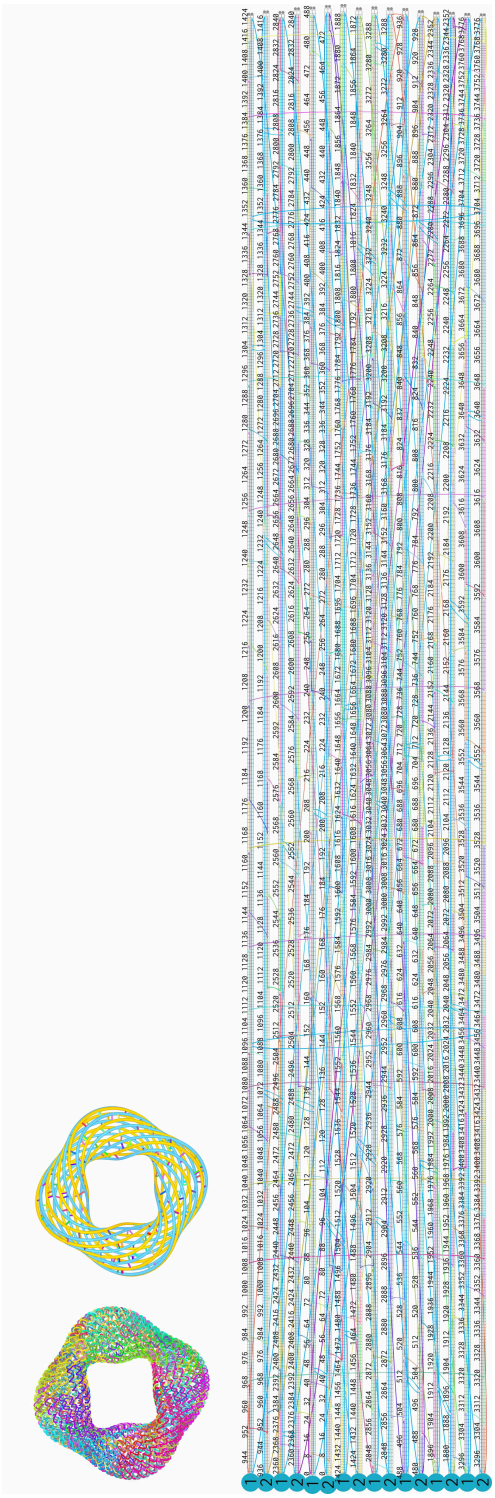

Figure S64: 2D view of the Torus 4 design. Scaffold and staples.

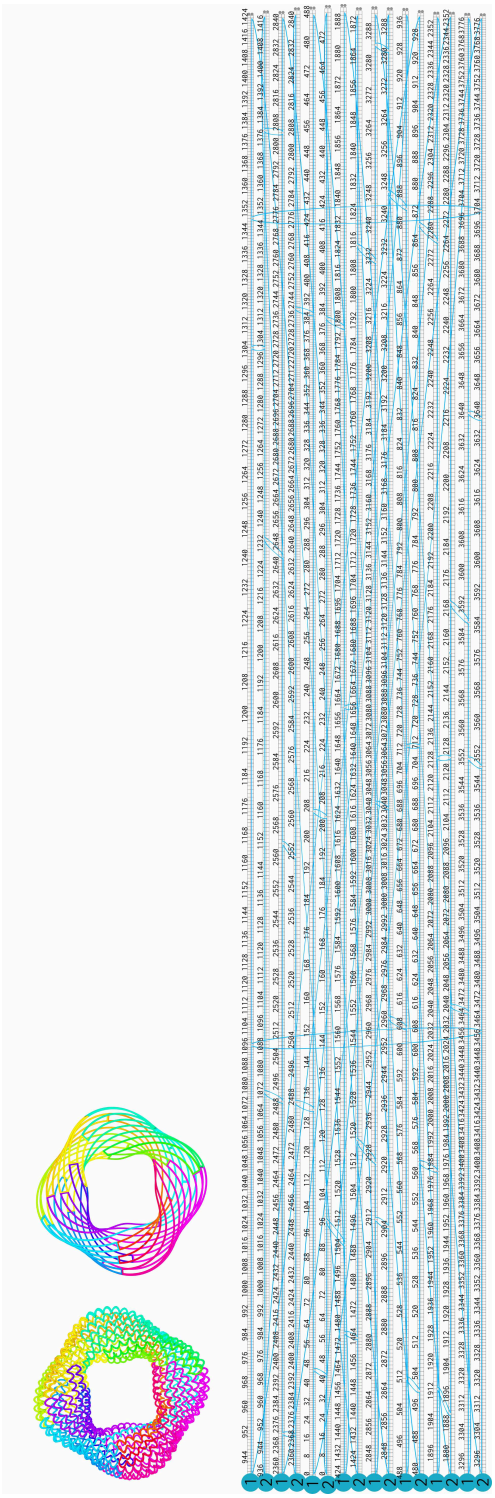

Figure S65: 2D view of the Torus 4 design. Scaffold only.

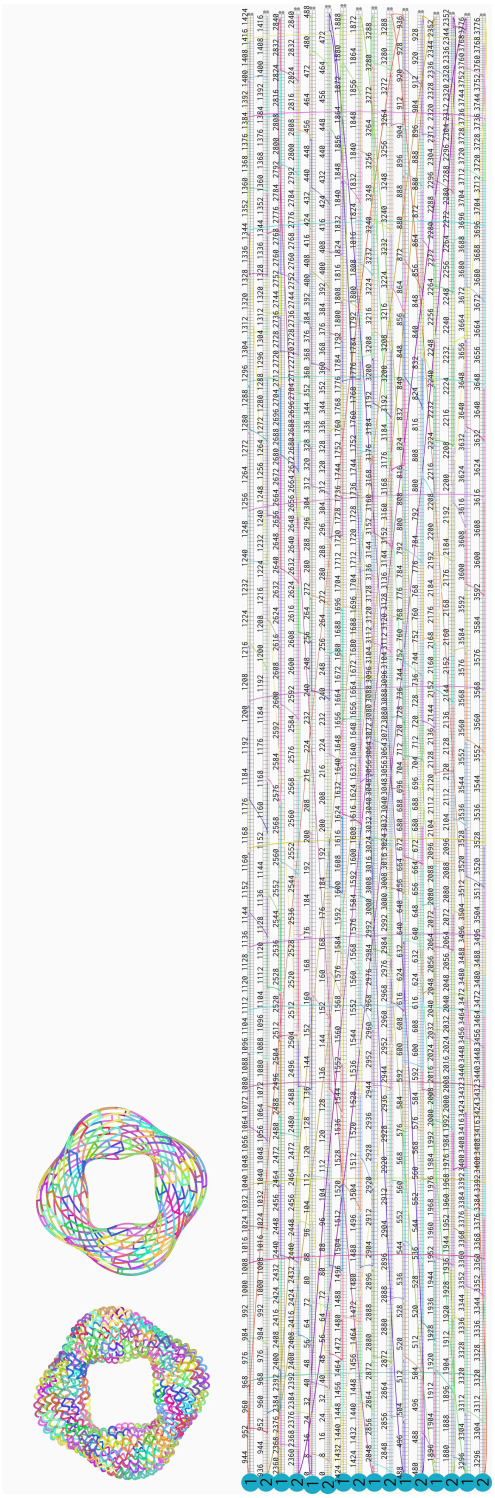

Figure S66: 2D view of the Torus 4 design. Staples only.

### S4.1.5 Torus 5 design

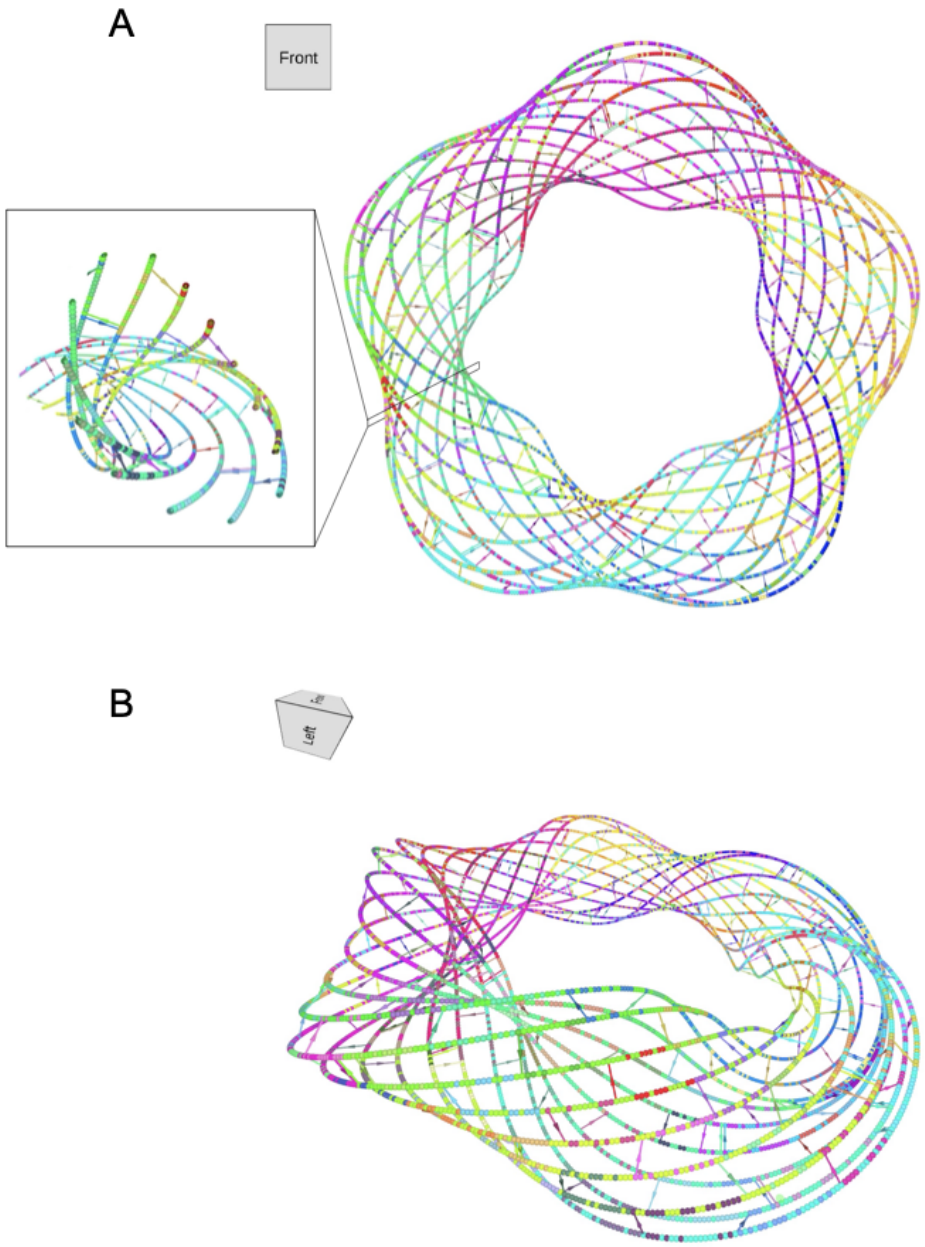


Figure S67: 3D view of the Torus 5 design, line representation. A: Front view and cross-section; B: side view. Each line represents a double helix of DNA. Transversal bars represent crossovers.

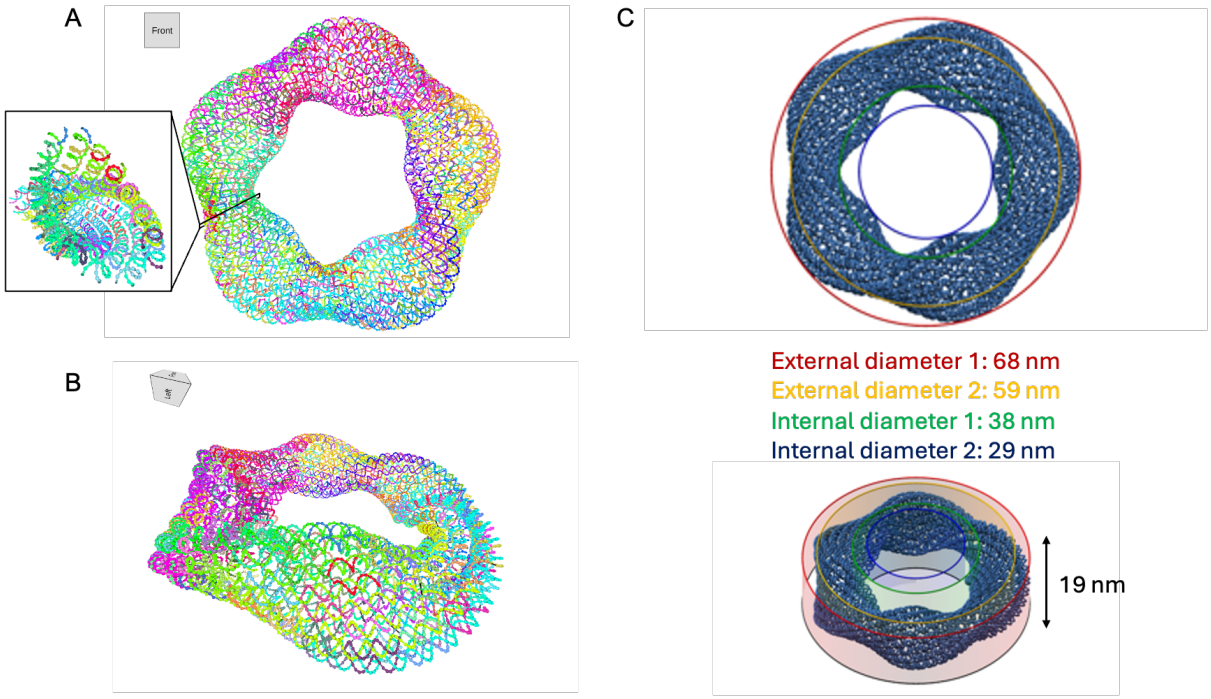


Figure S68: 3D view of the Torus 5 design, helix representation. A: Front view and cross-section; B: side view. Each ball represents a deoxynucleotide; C: Dimensions of the T5 origami. Front view (up), side view (bottom). External diameter 1 of 68 nm (red circle), external diameter 2 of 59 nm (yellow circle), internal diameter 1 of 38 nm (green circle), internal diameter 2 of 29 nm (blue circle), height of 19 nm.

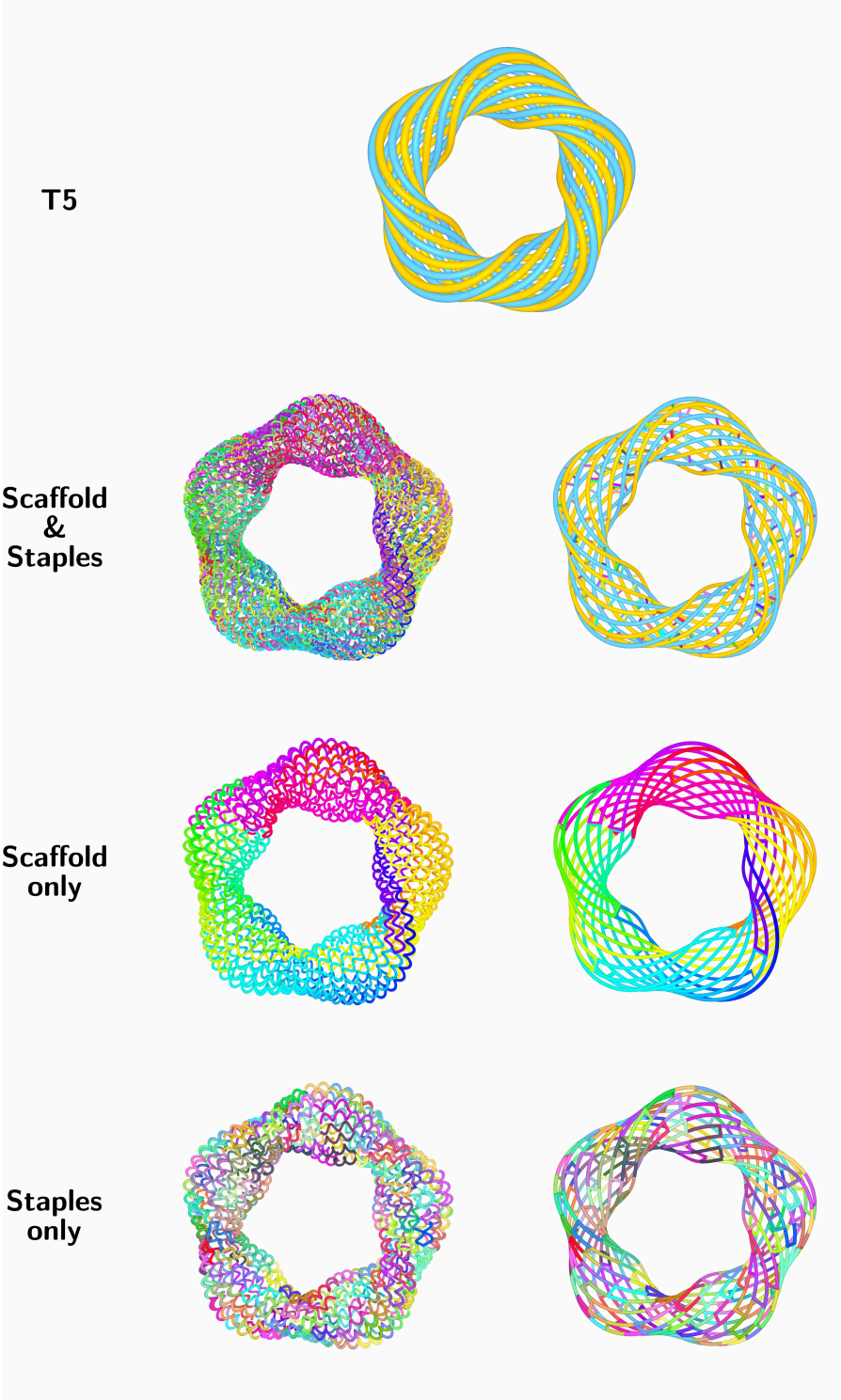


Figure S69: 3D view of the T5 design, helix (left) and line (right) representations. Views of the two spirals (top), the scaffold and staples (middle up), the scaffold (middle down) and the staples (bottom). Transversal bars on the line representation represents a crossover.

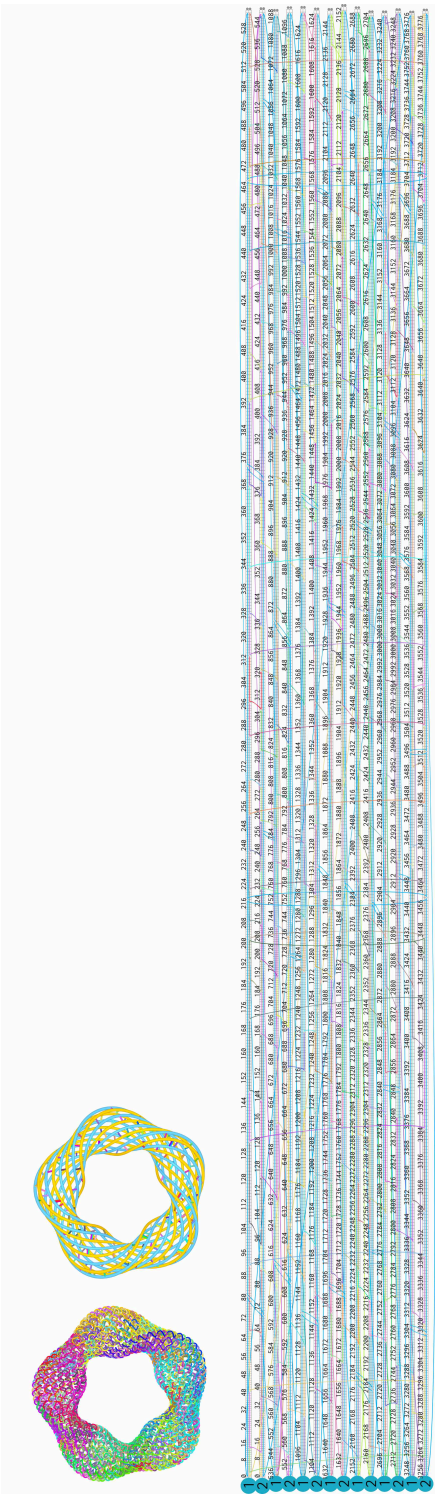

Figure S70: 2D view of the Torus 5 design. Scaffold and staples.

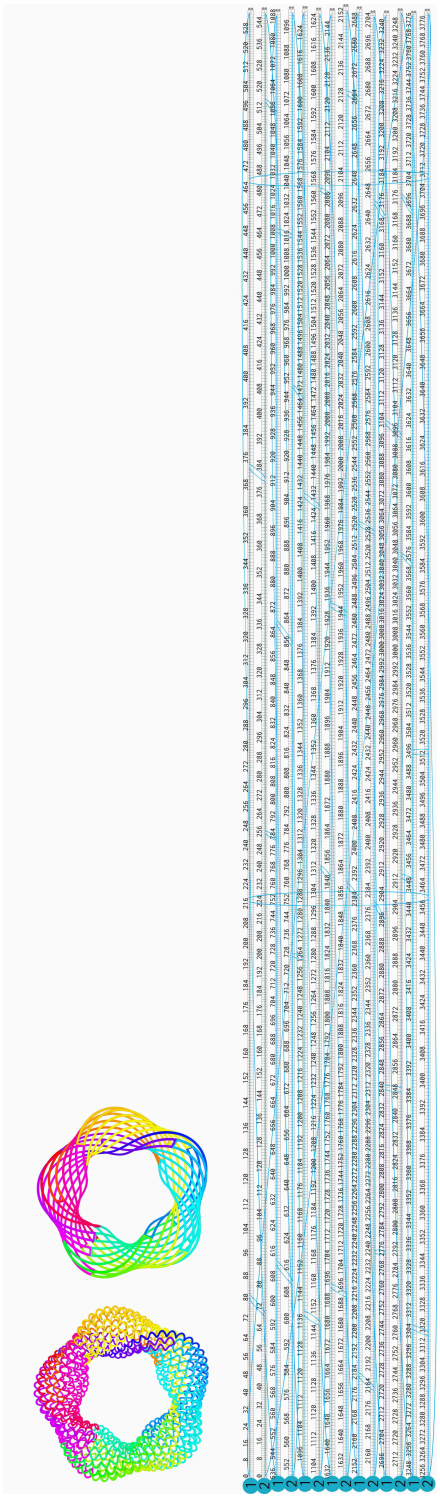

Figure S71: 2D view of the Torus 5 design. Scaffold only.

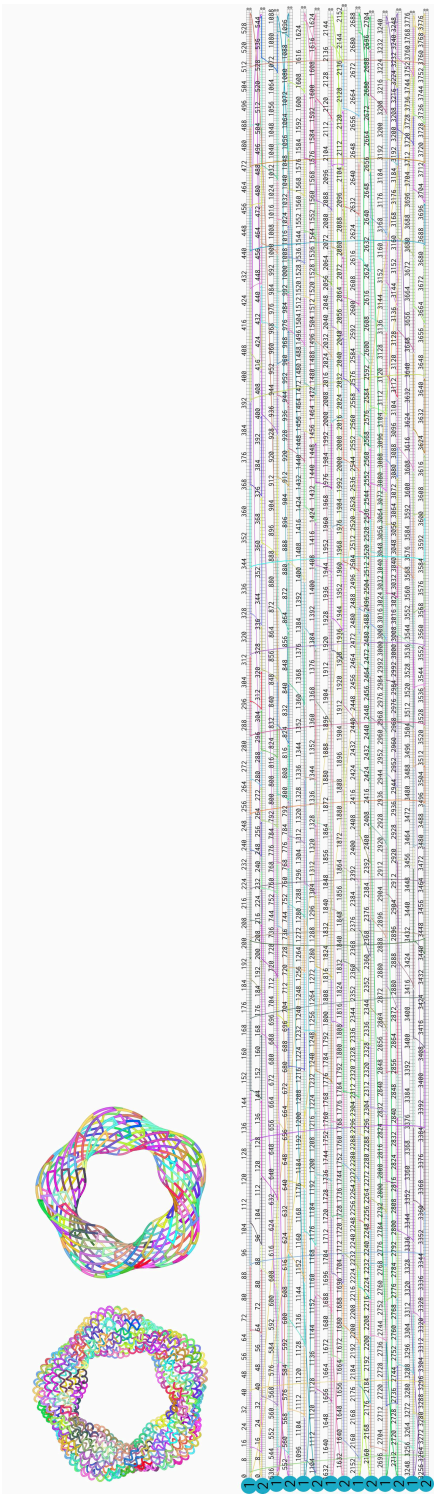

Figure S72: 2D view of the Torus 5 design. Staples only.

### S4.1.6 Torus 6 design

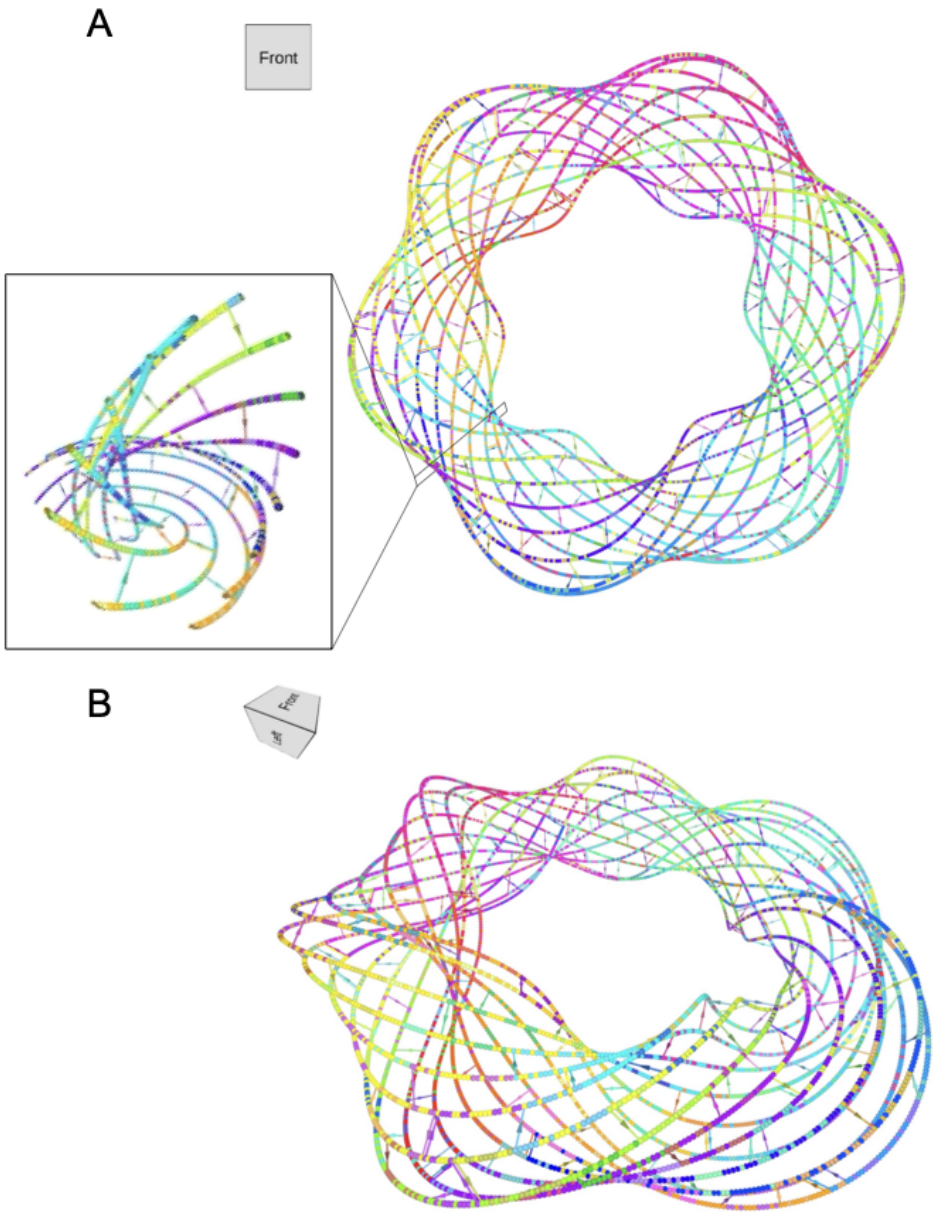


Figure S73: 3D view of the Torus 6 design, line representation. A: Front view and cross-section; B: side view. Each line represents a double helix of DNA. Transversal bars represent crossovers.

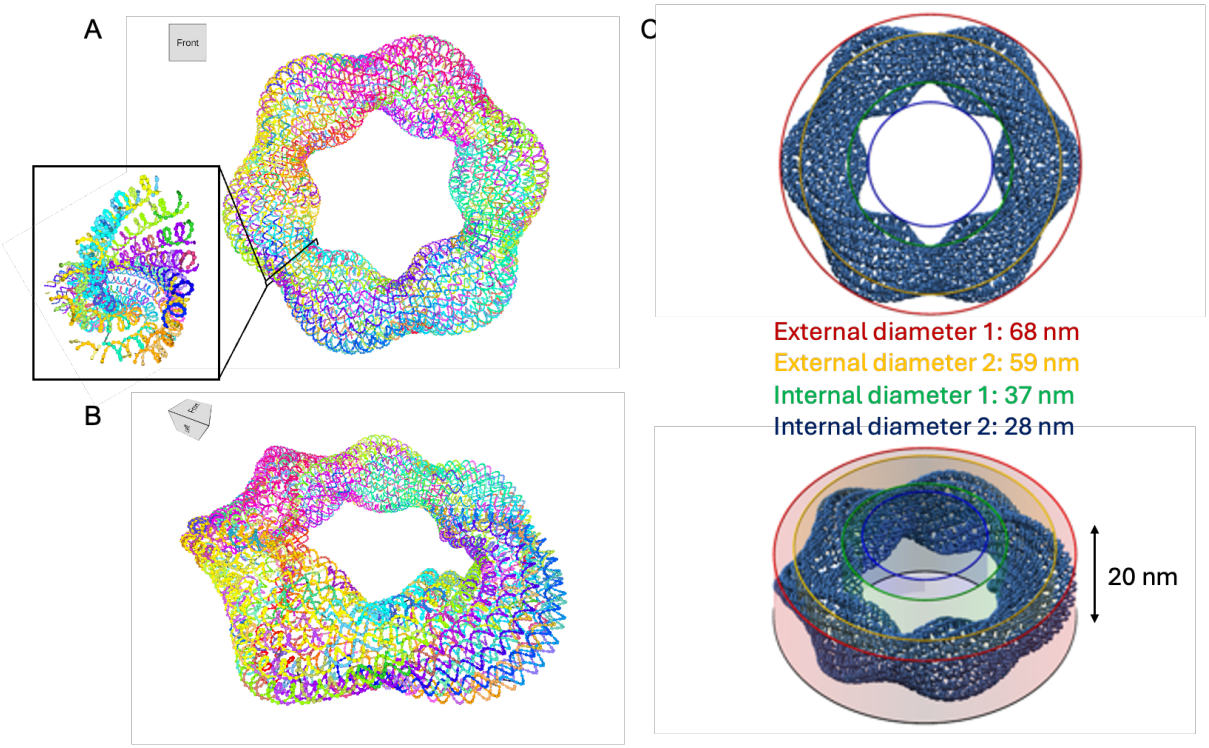


Figure S74: 3D view of the Torus 6 design, helix representation. A: Front view and cross-section; B: side view. Each ball represents a deoxynucleotide; C: Dimensions of the T6 origami. Front view (up), side view (bottom). External diameter 1 of 68 nm (red circle), external diameter 2 of 59 nm (yellow circle), internal diameter 1 of 37 nm (green circle), internal diameter 2 of 28 nm (blue circle), height of 20 nm.

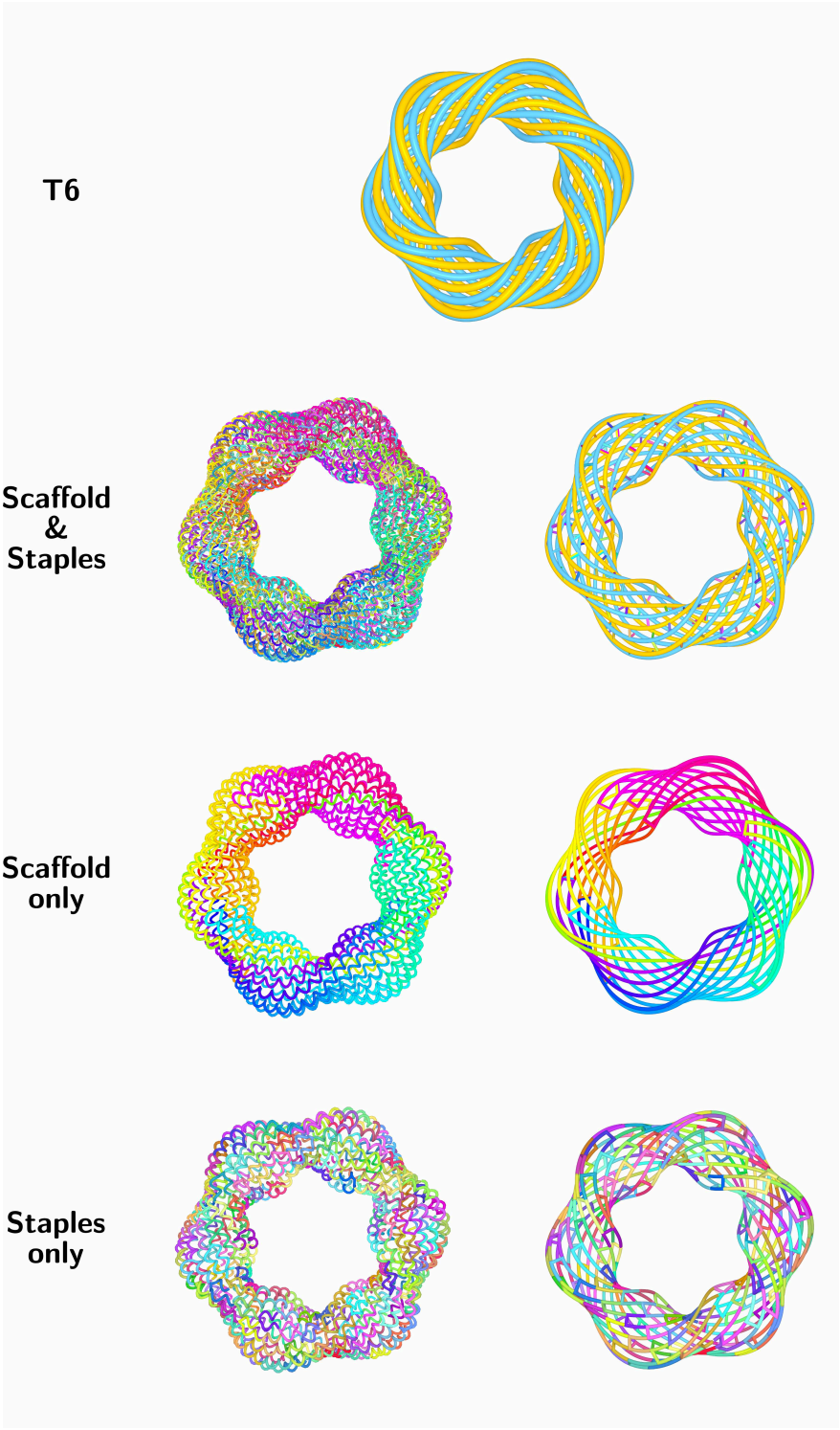


Figure S75: 3D view of the Torus 6 design, helix (left) and line (right) representations. Front views of the two spirals (top), the scaffold and staples (middle up), the scaffold (middle down) and the staples (bottom). Transversal bars on the line representation represents a crossover.

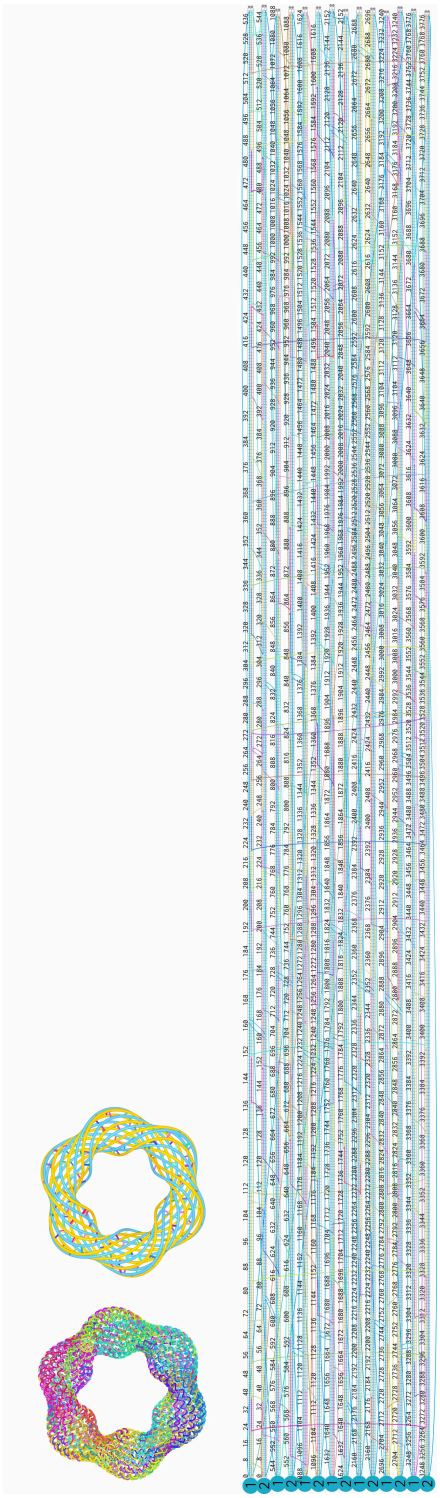

Figure S76: 2D view of the Torus 6 design. Scaffold and staples.

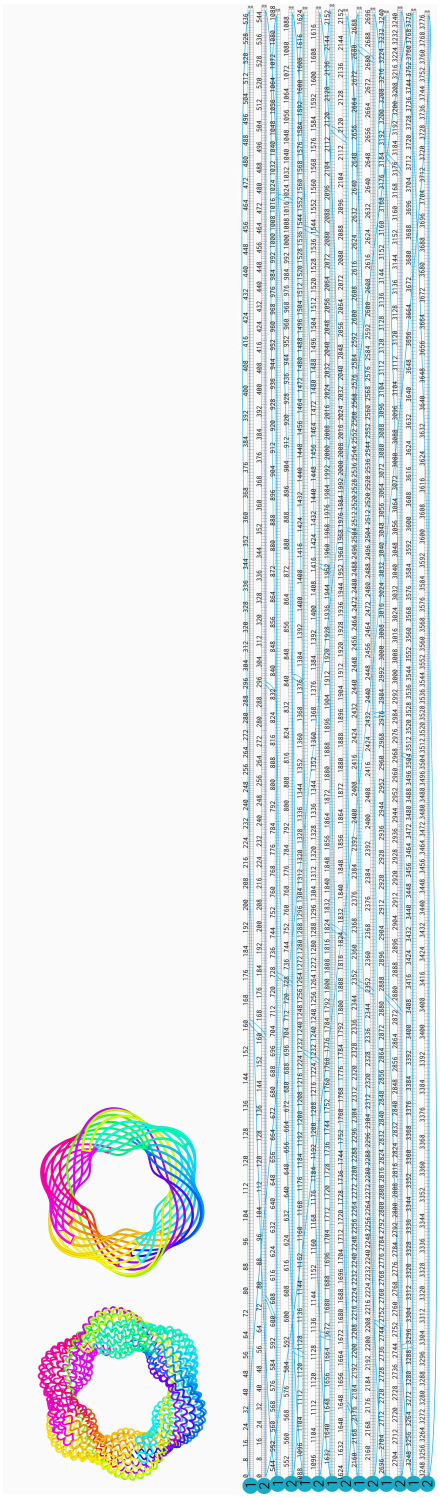

Figure S77: 2D view of the Torus 6 design. Scaffold only.

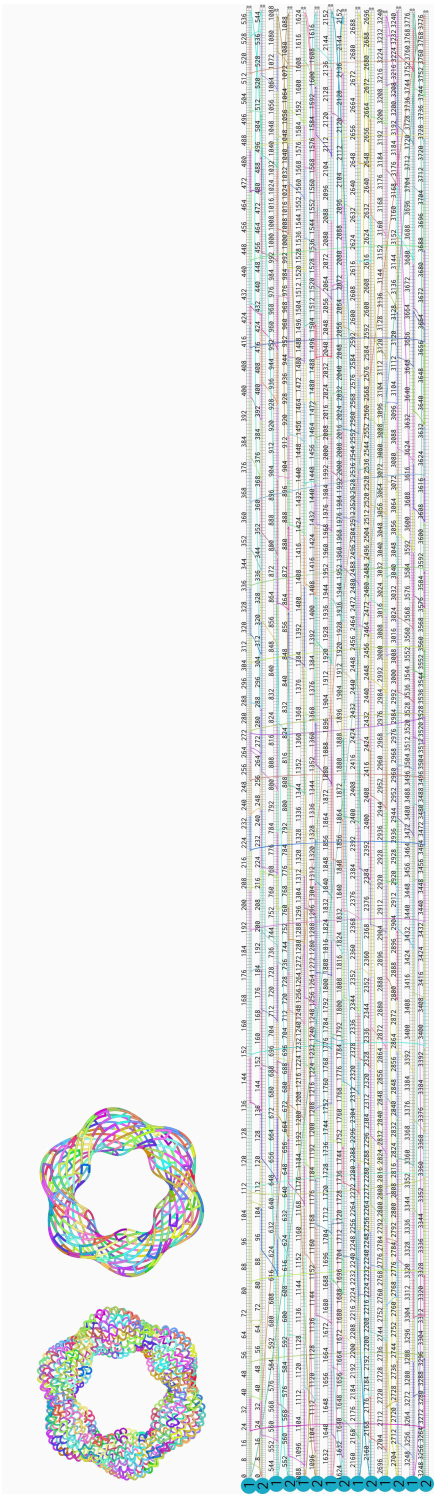

Figure S78: 2D view of the Torus 6 design. Staples only.

## S4.2 Tori experimental validation

### S4.2.1 Torus I experimental validation

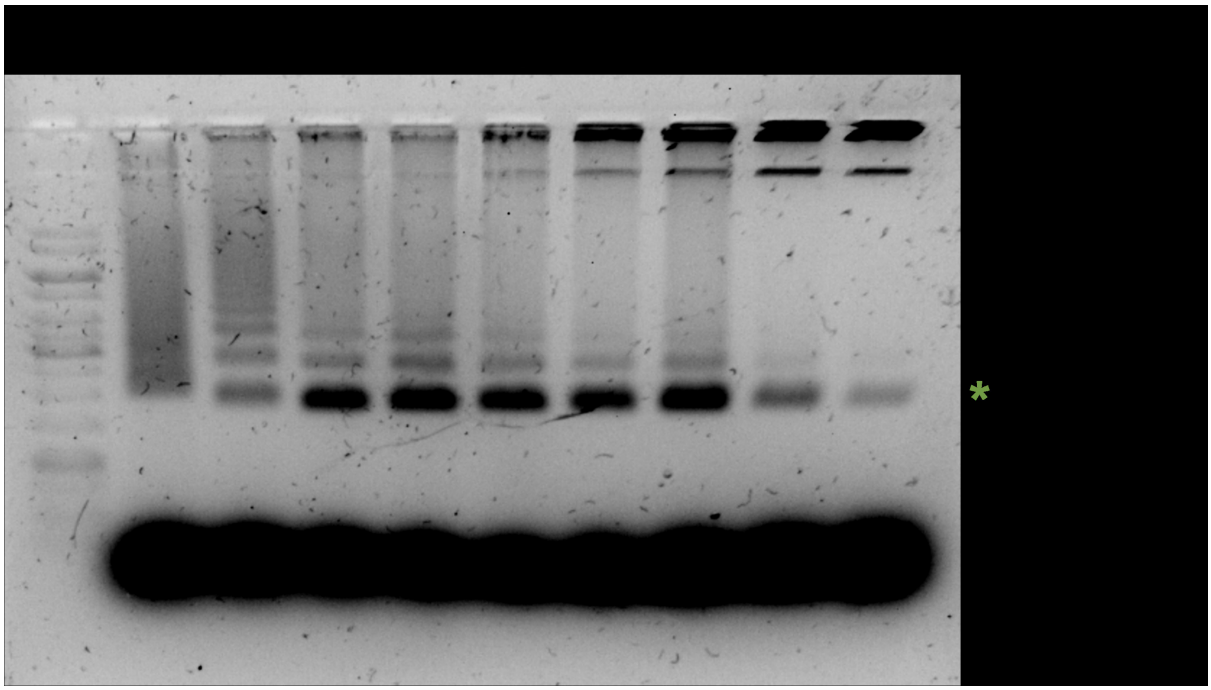

Figure S79: Gel analysis of the influence of $MgCl_2$ concentration on folding quality of the T1 origami. The foldings were analyzed by agarose gel electrophoresis (1%). L : 1kb DNA ladder ; Folding ramp: 65°C during 15 min, 60°C to 40°C -1°C/2h, 10°C Hold.

### S4.2.2 Tore VI experimental optimization and validation

To determine good self-assembly conditions, we first focused on optimizing nanostructure T6. Agarose gel electrophoresis analysis of the assembly conditions revealed an optimal assembly at 18 mM with an annealing ramp over 33 hours (figs. S80 and S81). ns-TEM analysis of the gel purified T6 origami and two-dimensional class averages confirmed the fully formed origami according to the design and 2D projection simulations (figs. S82 and S83). We validated the accuracy of the designed structure by generating a 3D electron density map through single-particle cryo-TEM (Fig. 2 and figs. S84 and S85) which revealed the distinctive six twists per ring features within the resolution obtained.

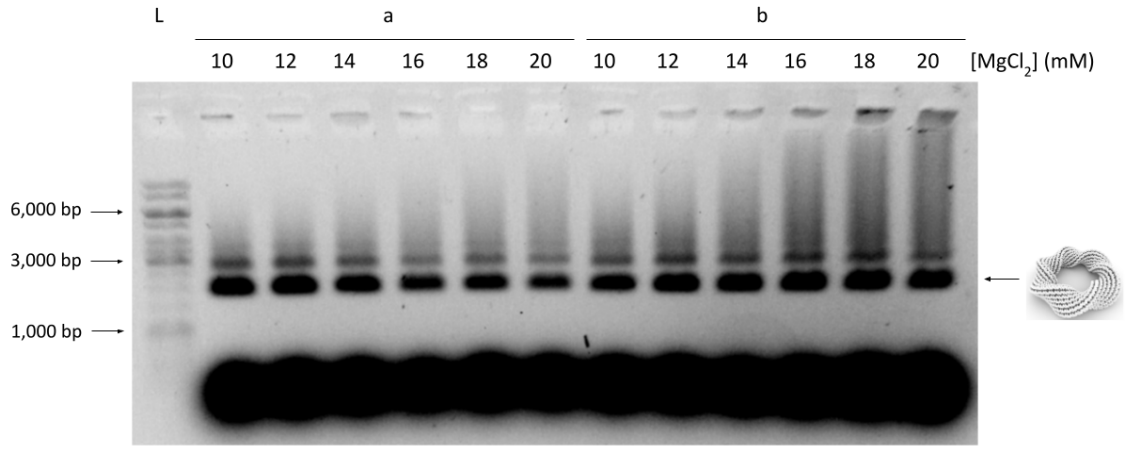


Figure S80: Gel analysis of the influence of $MgCl_2$ concentration on folding quality of the Tore 6. The foldings were analyzed by agarose gel electrophoresis (1%). L: 1kb DNA ladder; a: 65°C during 15 min, 60°C to 40°C -1°C/10minutes, 10°C Hold; b: 65°C during 15 min, 60°C to 40°C -1°C/1h, 10°C Hold.

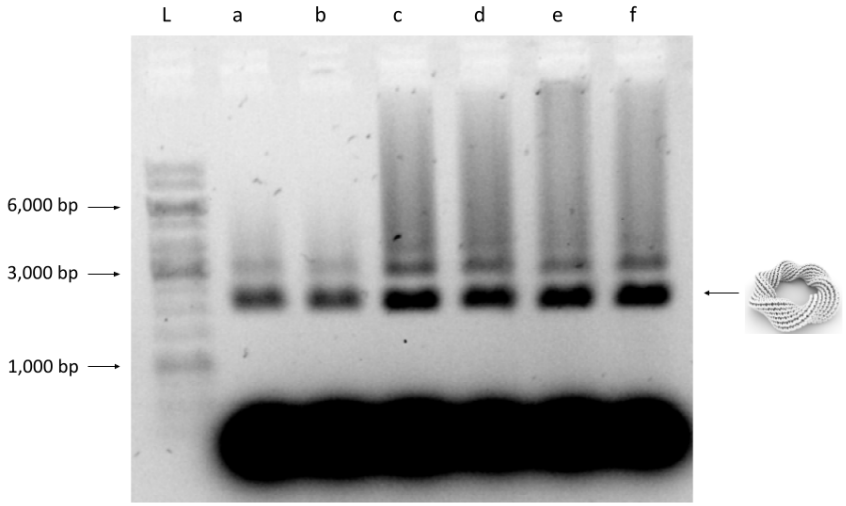


Figure S81: Gel analysis of the influence of different folding ramps on folding quality of the Tore 6. The foldings were analyzed by agarose gel electrophoresis (1%).. L: 1kb DNA ladder; a: 65°C during 15 min, 60°C to 40°C -1°C/5minutes, 10°C Hold; b: 65°C during 15 min, 60°C to 40°C -1°C/10minutes, 10°C Hold; c: 65°C during 15 min, 65°C to 55°C -1°C/10minutes, 55°C to 25°C -1°C/1h, 25°C Hold; d: 65°C during 15 min, 65°C to 50°C -1°C/10minutes, 50°C to 25°C -1°C/1h, 25°C Hold; e: 80°C during 15 min, 80°C to 55°C -1°C/10minutes, 55°C to 25°C -1°C/1h, 25°C Hold; f: 80°C during 15 min, 80°C to 25°C -1°C/10minutes, 25°C Hold.

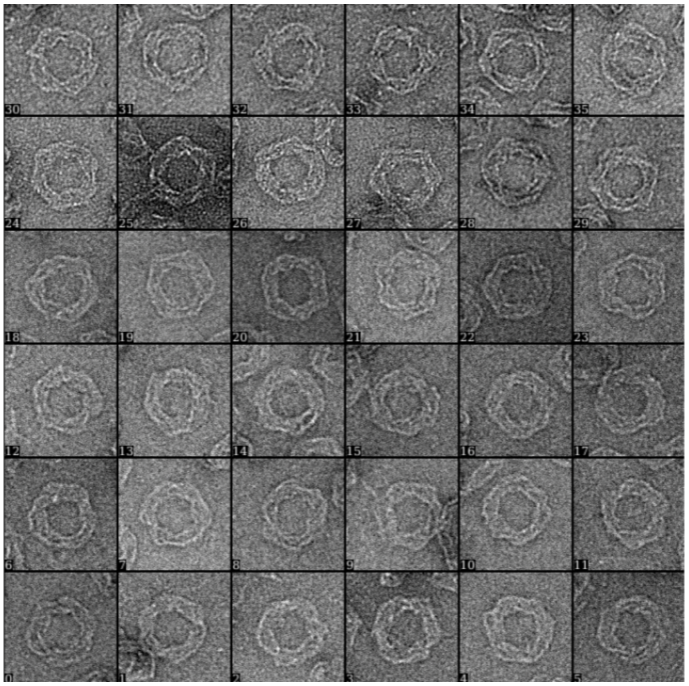

Figure S82: Transmission Electron Microscope (TEM) micrographs of typical particules of the Tore 6. Each box is 99 nm x 99 nm.

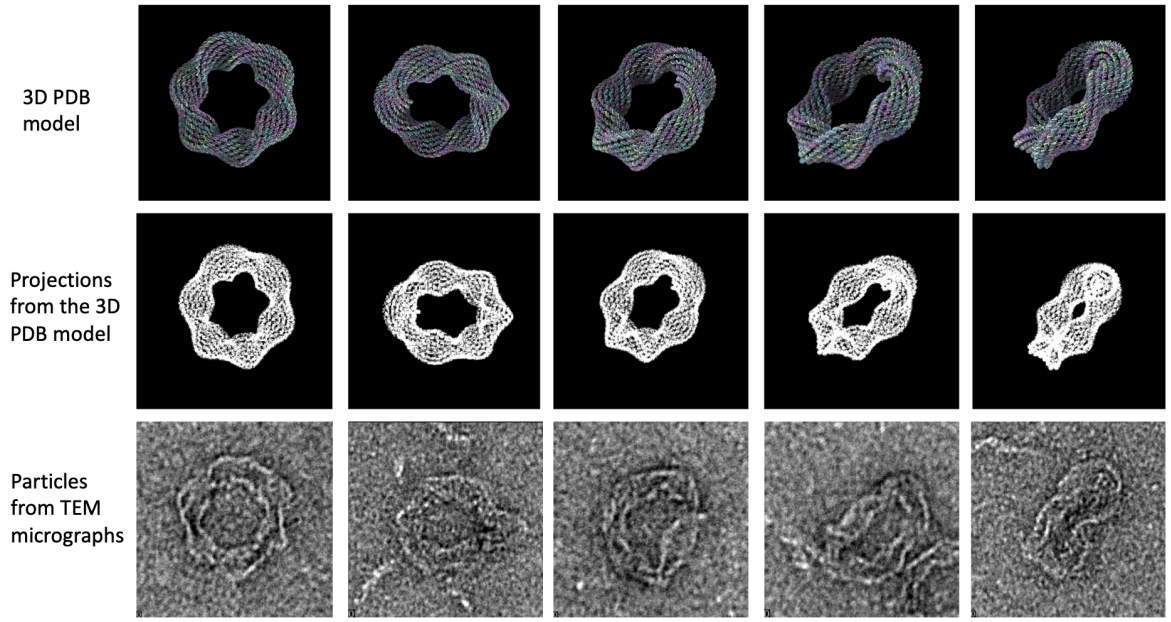


Figure S83: Tore 6 projections from 3D PDB model. Observed particles and representative projections from 3D PDB model of the Tore 6 showing different orientations from TEM micrographs. Each box is 99 nm x 99 nm.

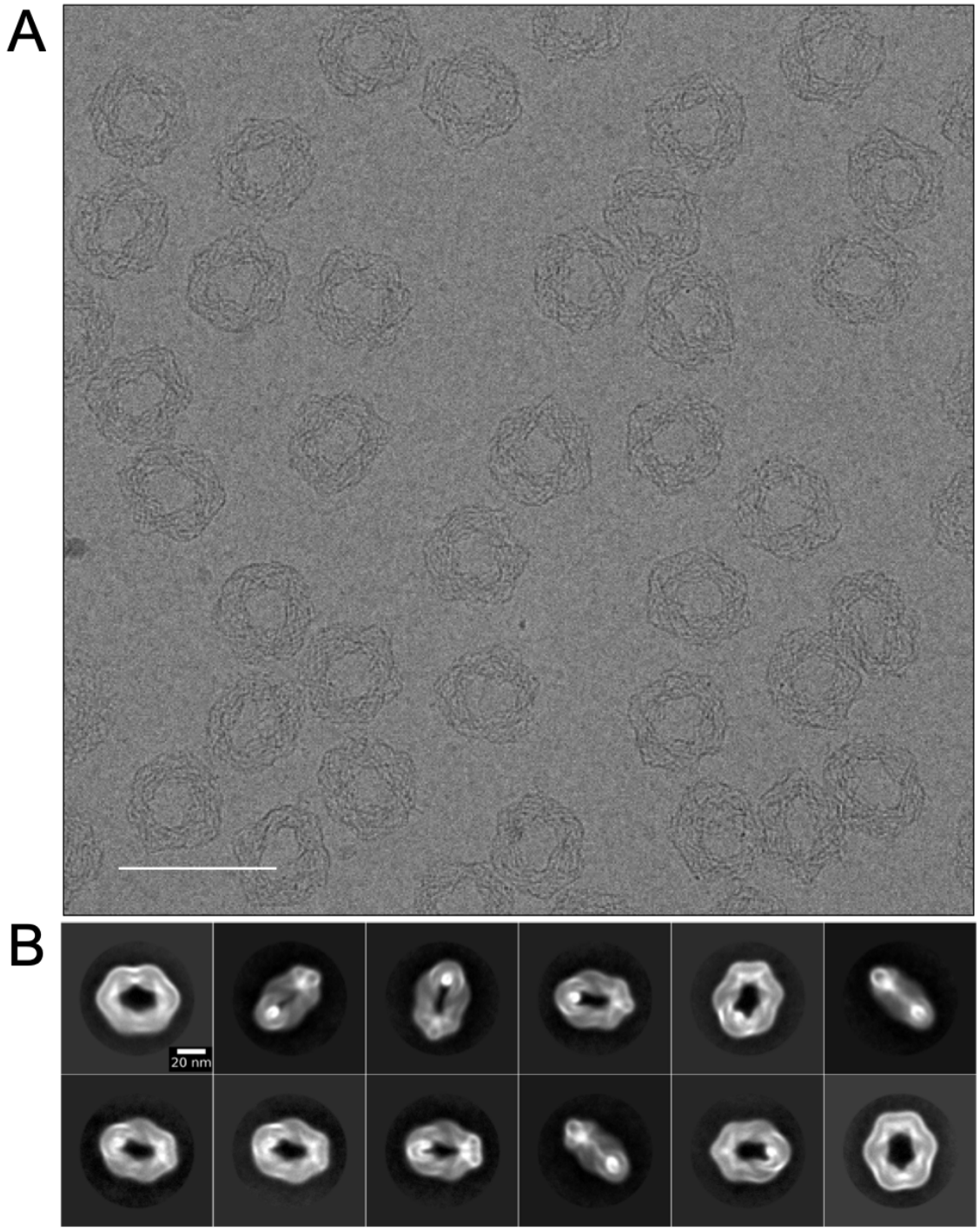


Figure S84: Cryo-EM images analysis for Tore 6. A: Exemplary micrograph of a total of 15,127 movie stacks. Scale bar = 100 nm. B: Representative 2D Class averages.

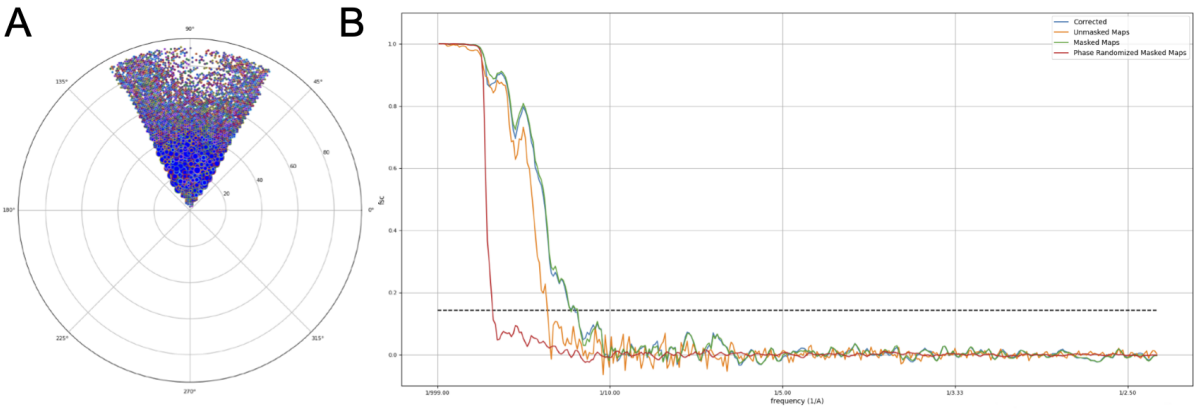


Figure S85: Cryo-EM map determination for Tore 6. A: Histogram representing the angular distribution of particles. B: FSC plot.

### S4.2.3 Tore II to Tore IV experimental validation

This optimized self-assembly protocol was employed for three additional structures (T2 to T4) (figs. S86 to S88 and had to be optimized for T5 (figs. S89 to S92).

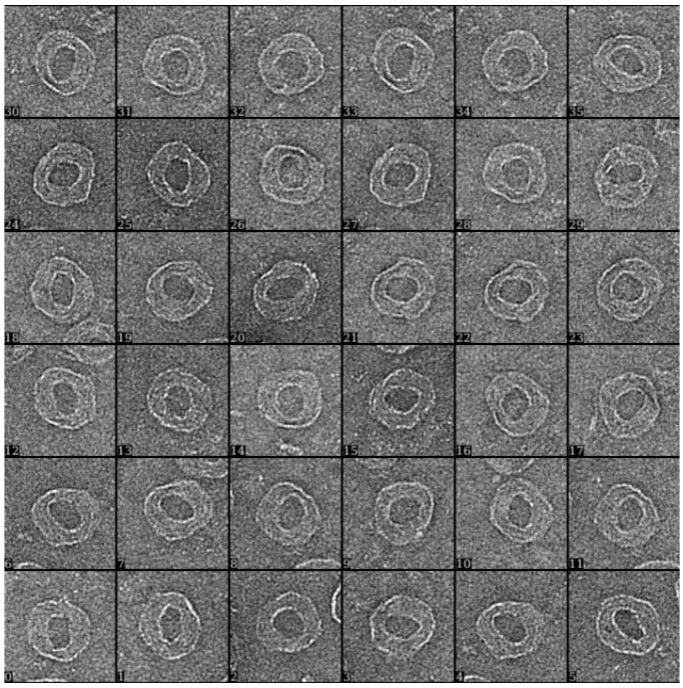

Figure S86: Transmission Electron Microscope (TEM) micrographs of typical particules of the Tore 2. Each box is 99 nm x 99 nm.

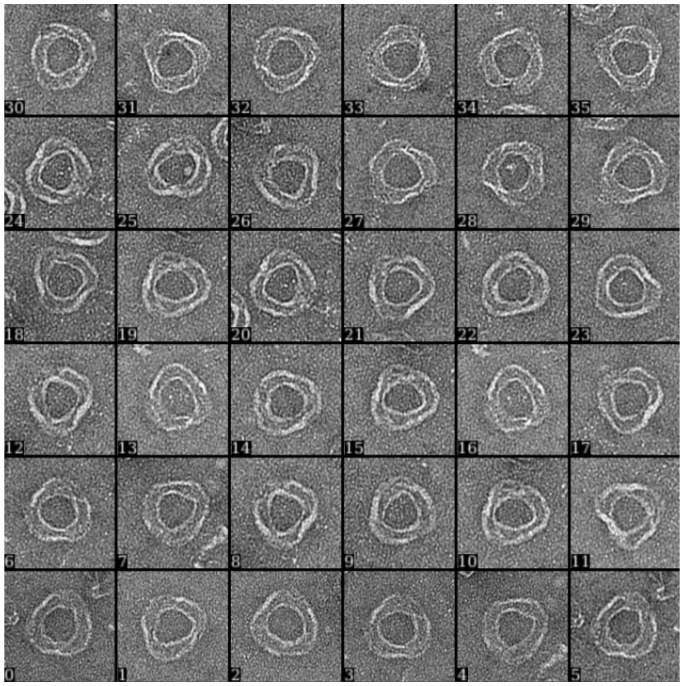


Figure S87: Transmission Electron Microscope (TEM) micrographs of typical particules of the Tore 3. Each box is 99 nm x 99 nm.

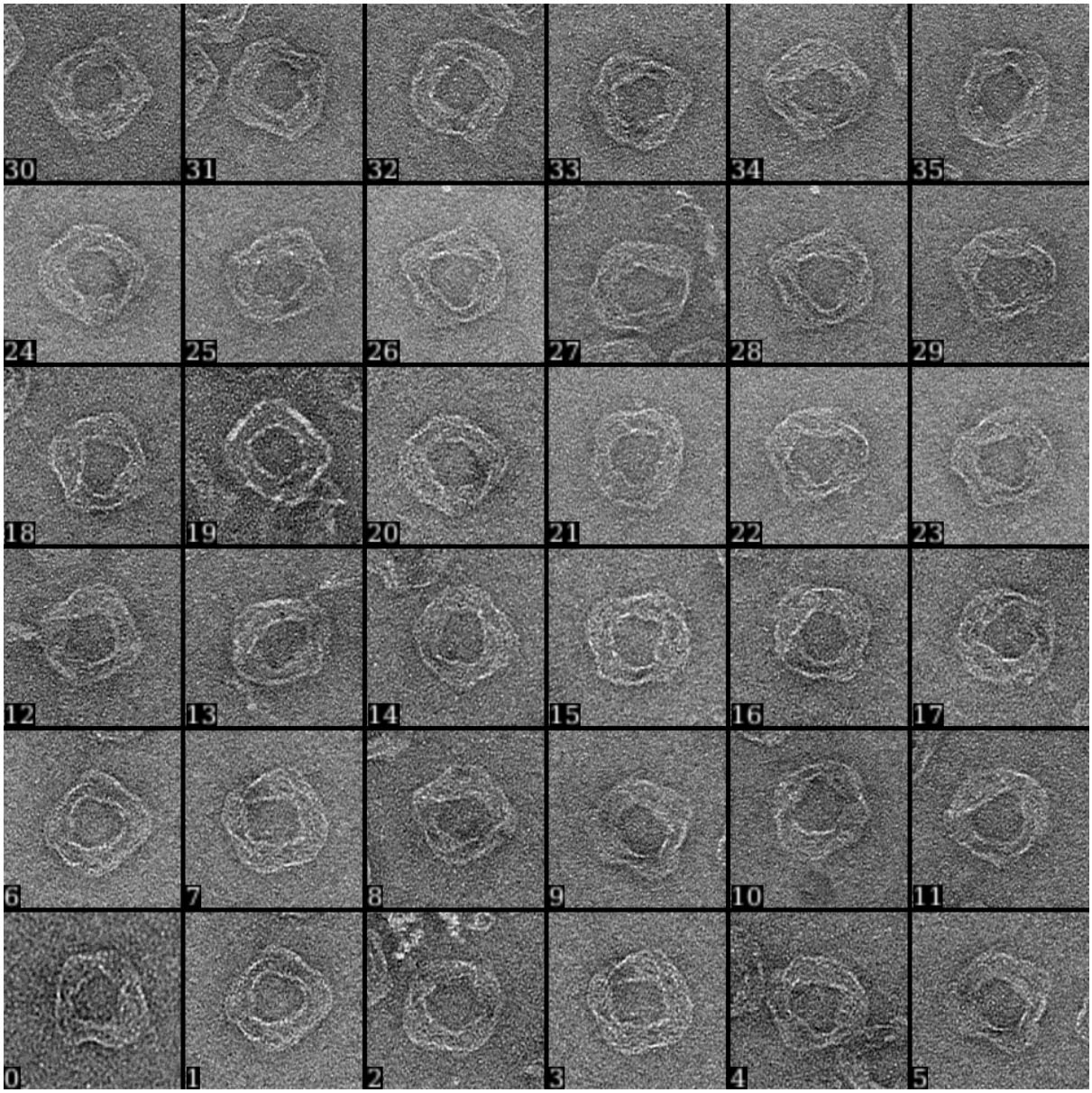


Figure S88: Transmission Electron Microscope (TEM) micrographs of typical particles of the Tore 4. Each box is 99 nm x 99 nm.

### S4.2.4 T5: optimization of folding conditions and experimental validation

**Optimization of the folding conditions of the T5 origami (figs. S89 to S92).** Despite four different tested folding ramps with a scaffold concentration of 20 nM and staples oligonucleotides in a 10-fold excess, the gel analysis of the T5 showed some aggregates in the well, with different $MgCl_2$ concentrations and folding ramps (figs. S89 to S92).

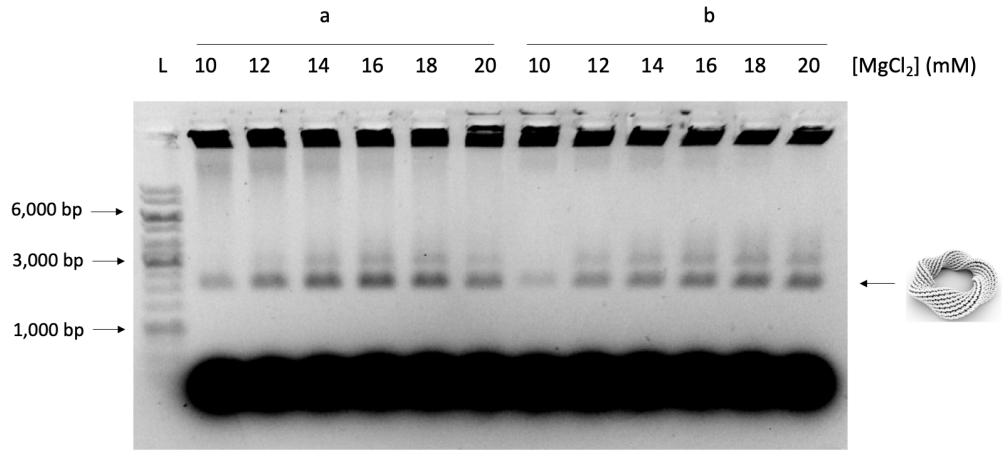


Figure S89: Gel analysis of the influence of $MgCl_2$ concentration on folding quality of the Tore 5. The foldings were analyzed by agarose gel electrophoresis (1%). L: 1kb DNA ladder ; a: 65°C during 15 min, 60°C to 40°C -1°C/10minutes, 10°C Hold ; b: 65°C during 15 min, 60°C to 40°C -1°C/1h, 10°C Hold.

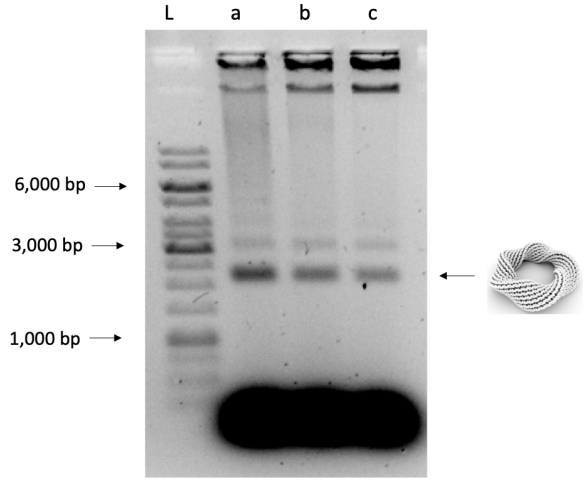


Figure S90: Gel analysis of the influence of the folding ramp on folding quality of the Tore 5 with 18 $MgCl_2$. The foldings were analyzed by agarose gel electrophoresis (1%). L: 1kb DNA ladder; a: 65°C during 15 min, 60°C to 40°C -1°C/2minutes, 10°C Hold; b: 65°C during 15 min, 60°C to 40°C -1°C/5minutes, 10°C Hold; c: 65°C during 15 min, 60°C to 40°C -1°C/10minutes, 10°C Hold.

To improve the folding's yield, we tested different concentrations of scaffold and staples oligonucleotides. Agarose gel electrophoresis analysis showed that while we still had a well defined monomeric band with 5 nM of scaffold, we had less aggregates in the well, indicating a better yield of the origami at this scaffold concentration. These results were especially observed with a folding ramp over a 3.5 hours period rather than with one over 33 hours (fig. S91).

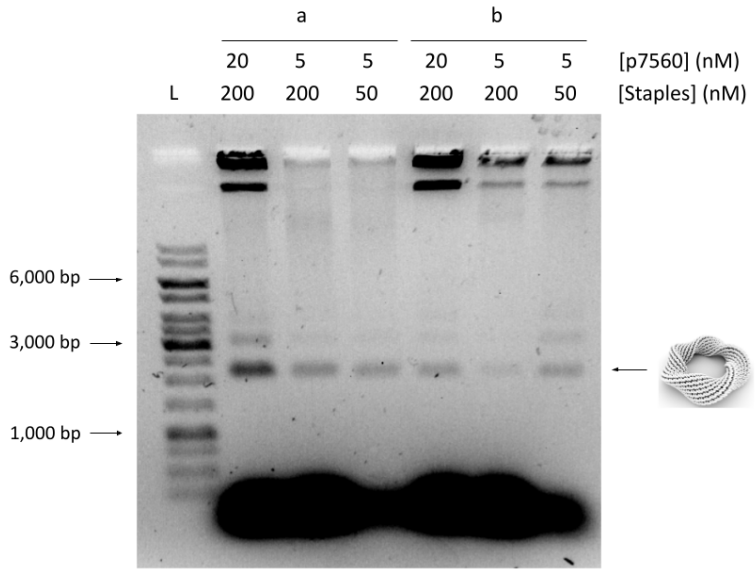


Figure S91: Gel analysis of the influence of scaffold M13 7560 and staples concentration on folding quality of the Tore 5. The foldings were analyzed by agarose gel electrophoresis (1%).. L: 1kb DNA ladder; a: 65°C during 15 min, 60°C to 40°C -1°C/10minutes, 10°C Hold; b: 65°C during 15 min, 65°C to 55°C -1°C/10minutes, 55°C to 25°C -1°C/1h, 25°C Hold.

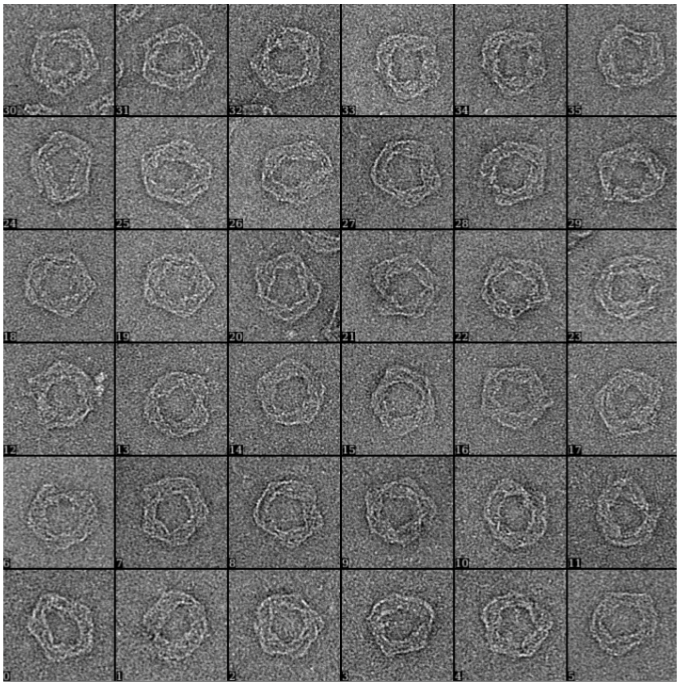

Figure S92: Transmission Electron Microscope (TEM) micrographs of typical particules of the Tore 5. Each box is 99 nm x 99 nm.

# S5 Double-sphere, Figures S93 to S100

## S5.1 Double-sphere DS design

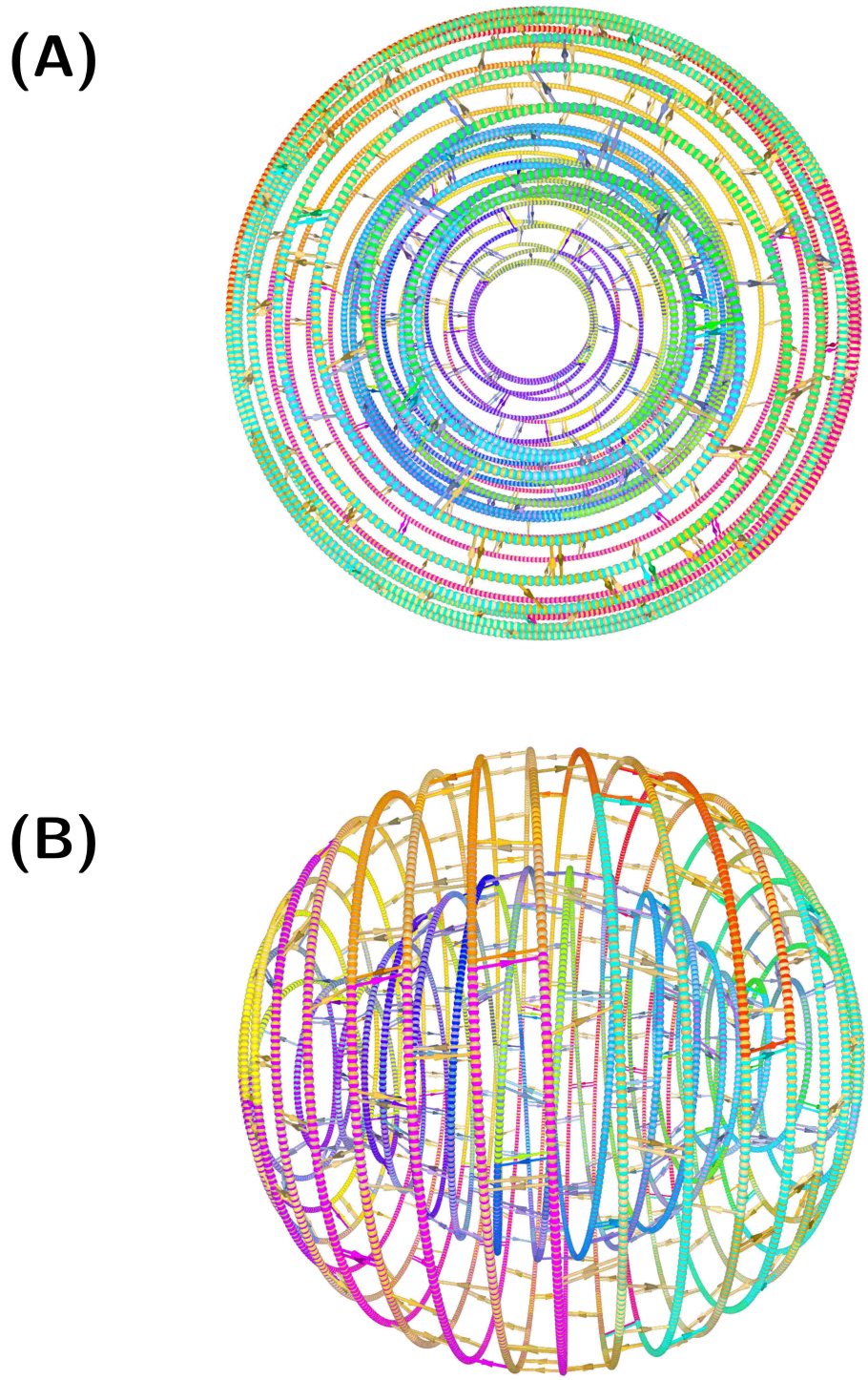


Figure S93: 3D view of the DS design, line representation. A: Front view ; B: side view. Each line represents a double helix of DNA. Transversal bars represent crossovers.

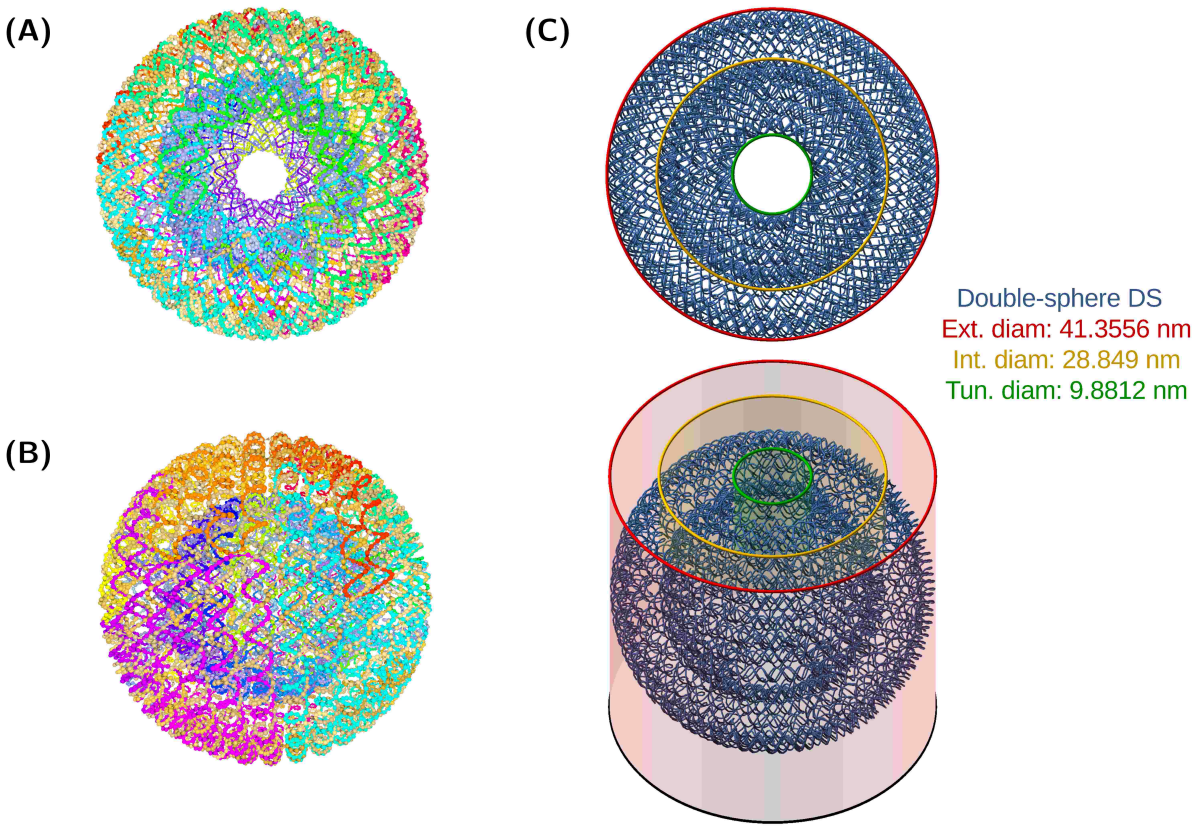


Figure S94: 3D view of the DS design, helix representation. A: Front view ; B: side view. Each ball represents a deoxynucleotide ; C: Dimensions of the DS origami. Front view (up), side view (bottom). External diameter of 41 nm (red circle), internal diameter of 29 nm (yellow circle), tunnel diameter of 10 nm (green circle).

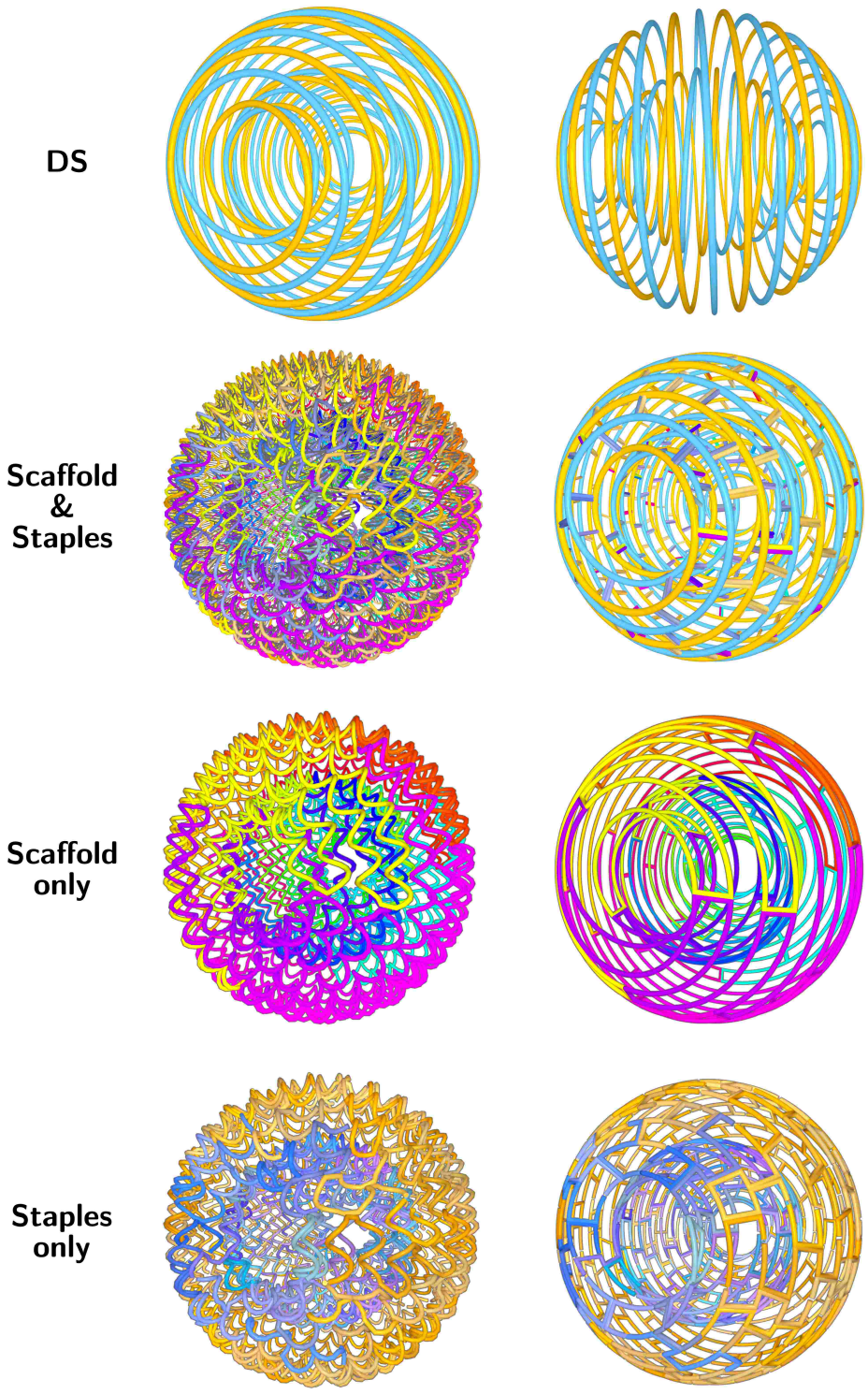


Figure S95: 3D view of the DS design, helix (left) and line (right) representations. Views of the two spirals (top), the scaffold and staples together (middle up), the scaffold (middle down) and the staples (bottom). Transversal bars on the line representation represents a crossover.

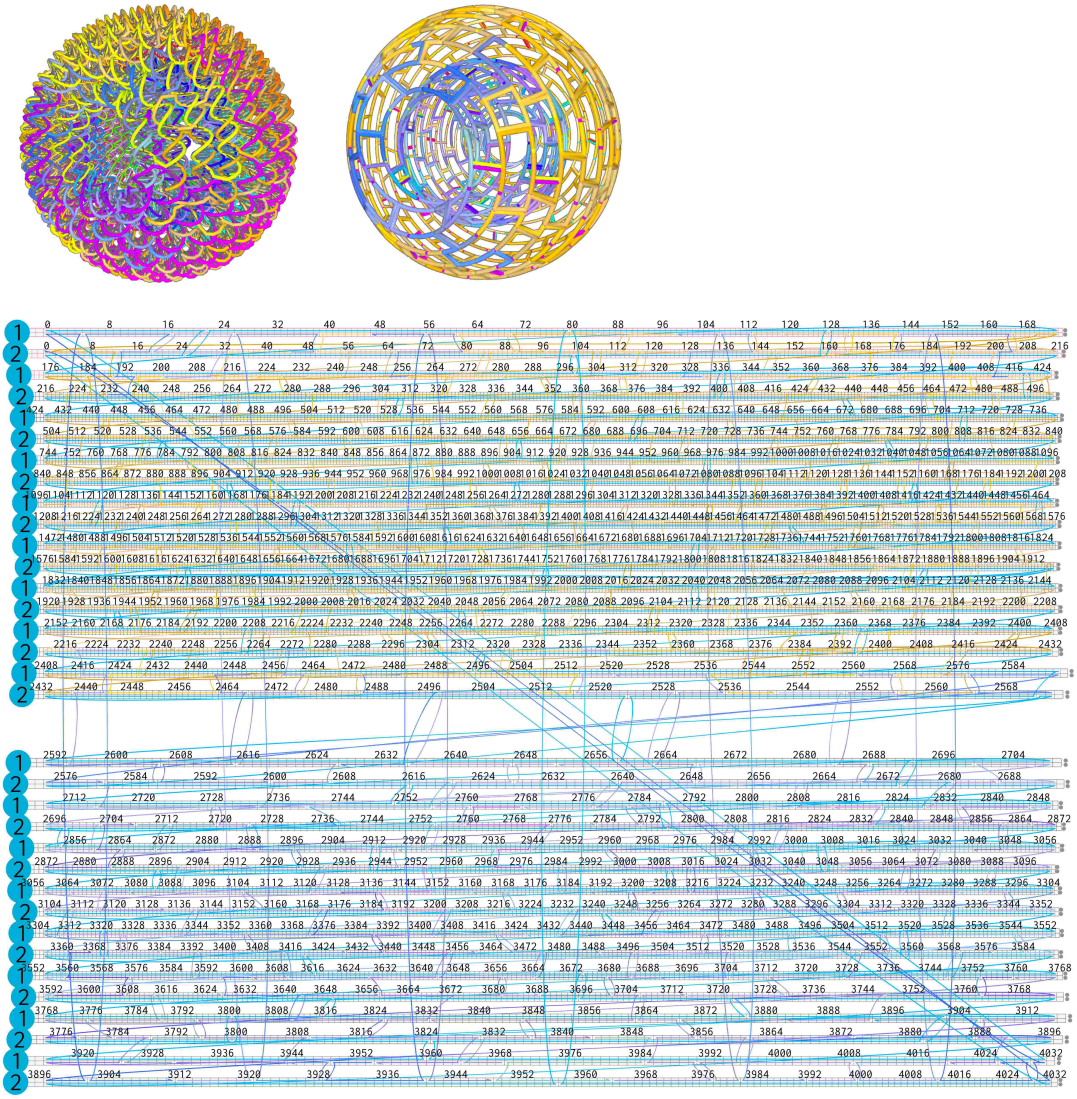

Figure S96: 2D view of the DS design. Scaffold and staples.

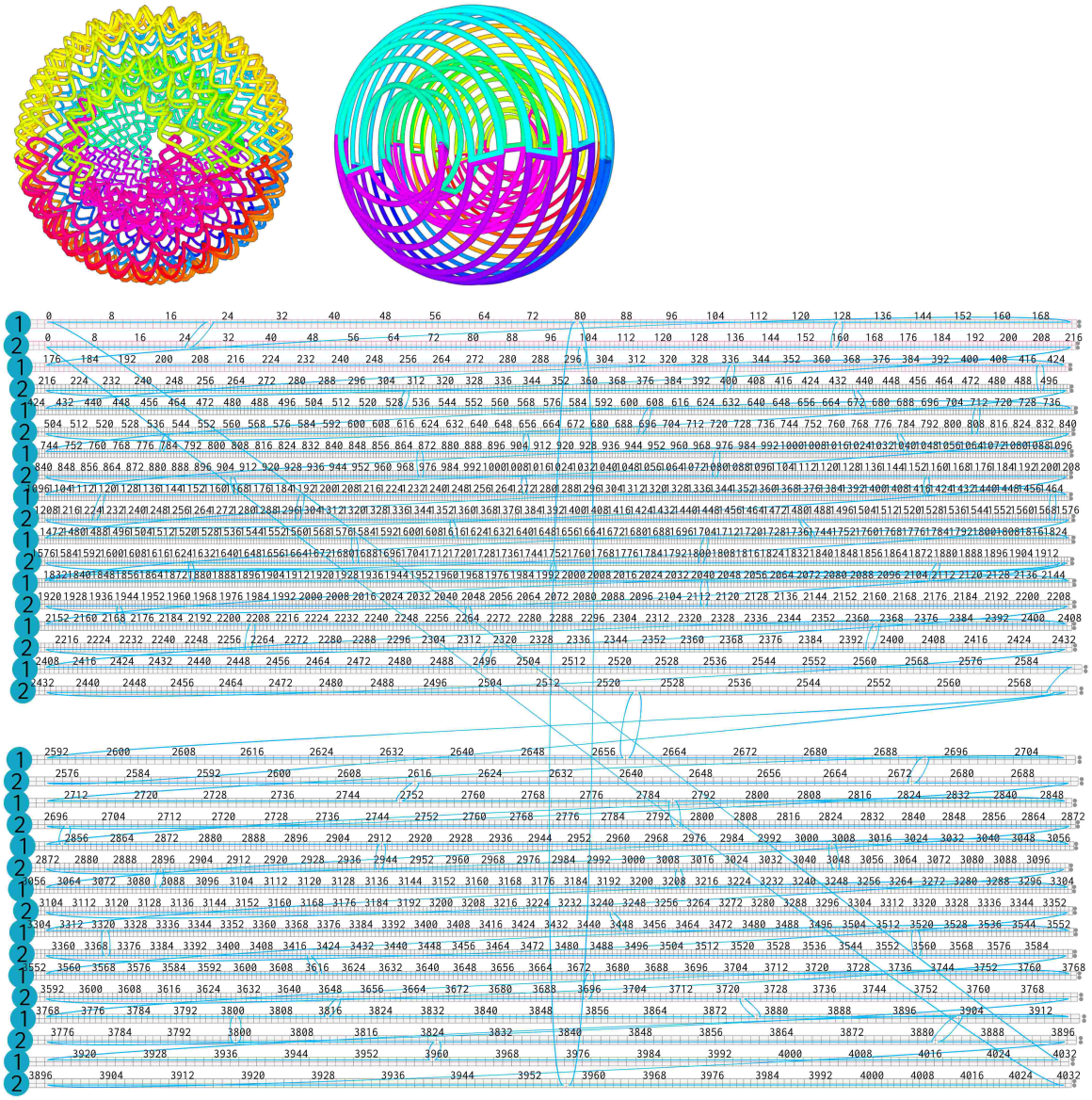

Figure S97: 2D view of the DS design. Scaffold only.

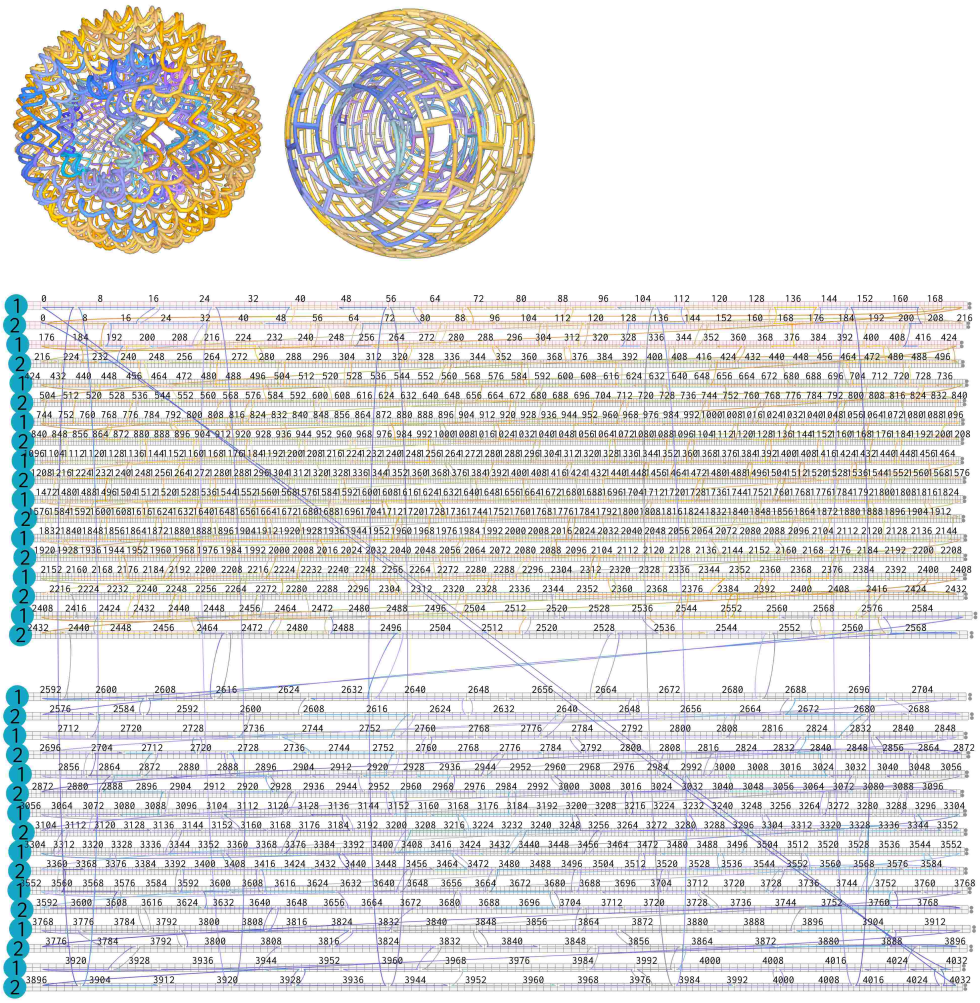

Figure S98: 2D view of the DS design. Staples only.

## S5.2 Double-sphere DS experimental validation

**Optimization of the folding conditions of the DS origami (fig. S99)** Three different folding ramps and three different magnesium concentrations were tested and analyzed by agarose gel electrophoresis to optimize the folding conditions. This analysis revealed a brighter monomeric band when the origami was folded over a long period of time (65°C during 15 min, 60°C to 20°C -1°C/2h, 10°C Hold, fig. S99) rather than over shorter folding ramps.

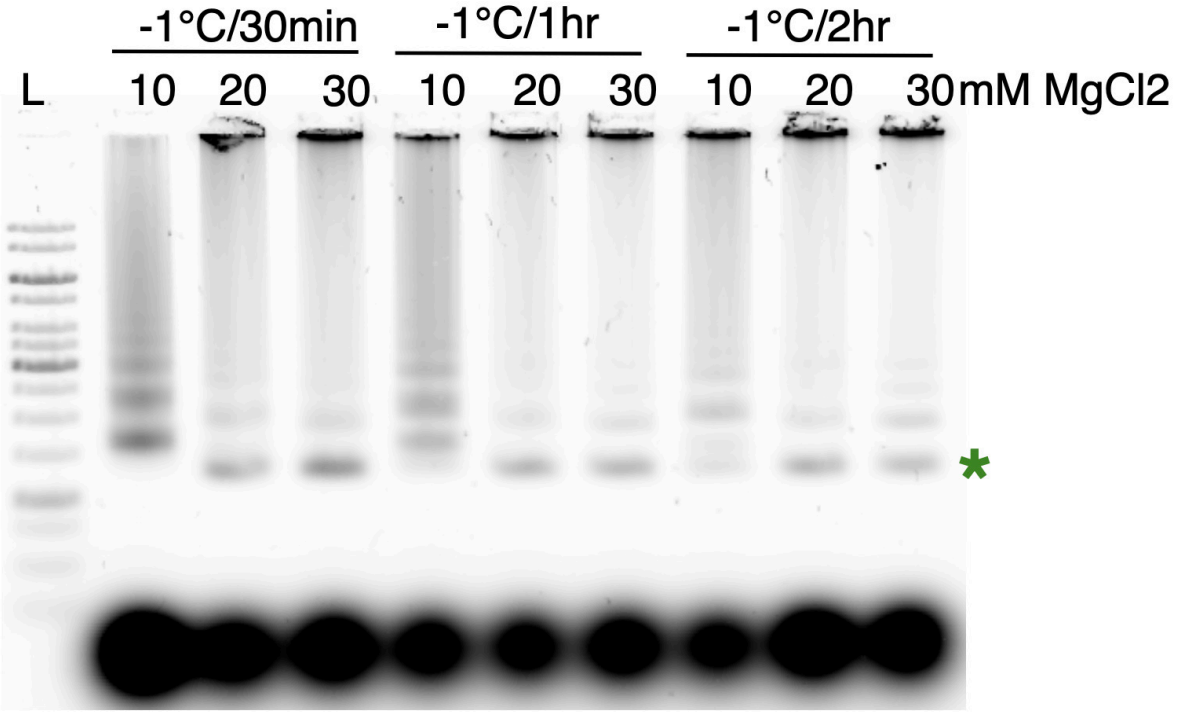


Figure S99: Gel analysis of the influence of $MgCl_2$ concentration on folding quality of the DS. The foldings were analyzed by agarose gel electrophoresis (1%). L: 1kb DNA ladder. 65°C during 15 min, 60°C to 20°C -1°C/30min, 10°C Hold ; 65°C during 15 min, 60°C to 20°C -1°C/1h, 10°C Hold ; 65°C during 15 min, 60°C to 20°C -1°C/2h, 10°C Hold.

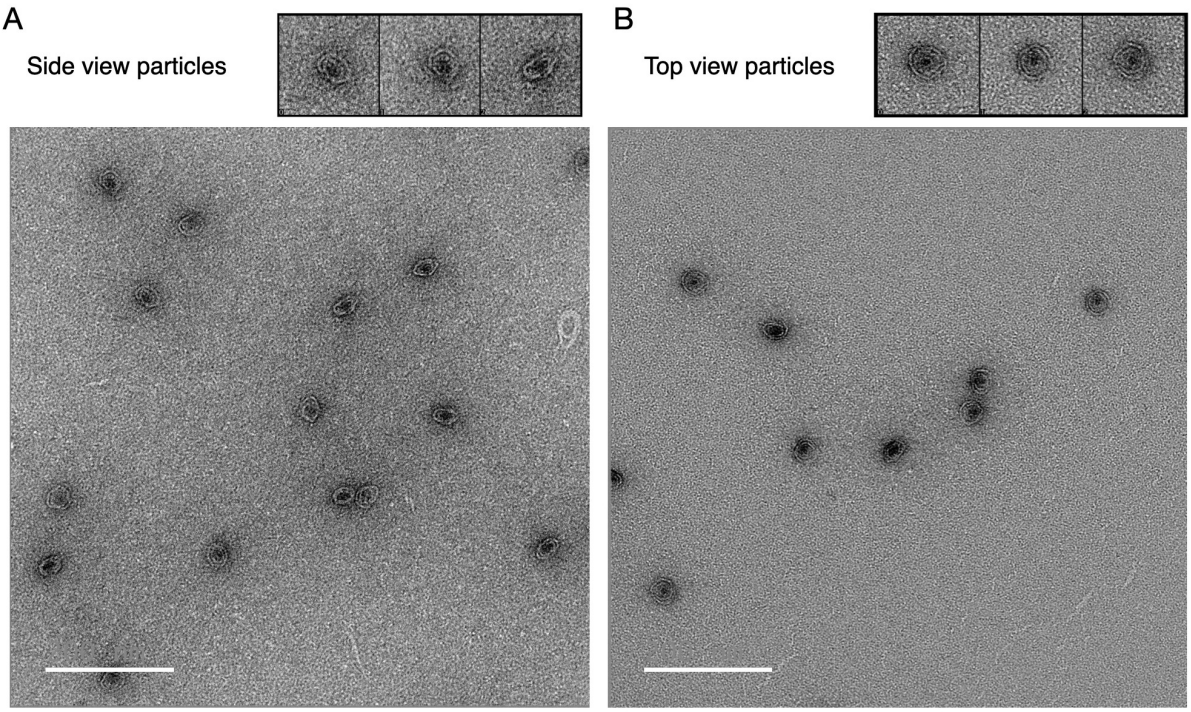


Figure S100: Transmission Electron Microscope (TEM) micrographs of typical particules of the DS. A: Selected side view particles. B: Selected Top view particles. Scale bar = 200 nm.

# S6 Vault-like origami, Figures S101 to S112

## S6.1 Vault-like origami design

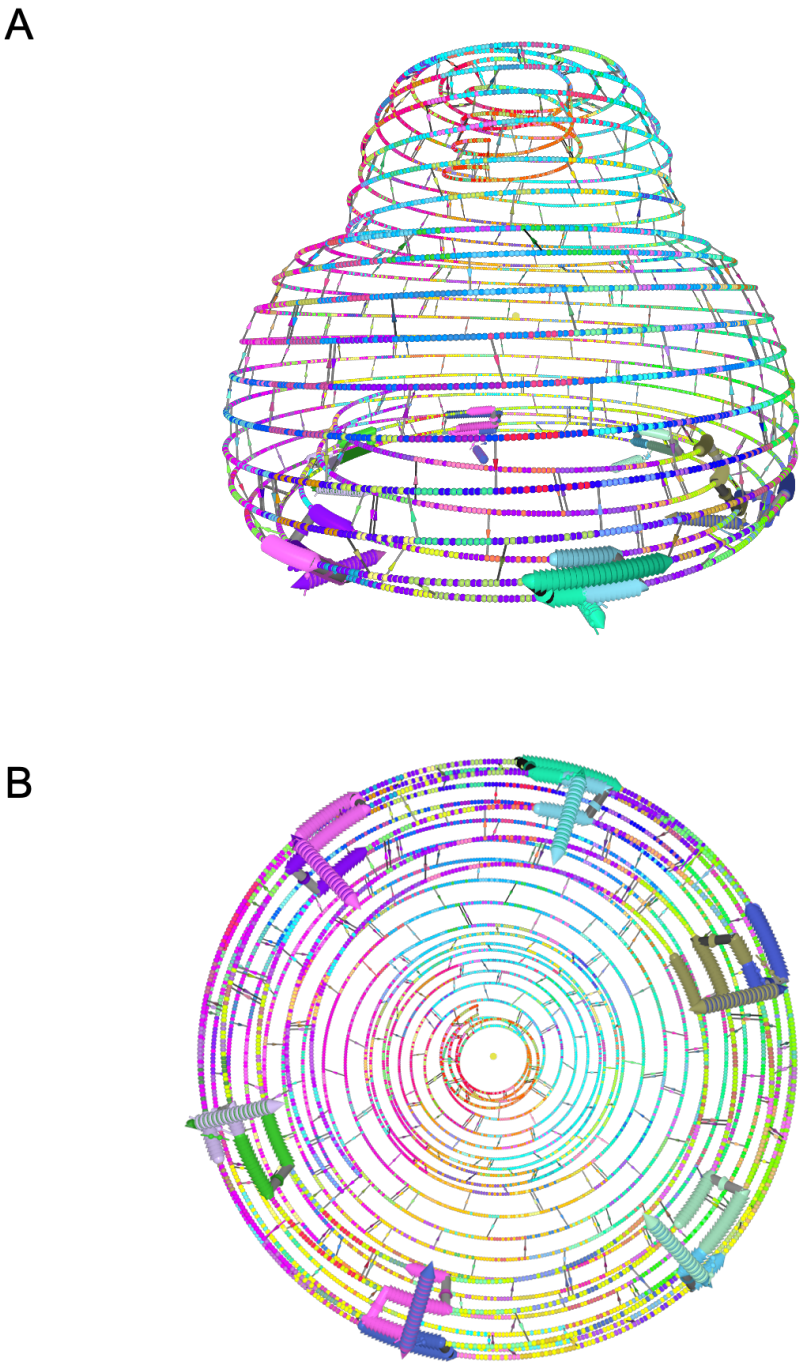


Figure S101: 3D view of the Vault-like design, line representation. A: Front view; B: Bottom view. Each line represents a double helix of DNA. Transversal bars represent crossovers. Bold lines represent the anchor staples (6 pairs) used to enable the homodimerization.

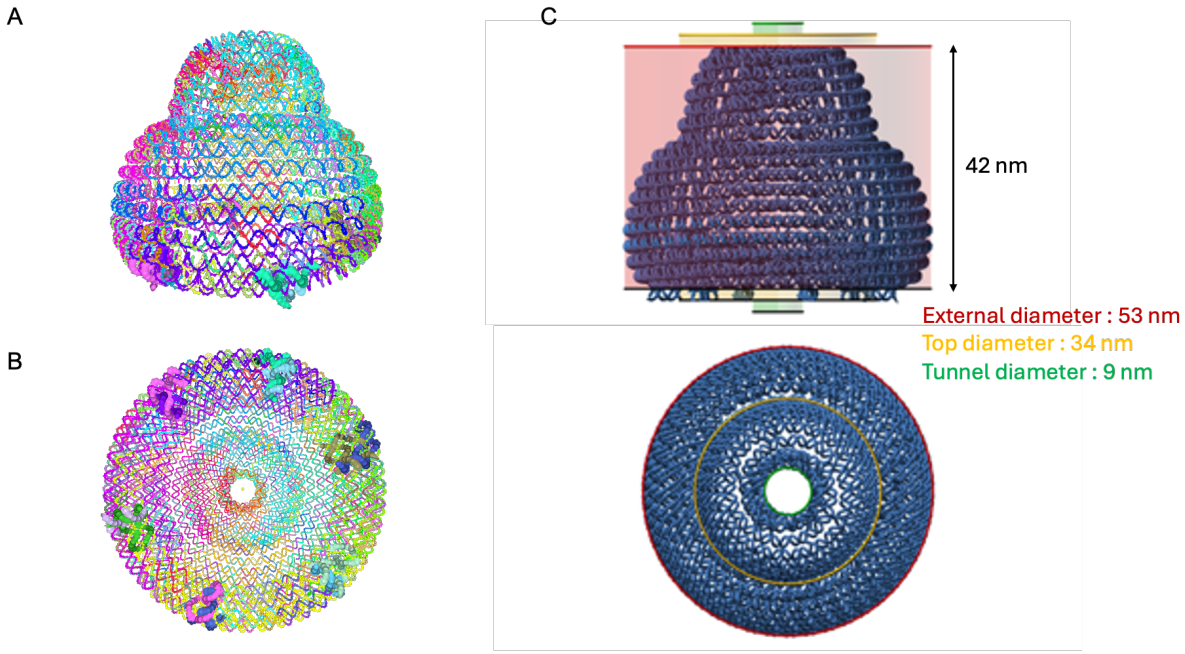


Figure S102: 3D view of the Vault-like design, helix representation. A: Front view; B: Bottom view. Each ball represents a deoxynucleotide. Bold part of the helices represent the anchor staples (6 pairs) used to enable the homodimerization; C: Dimensions of the Vault-like origami. Front view (up), bottom view (bottom). External diameter of 53 nm (red circle), top diameter of 34 nm (yellow circle), tunnel diameter of 9 nm (green circle), height of 42 nm.

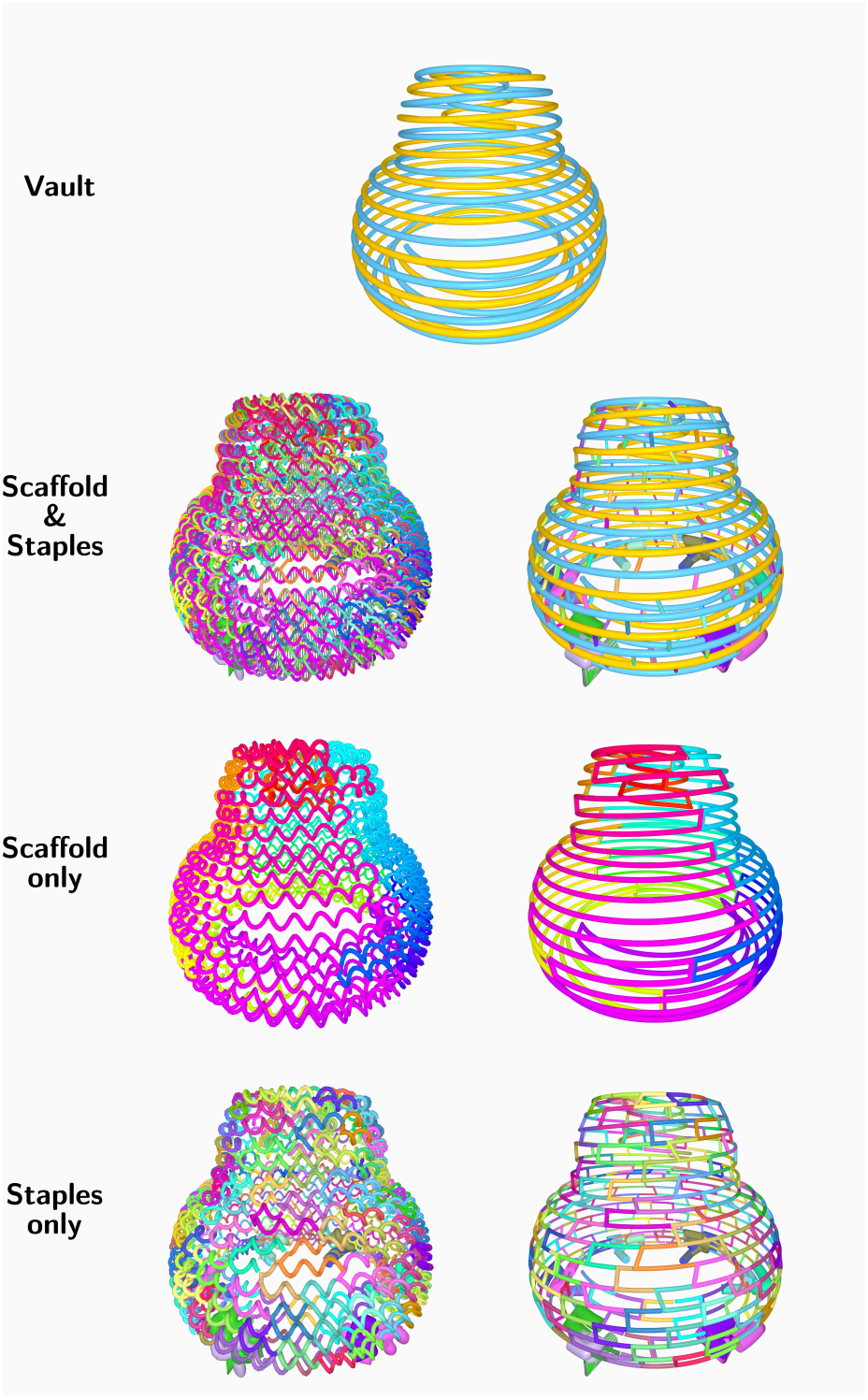


Figure S103: 3D view of the Vault-like design, helix (left) and line (right) representations. Views of the two spirals (top), the scaffold and staples together (middle up), the scaffold (middle down) and the staples (bottom). Transversal bars on the line representation represents a crossover. Bold strands represent the anchor staples (6 pairs) used to enable the homodimerization.

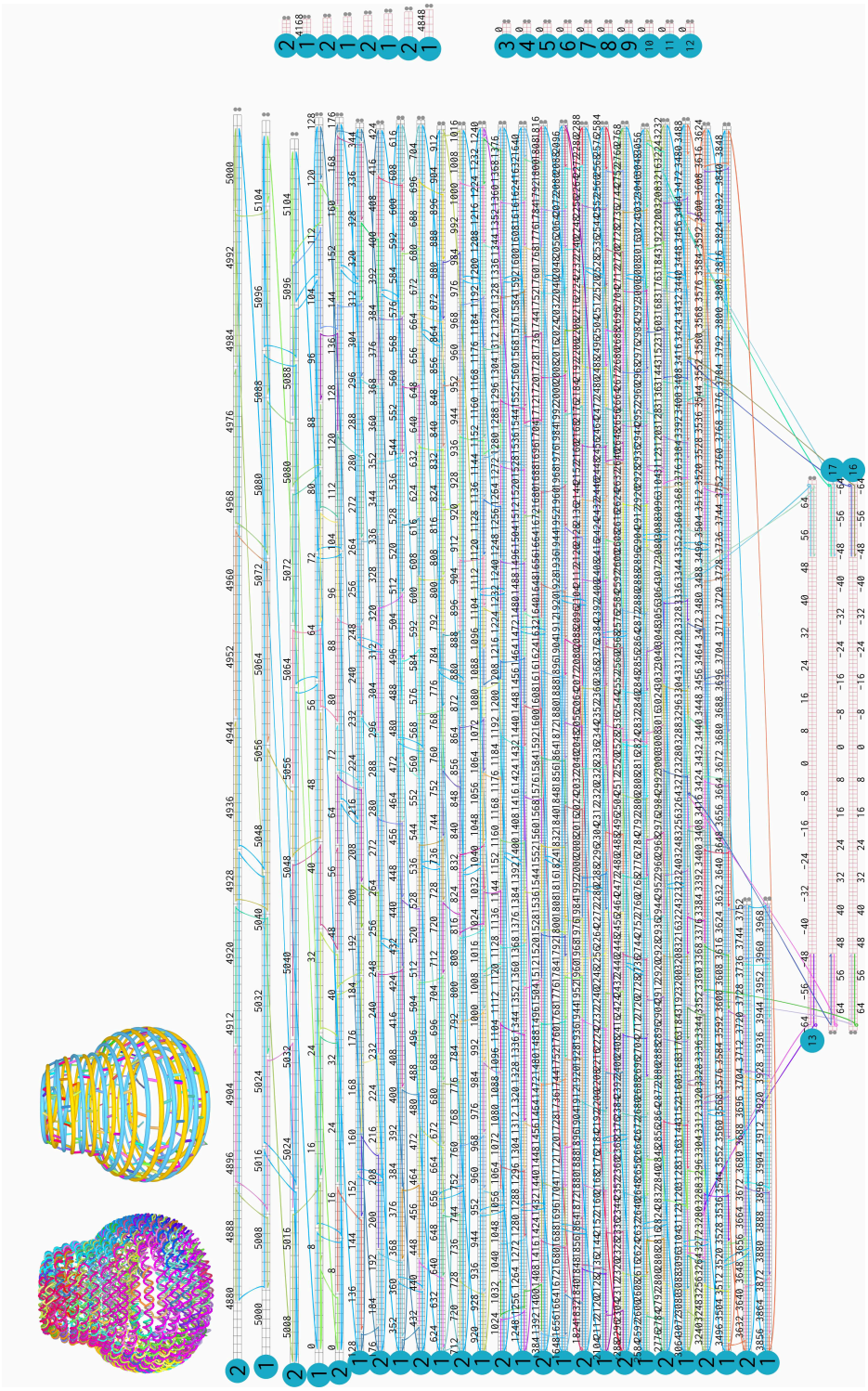

Figure S104: 2D view of the Vault-like design. Scaffold and staples.

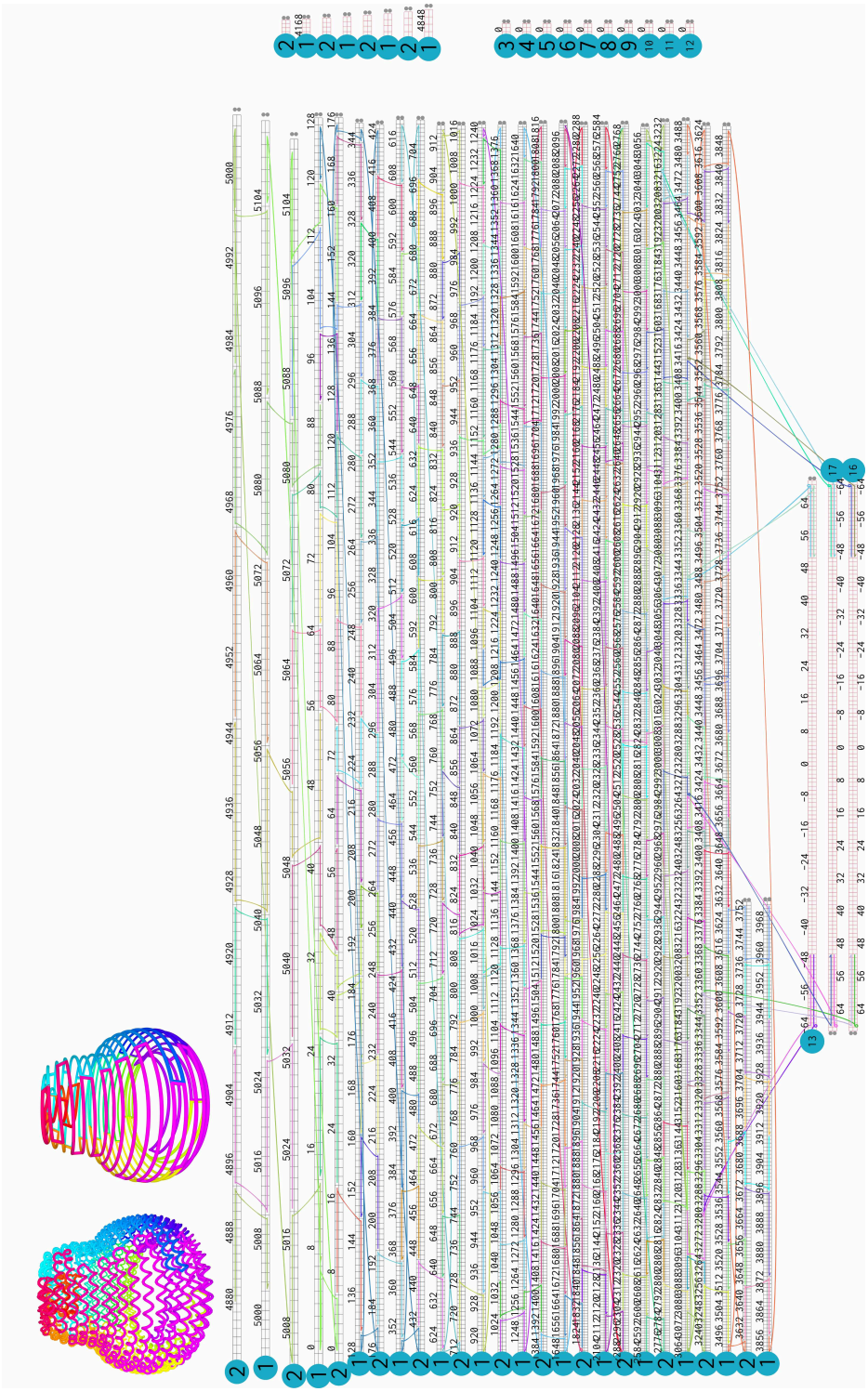

Figure S105: 2D view of the Vault-like design. Scaffold only.

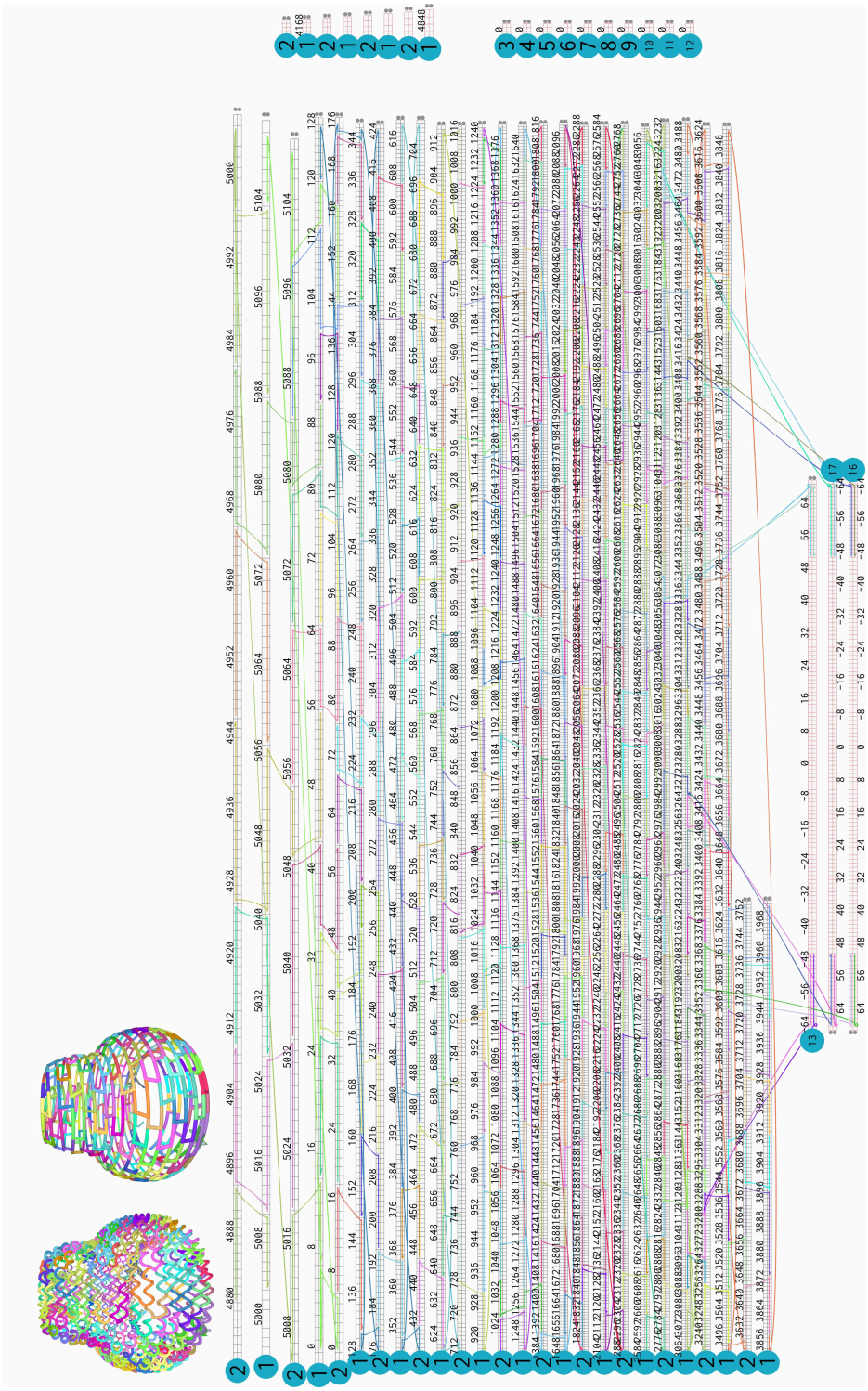

Figure S106: 2D view of the Vault-like design. Staples only.

## S6.2 Vault-like origami experimental validation

**Optimization of the folding conditions of the** Vault **origami (figs. S107 to S112)** Three different folding ramps (over 3.5 hours, 33 hours and 42 hours) were first tested and analyzed by agarose gel electrophoresis, with six different magnesium concentrations (10 to 20 mM) and a scaffold concentration of 20 nM with staples oligonucleotides in a 10-fold excess (fig. S107). The gel showed that the yield was better with higher magnesium concentrations and longer folding ramps.

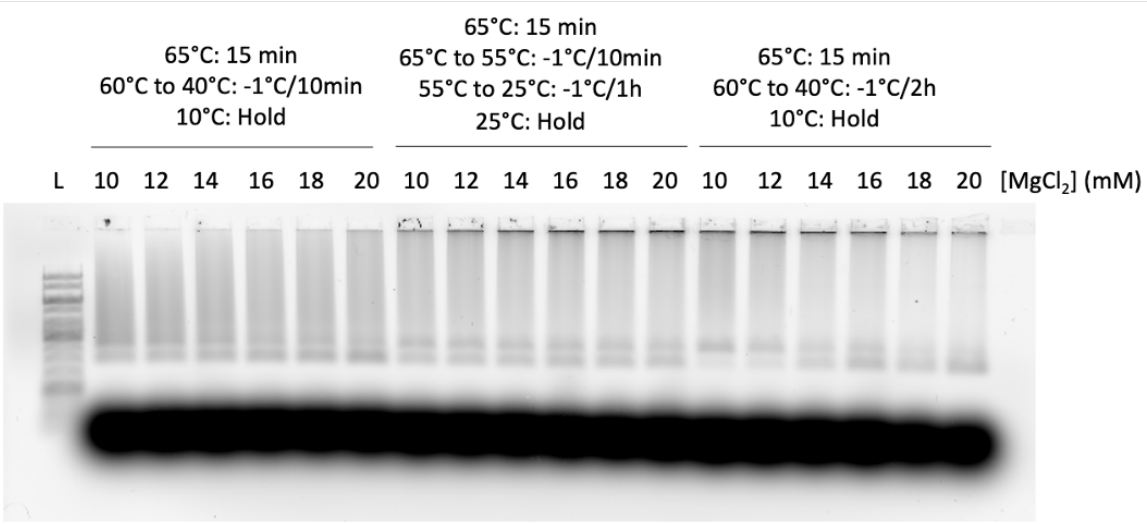


Figure S107: Gel analysis of the influence of $MgCl_2$ concentration and folding ramp on folding quality of the Vault. The foldings were analyzed by agarose gel electrophoresis (1%). L: 1kb DNA ladder.

We then folded the vault with 20 mM of magnesium over a 63-hour time period and compared it to the foldings of the vault over a 42-hour and over a 3.5-hour time period thanks to agarose gel electrophoresis (fig. S108). For all the conditions, we observed a monomeric lower band, with a better yield with the longest folding ramp (63 hours).

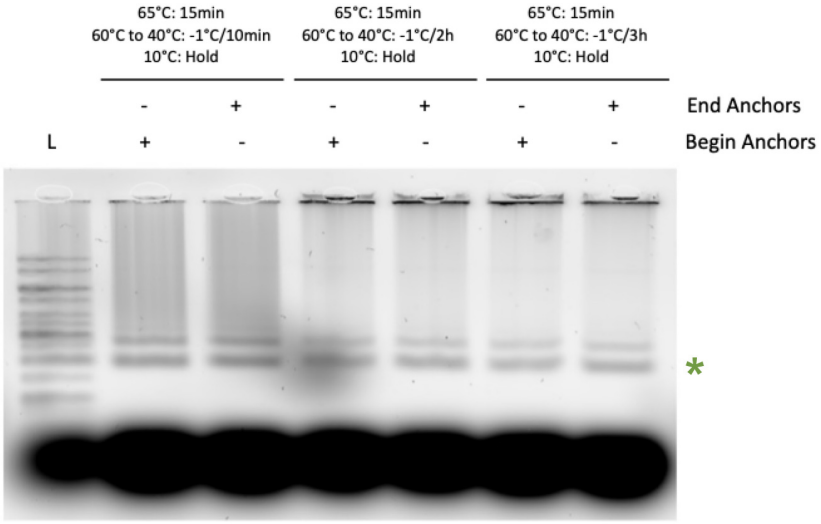


Figure S108: Gel analysis of the influence of different folding ramps on the folding quality of the Vault. For each folding ramp, the two versions of the Vault monomer (with 5'-anchors: "Begin Anchors" and with 3'-anchors: "End Anchors") designed to enable the dimerization were folded. The foldings were analyzed by agarose gel electrophoresis (1%). L: 1kb DNA ladder.

We analyzed the purified monomers of the Vault folded with these three conditions with negative staining electron-microscopy. The micrographs, galleries and 2D-class averaging displayed anticipated shapes of the Vault-like origami even though the 3.5-hour and 42-hour long folding ramps showed monomers which looked more flattened than the ones observed with the 63-hour long folding ramp (Figure 4, fig. S109).

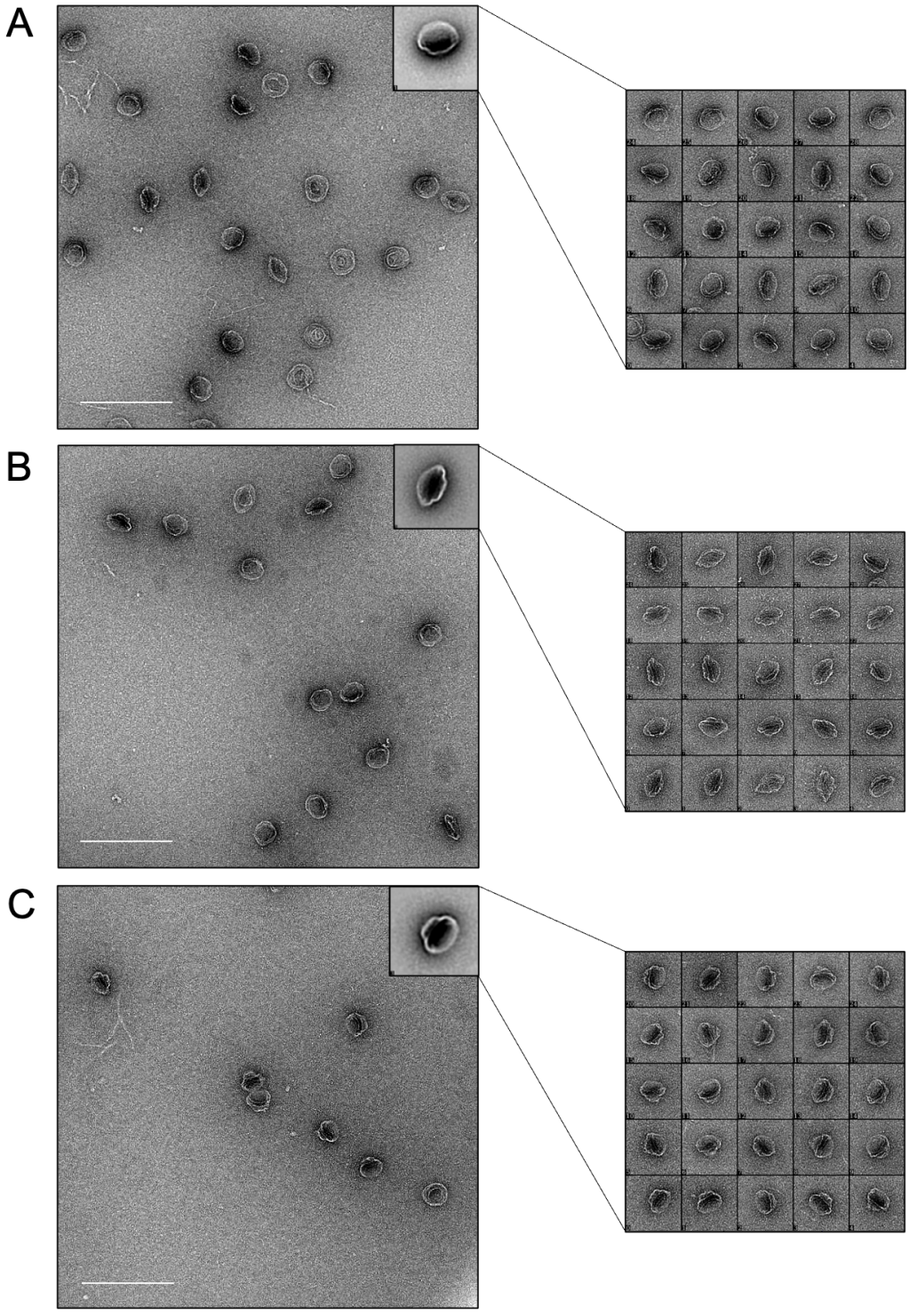


Figure S109: ns-TEM analysis of purified Vault monomers folded with different folding ramps. For each condition, one TEM micrograph, a 2D-class averaging and a gallery of typical particles observed on micrographs are depicted. A: 65°C during 15 min, 60°C to 40°C -1°C/10min, 10°C Hold; B: 65°C during 15 min, 60°C to 40°C -1°C/2h, 10°C Hold; C: 65°C during 15 min, 60°C to 40°C -1°C/3h, 10°C Hold. Scale bar = 200 nm. Box size = 112 nm x 112 nm.

After optimization of the dimerization conditions (fig. S110), we incubated the Vault monomers obtained with each of the three previously mentioned folding ramps with 100 mM magnesium at 37°C over a 15-hour time period. We then analyzed the dimers formation by agarose-gel electrophoresis (Figure 4, fig. S111) and ns-TEM (Figure 4, fig. S112).

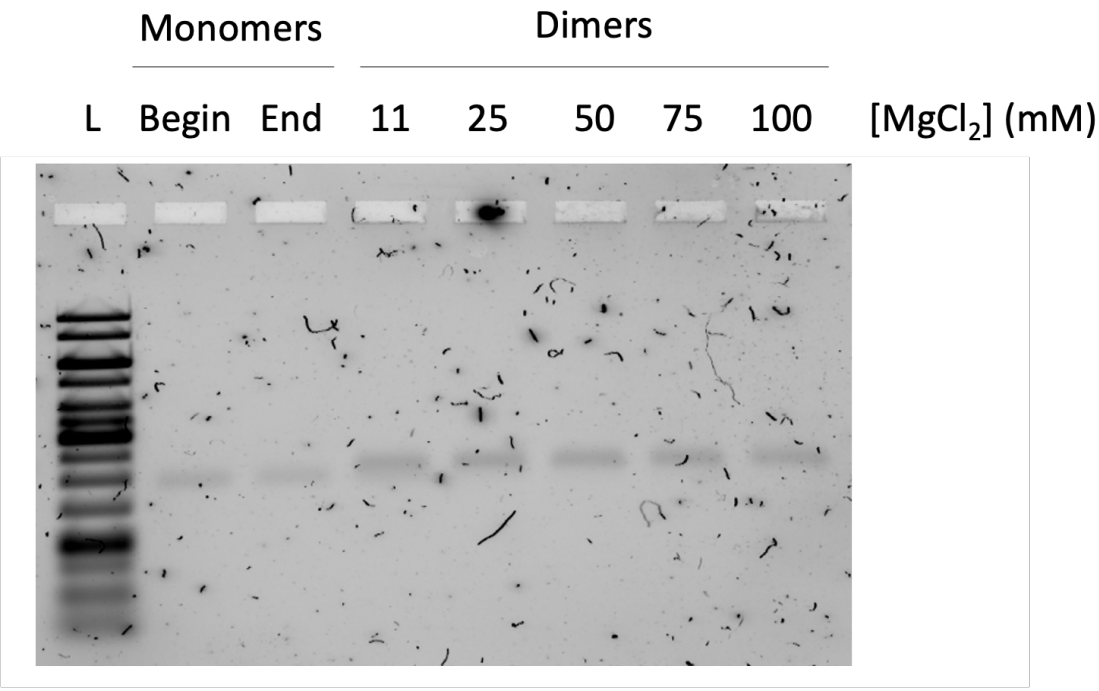


Figure S110: Gel analysis of the influence of different $MgCl_2$ concentrations on the dimerization of the vault-origami. The dimerization quality was analyzed by agarose gel electrophoresis (1%). The monomers "Begin" and "End" correspond to the vault monomers with 5'-anchors and 3'-anchors respectively, after a 42-hour folding and gel purification. L: 1kb DNA ladder. The monomers "Begin" and "End" were incubated with different $MgCl_2$ concentrations over a 15-hour time period at 37°C to enable dimerization. We observe retarded bands for the dimers compared to the monomers, suggesting some oligomerization (possibly dimerization). At 100 mM $MgCl_2$, we observe a slightly retarded band compared to the other ones, suggesting a better dimerization of the monomers.

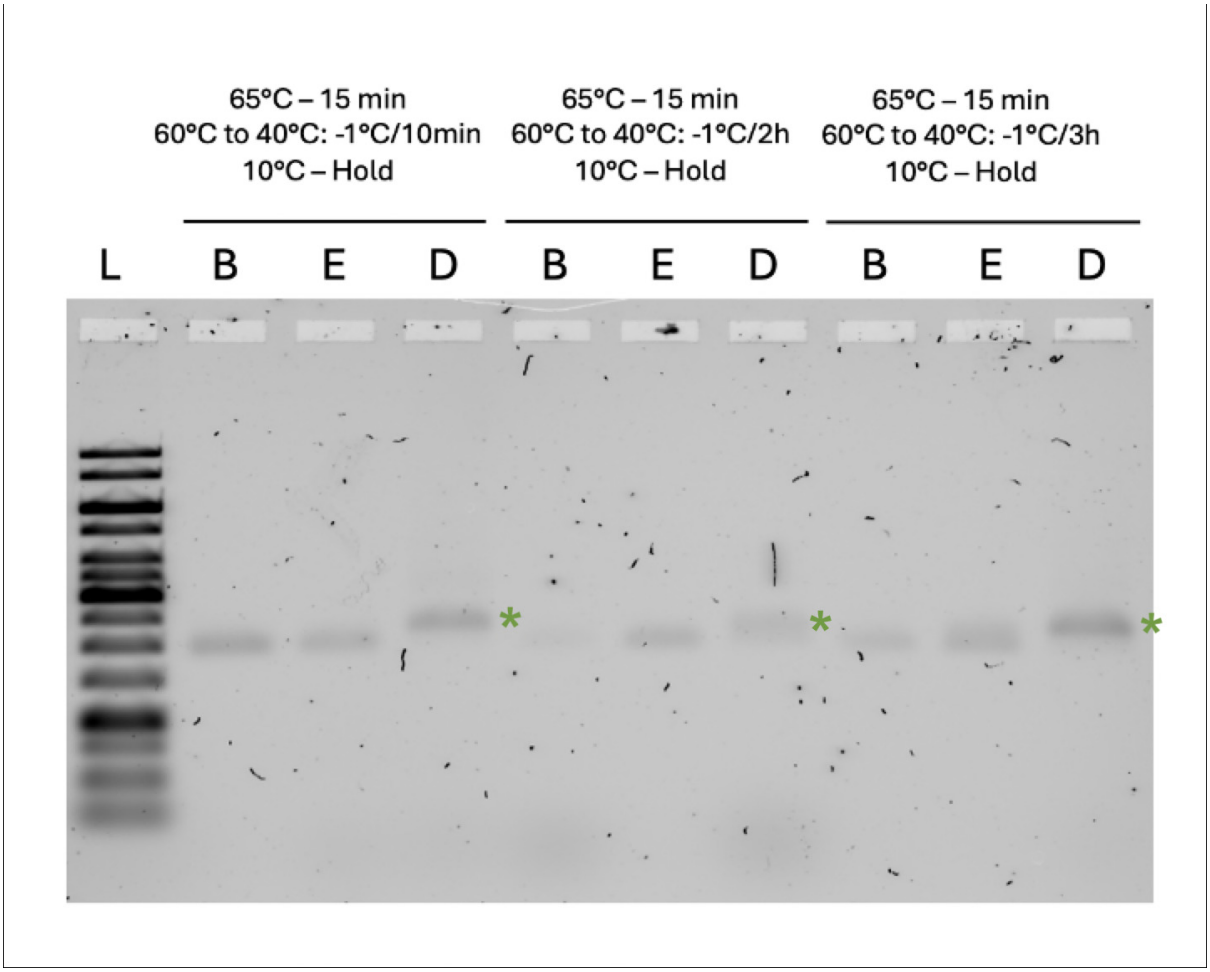


Figure S111: Gel analysis of the influence of the folding ramp of the vault monomers on their dimerization. The dimerization quality was analyzed by agarose gel electrophoresis (1%). B: purified vault monomers with 5'-anchors; E: purified vault monomers with 3'-anchors; D: obtained dimer by incubating B and E with 100 mM $MgCl_2$ over a 15-hour time period at 37°C; L: 1kb DNA ladder. We observe that for all the folding ramps used to fold the monomers, retarded bands were observed after incubation of the monomers together (D), suggesting some oligomerization (possibly dimerization).

The observed dimers formed from monomers folded over a 63-hour time period appeared to be longer than the ones formed from monomers folded with the two other folding ramps (fig. S112).

Hence, we concluded that the optimal folding ramp for the folding of the vault origami was the 63-hour long folding ramp.

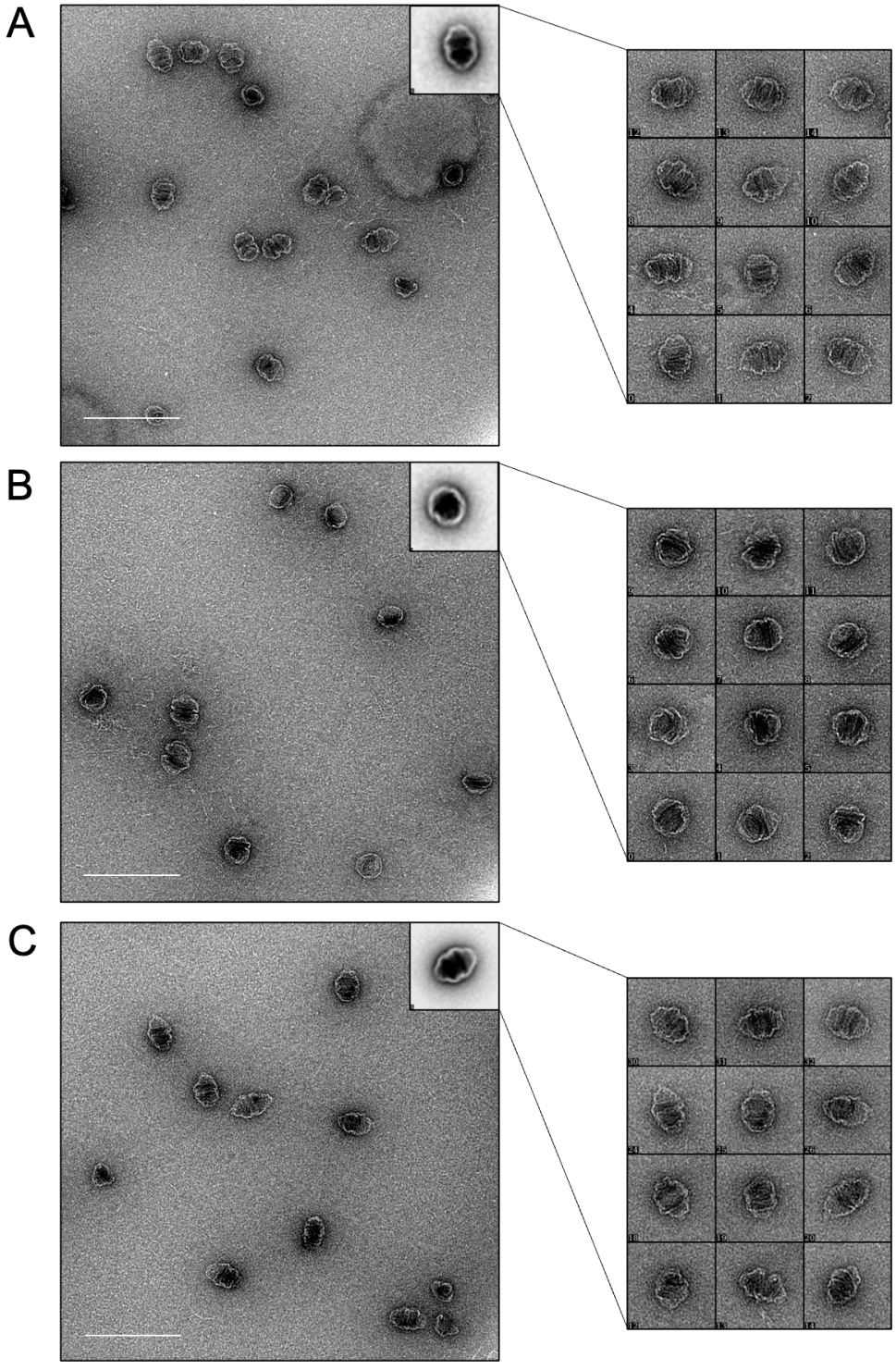


Figure S112: ns-TEM analysis of purified Vault dimers obtained from vault monomers folded with different folding ramps. For each condition, one TEM micrograph, a 2D-class averaging and a gallery of typical particles observed on micrographs are depicted. A: 65°C during 15 min, 60°C to 40°C -1°C/10min, 10°C Hold; B: 65°C during 15 min, 60°C to 40°C -1°C/2h, 10°C Hold; C: 65°C during 15 min, 60°C to 40°C -1°C/3h, 10°C Hold. Scale bar = 200 nm. Box size = 132 nm x 132 nm.

# S7 Summary of all the designs, Figure S113

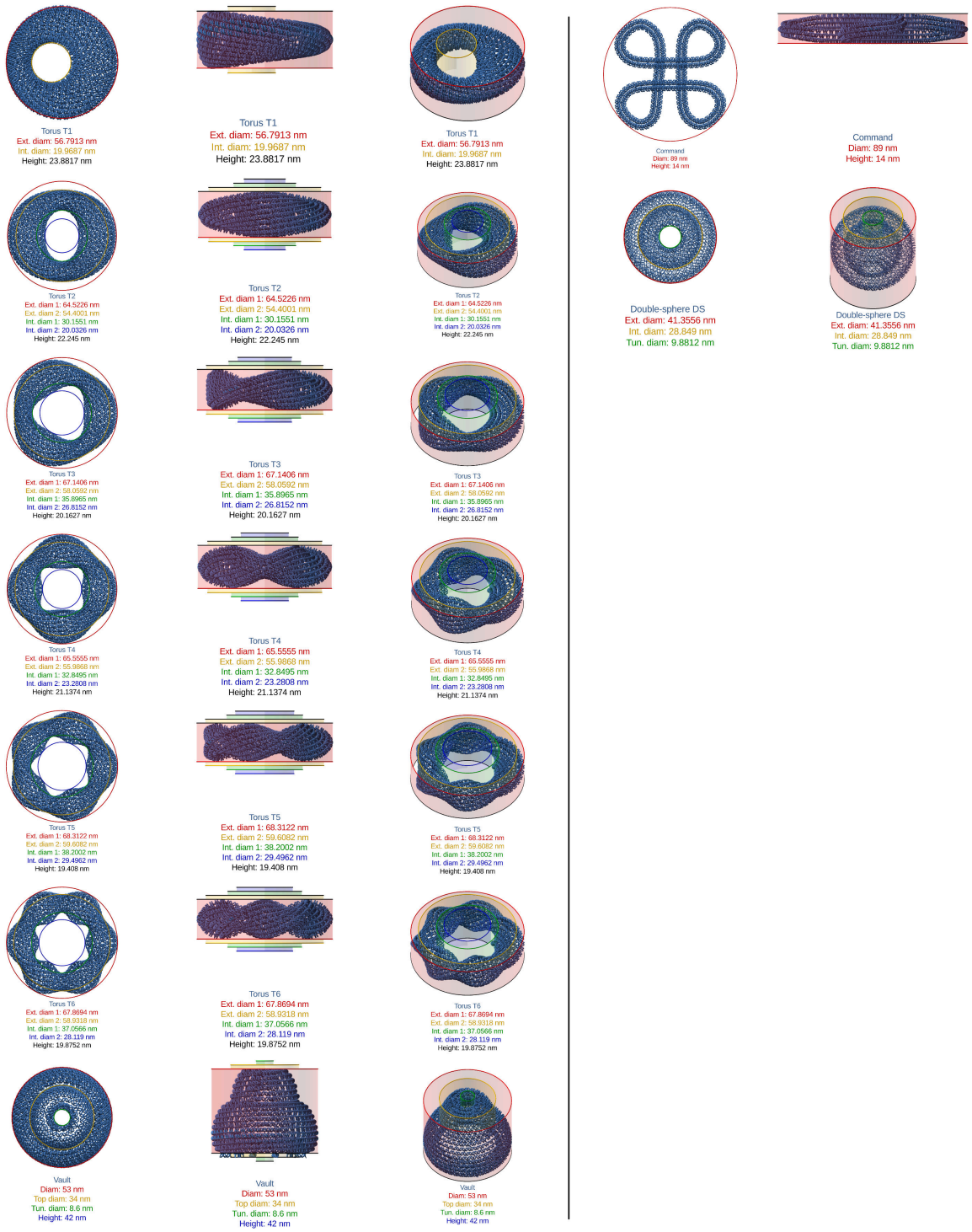


Figure S113: All the designs and their expected sizes

# S8 Distribution of staple strand crossover interdistances, Figures S114 to S121

Figures S114 to S121 show the distribution of staple crossover interdistances for the designs ⌘, T2, T3, T4, T5, T6, DS, and a classic flat square design. The colors of the bars indicate the average curvature radius (main color scale: 4 nm [red] to 40 nm [blue]) and average torsion (inset color scale: 0/nm [blue] to 0.2/nm [red]) at the crossover locations. As opposed to the classic flat design, where interdistances are sharply centered at 16 and 31 nucleotides (fig. S121), the crossover interdistances in our curved and twisted designs are broadly distributed, forming three main peaks centered around 6–8, 15, and 25 nucleotides. The spike at 1 nucleotide corresponds to double crossovers.

Note that the different curvature radii and torsion values are similarly represented within the two peaks centered at 15 and 25 nucleotides across all designs. However, the peak centered at 4-6 nucleotides appears to include crossovers located at regions of smaller curvature radius (e.g., fig. S120). This observation may serve as a design guideline: regions with smaller curvature radii may require more closely spaced crossovers.

Finally, these graphs suggest that accommodating curvature and torsion requires a broader distribution of crossover interdistances—an outcome made possible by our spiral design paradigm. Moreover, no apparent patterns emerge, as no correlation with either curvature radius or torsion is observed. This supports the conclusion that rule-based patterning is likely insufficient and underscores the value of our algorithmic 3D nucleotide positioning strategy for accurate crossover placement.

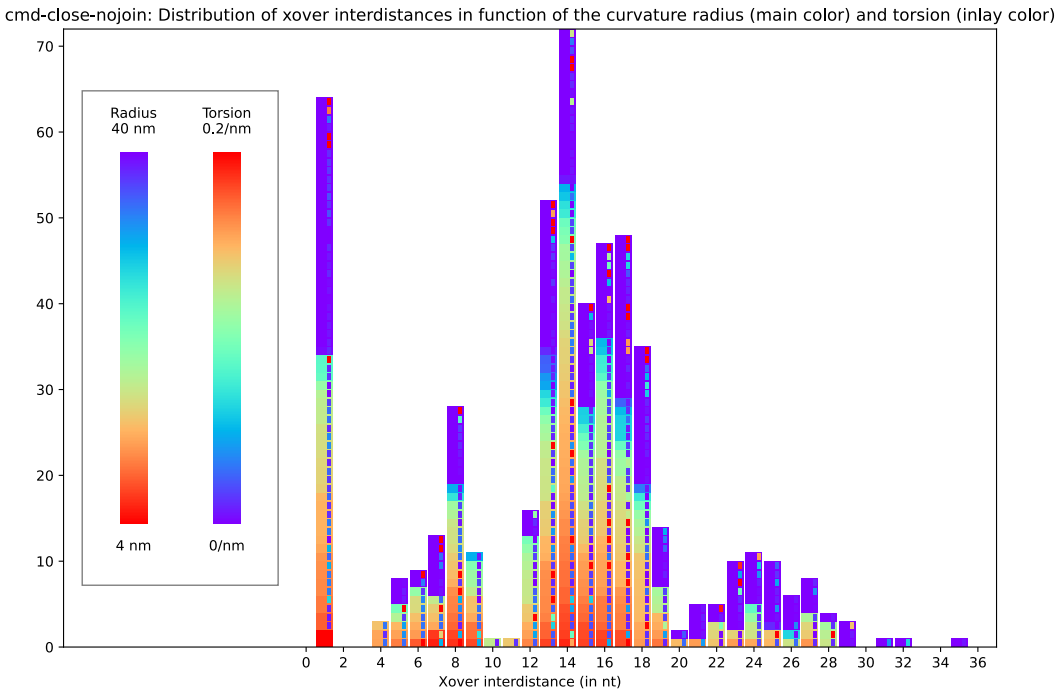


Figure S114: Distribution of staple strand crossover interdistances correlated (in colors) with local curvature radius and torsion in the ⌘-origami.

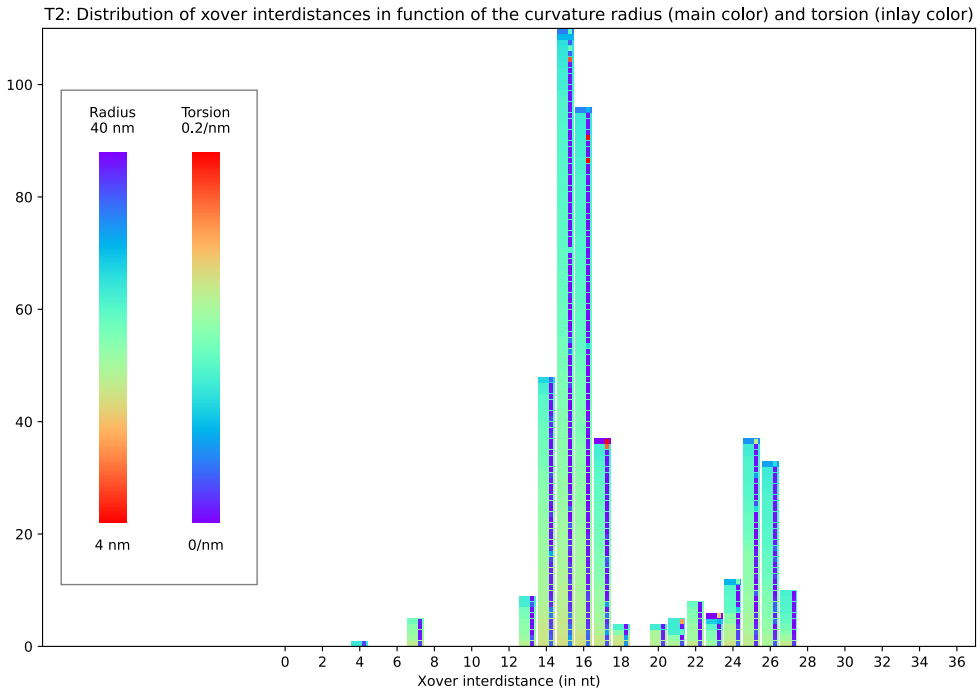


Figure S115: Distribution of staple strand crossover interdistances correlated (in colors) with local curvature radius and torsion in the T2-origami.

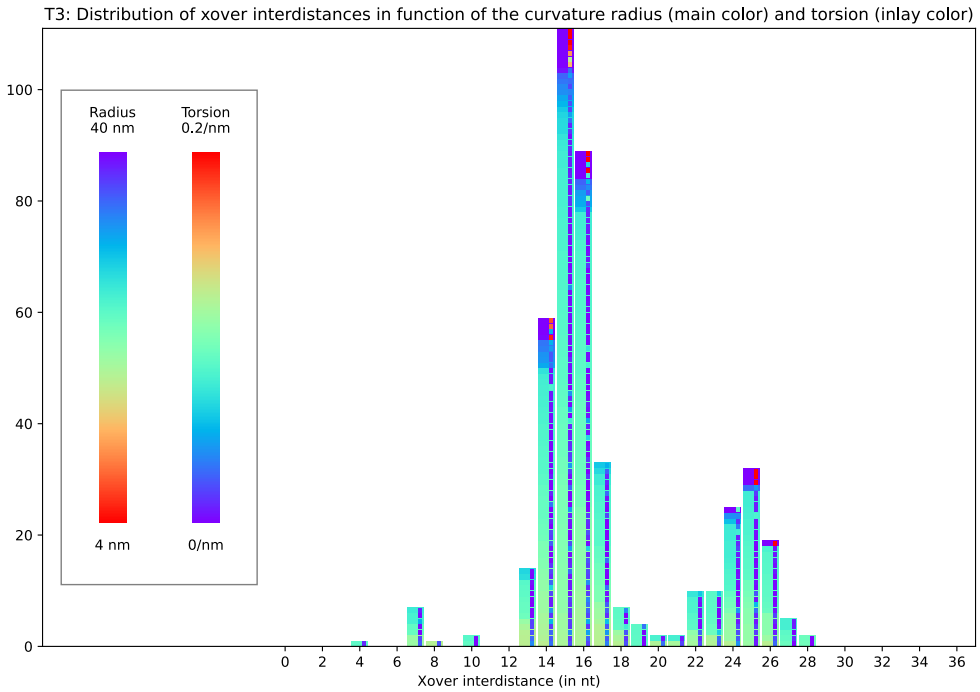


Figure S116: Distribution of staple strand crossover interdistances correlated (in colors) with local curvature radius and torsion in the T3-origami.

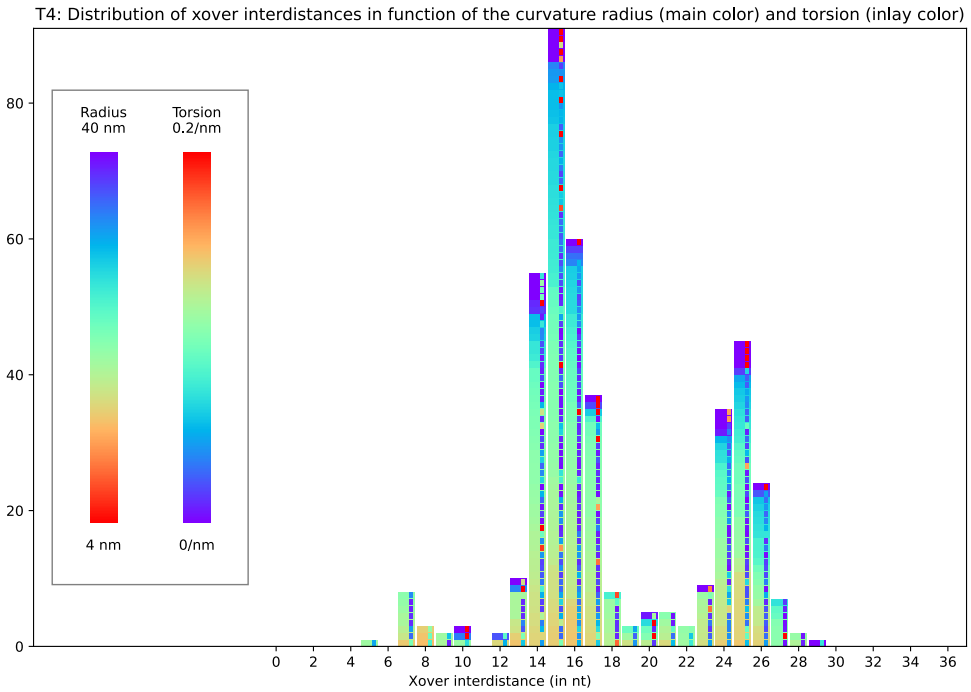


Figure S117: Distribution of staple strand crossover interdistances in the T4-origami.

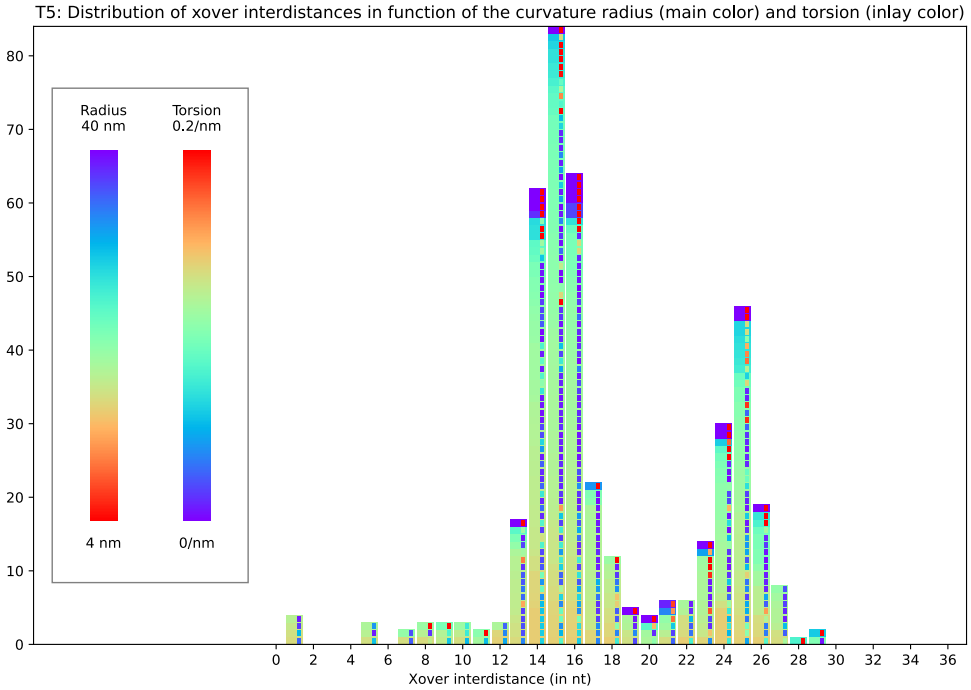


Figure S118: Distribution of staple strand crossover interdistances in the T5-origami.

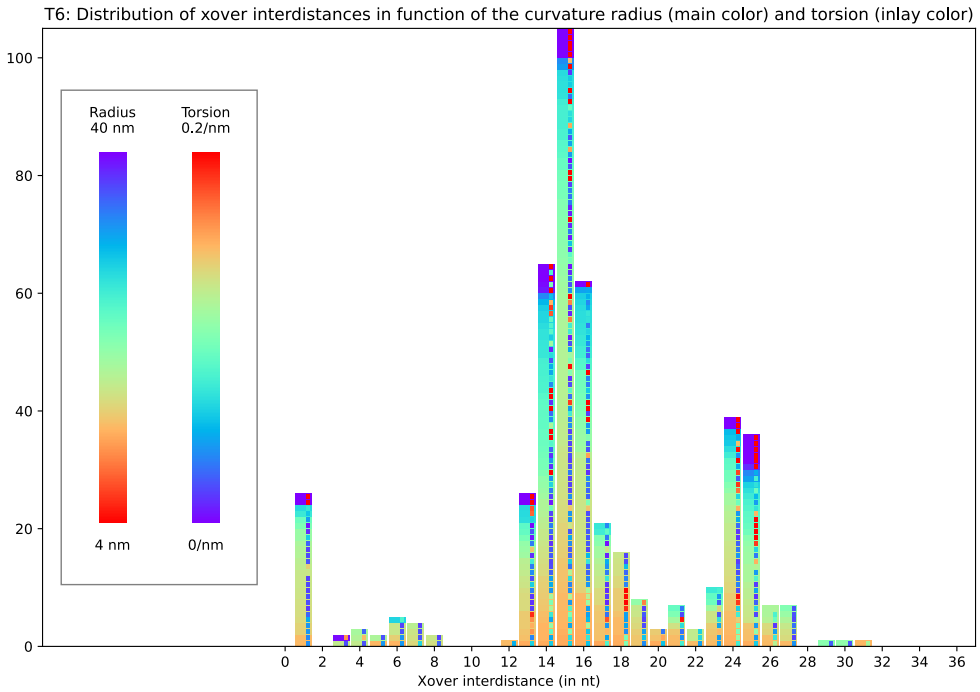


Figure S119: Distribution of staple strand crossover interdistances correlated (in colors) with local curvature radius and torsion in the T6-origami.

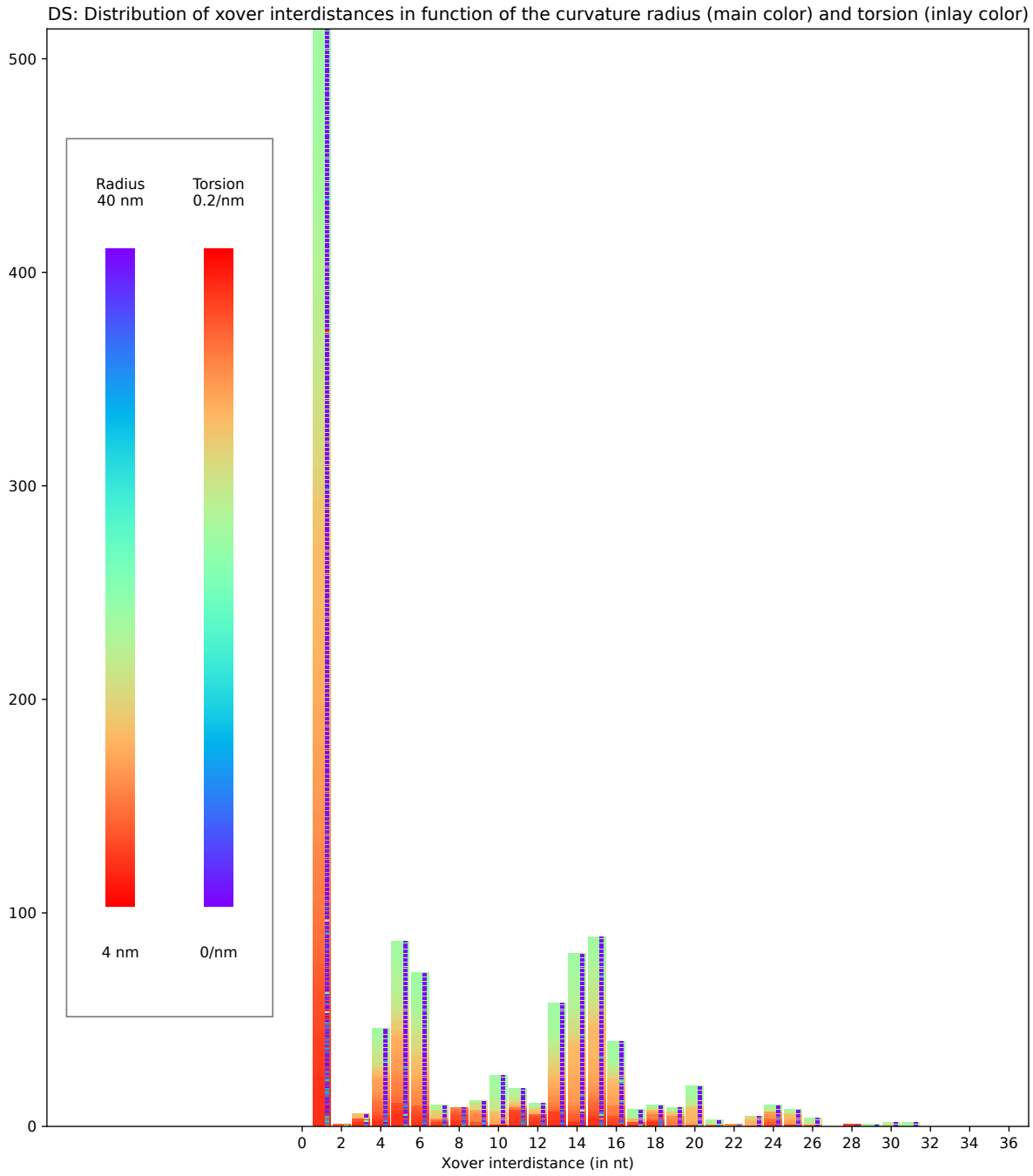


Figure S120: Distribution of staple strand crossover interdistances correlated (in colors) with local curvature radius and torsion in the DS-origami.

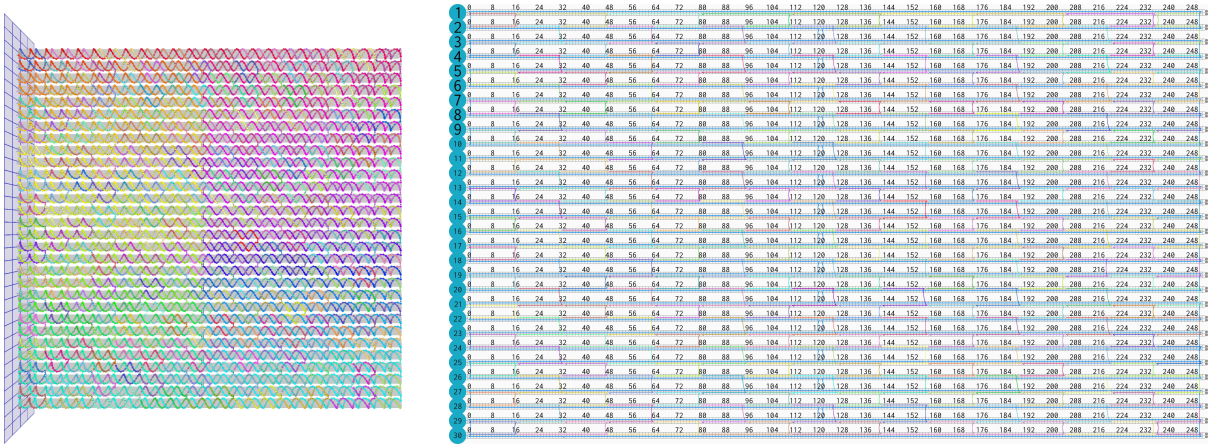

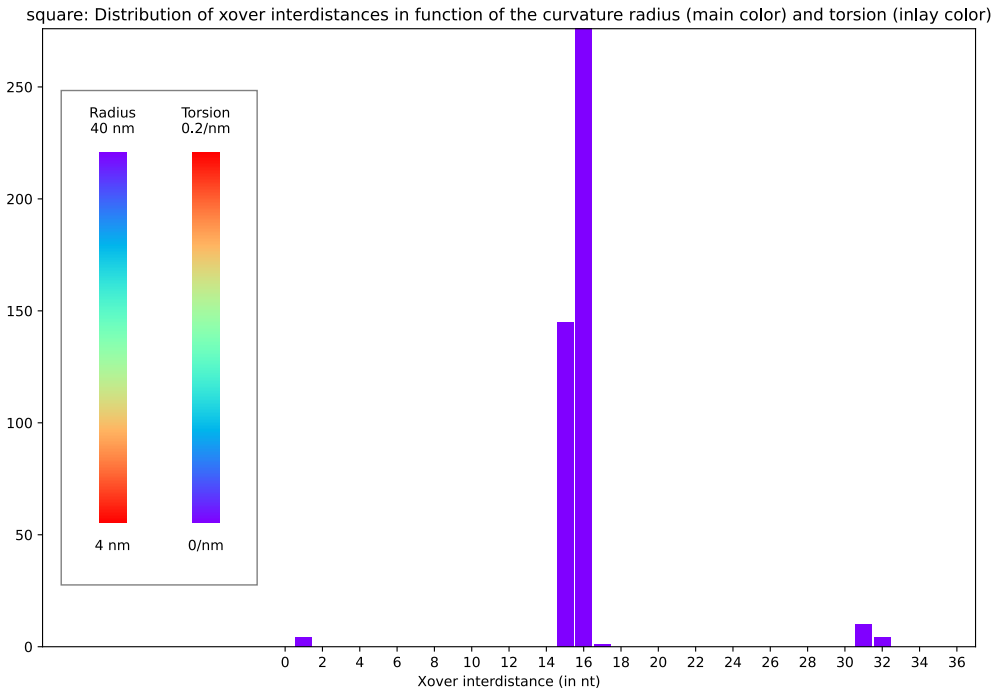


Figure S121: Distribution of staple strand crossover interdistances correlated (in colors) with local curvature radius and torsion in a classic 30-helix square origami (7560-nt scaffold), corresponding to the design shown above.